EXPERIMENTAL INVESTIGATION OF CONSTANT VOLUME SULFUR DUST EXPLOSIONS

BY

JOSEPH KALMAN

DISSERTATION

Submitted in partial fulfillment of the requirements
for the degree of Doctor of Philosophy in Mechanical Engineering
in the Graduate College of the
University of Illinois at Urbana-Champaign, 2014

Urbana, Illinois

Doctoral Committee:

Professor Nick Glumac, Chair
Professor Emeritus Herman Krier
Professor M. Quinn Brewster
Professor Dana Dlott

ABSTRACT

Dust flames have been studied for decades because of their importance in industrial safety and accident prevention. Recently, dust flames have become a promising candidate to counter biological warfare. Sulfur in particular is one of the elements that is of interest, but sulfur dust flames are not well understood. This research investigates the physical and chemical mechanisms involved in sulfur dust combustion. A 31 L constant volume dust cloud combustion facility was designed and built to develop a methodology to determine both the effectiveness of powder dispersion, and also the validity of using pressure-time data to measure flame speed in dust explosions. These results were applied to measurements of the fundamental combustion quantities, such as flame temperature and speed, to ascertain the burning regime of sulfur dust flames.

A two-dimensional laser extinction technique was used to characterize the powder dispersion and uniformity by measuring the particle concentration with spatial and temporal resolution. The two-dimensional measurement provided a methodology to increase the number of line-of-sight measurements (i.e. number of samples) such that the mean concentration was statistically significant. This approach was used to determine the time at which the mean particle concentration approached the expected value. It was observed that at that time, the cloud was most uniform, as indicated by a decrease in the standard deviation of particle concentration. The measurement was then used to determine the effectiveness of anti-caking agents to assist with the dispersion of sulfur. The addition of 1% by mass of submicron fumed silica particles was more effective then the addition of calcium stearate and magneisum stearate even at greater concentrations.

The validity of using pressure-time data within a constant volume dust explosion to measure laminar flame speed was examined by using ionization probes simultaneously. The flame speeds measured by the ionization probes

indicated that the significant amount of turbulence within the system makes it inappropriate to call the calculated flame speeds laminar. Nevertheless, limited agreement was observed between the two measurement techniques. It was concluded that pressure-time data can be used to estimate the flame speed of constant volume dust explosions.

Sulfur dust (-325 mesh) flames were investigated in conjunction with the above results. Spectroscopic measurements indicated the presence of S_2 in the gas-phase, suggesting that sulfur burns at least partially in the gas-phase. Flame temperature and flame speed were measured for sulfur flames with particle concentrations of 280 and 560 g/m^3. The oxygen concentration varied between 10% and 42% by volume. The flame temperature increased with oxygen concentration from approximately 900 K for the 10% oxygen cases to temperatures exceeding 2000 K under oxygen enriched conditions. The temperature was also observed to increase slightly with particle concentration. The reduced temperatures (compared to the adiabatic flame temperature) might be due to incomplete combustion. The unburnt sulfur particles are believed to act as heat sinks, thus decreasing the temperature within the chamber. The flame speed was observed to increase from approximately 10 cm/s with 10% oxygen to 57 and 81 cm/s with 42% oxygen for the 280 and 560 g/m^3 cases, respectively. Flame speeds measured for the 280 g/m^3 powder loading in 21% oxygen were greater than the values reported in the literature, which is likely due to a combination of increased turbulence and smaller heat losses in the experimental setup used here. A scaling analysis determined that flames burning in 21% and 42% oxygen are diffusion limited.

This thesis is dedicated to the memory of the man who first introduced the thought that I could earn a Ph.D., my grandfather, Sidney B. Kalman.

ACKNOWLEDGMENTS

This research could not have been possible, if not for the guidance and support of many individuals. First and foremost, I would like thank my advisor, Professor Nick Glumac, for providing me the education and the means and support to reach this point in my career. I most sincerely appreciate the opportunities he provided me, including mentoring undergraduates, giving guest lectures, attending scientific conferences and of course allowing the freedom to do research in his laboratories.

I would also like to thank Professor Emeritus Herman Krier not only for his advice academically and professionally, but also for sharing his life experiences and all of his humourous stories. I recognize both Professors Glumac and Krier for educating me on the intricacies of technical writing and conducting world class research.

I thank Professors M. Quinn Brewster and Dana Dlott for serving on my Ph.D. committee. I appreciate Prof. Brewster's insight and advice regarding my work on the emissive properties of metal oxide particles. Prof. Dlott's suggestions on the analysis of the combustion mechanism in this work were crucial in making this study complete. The experience and knowledge of all the committee members have helped me to grow and develop as a researcher. Finally, this work would not have been possible if not for the funding from the Defense Threat Reduction Agency (DTRA) with Project Manager Dr. Suhithi Peiris, under grant HDTRA1-11-1-0014.

A benefit of attending an institution such as the University of Illinois is the interaction with many outstanding faculty and graduate students. In addition to the committee members, I would like to thank Prof. Dimitri Kyritsis for sharing his knowledge on combustion as well as providing advise and encouragement. I am also indebted to my friends, and fellow graduate students (past and present) with whom I've worked with over my graduate career: David Allen, Michael Clemenson, Dr. Lance Kingston, Prof. Patrick Lynch,

Dino Mitsingas, Chris Murzyn, Michael Pennisi, Dr. John Rudolphi, Brad Sanders, and Mike Soo. I would also like to acknowledge Joe Vanderveer and Bill Doig with whom I worked with and learned from during my tenure at Rutgers University. I appreciate all that they have done for me in the laboratory and outside of our studies. I thank undergraduate assistants Tommy Pilewicz, David Sung, Phil Rzdanek, and Stefan Dao for their hardwork. I am especially grateful for the assistance and friendship of Sasank Vemulapati who would brave the smell of sulfur, day in and day out. A special thank you goes out to the members of The Band who provided the music I listened to while I wrote much of this thesis.

I would not have gotten my start as an engineer and researcher if not for Mr. Jim Kennedy of Pascack Valley High School. I thank Mr. Kennedy for letting me into the shop 7 am every morning and signing (who knows how many) hall passes after I would continue tinkering in the shop even though my next class had begun.

Last and certainty not least, I thank my family. My grandparents, Sheila Cherry, Gladys Kalman and my late grandfather Sidney Kalman, have been the most loving and generous people I will ever know. My parents Francine and Jeffrey have provided so much that it is impossible to adequately state this in a sentence or two. Their love, support, and dedication to me and my siblings are the reasons I have been able to accomplish as much as I have. My brother Steven and sister Diane have always been there for me and I am so lucky to have them in my life. I also thank my sister-in-law Caitlin for her help proofreading cover letters and other documents. Finally, acknowledging my family would not be complete without mentioning Val, Tina, and Elmo the dog for their love and sometimes providing entertainment.

TABLE OF CONTENTS

LIST OF TABLES ix

LIST OF FIGURES x

CHAPTER 1 INTRODUCTION AND BACKGROUND 1
1.1 Motivation 1
1.2 Gas Flames 2
1.3 Multiphase combustion 4
1.4 Dust Cloud Combustion 8
1.5 Measurements Techniques 13
1.6 Current Work 18

CHAPTER 2 EXPERIMENTAL METHODS 20
2.1 Setup Overview 20
2.2 Dust Cloud Combustion Chamber 21
2.3 Powders Studied 28
2.4 Ignition Source 30
2.5 Diagnostics 36
2.6 Experimental Test Conditions 49

CHAPTER 3 RESULTS AND DISCUSSION 51
3.1 Powder Dispersal 51
3.2 Pressure-Time Validity 61
3.3 Sulfur Dust Combustion 70
3.4 Combustion Mechanism Discussion 90
3.5 Closing Remarks 96

CHAPTER 4 CONCLUSIONS AND RECOMMENDATIONS 99
4.1 Powder Dispersion 99
4.2 Pressure-Time Validity 100
4.3 Sulfur Dust Combustion 101

APPENDIX A STANDARD OPERATING PROCEDURE 103

APPENDIX B CHAMBER DRAWINGS 106

APPENDIX C FRANCK-CONDON FACTOR CALCULATION . . . 122

REFERENCES 125

LIST OF TABLES

3.1 **Spectroscopic Constants for the SO b-X model.** 79
3.2 **Summary of the Chemical Time Scales.** 91
3.3 **Summary of the Diffusion Time Scales.** 92
3.4 **Summary of the Damköhler Numbers.** 92
3.5 **Flame Speed Scaling in the Diffusion Limit.** 94
3.6 **Flame Speed Scaling in the Kinetic Limit.** 95
3.7 **Measured Flame Speed Ratios** 95
3.8 **Low Pressure Test Flame Speed Ratios Relative to 21% Oxygen at 1 bar** 96

LIST OF FIGURES

1.1 Diagram of the structure of a premixed flame front. The width of the reaction zone is greatly exagerrated. 3
1.2 Rendering of a droplet burning under different combustion regimes. 5
1.3 Calculated mole fractions of the important species in sulfur-air combustion. 11
1.4 Calculated adiabatic flame temperature of sulfur-air flames. . . 13

2.1 Schematic of the whole experimental setup. Blue lines-Gas flow tube, Orange Link-Delay Channel 1, Red Line-Delay Channel 2, Black Line-Data 21
2.2 Computer rendering of the dust explosion chamber built. . . . 23
2.3 Photograph of the experimental facility fully equipped. 24
2.4 Schematic of the powder injection process. The assembly sits underneath the chamber. 26
2.5 Picture of the injection nozzle. 27
2.6 Micrograph of the sulfur powder 28
2.7 Measured size distribution of sulfur powder. 29
2.8 Comparison of sulfur powder with (left) and without (right) Aerosil 200. 29
2.9 Micrograph of magnesium stearate powder 30
2.10 Particle size distribution of calcium stearate powder. 31
2.11 Picture of the fireset used to ignite the explosions. 33
2.12 Remnants of the spherical casing igniter. Note the large amount of unburnt powder. 34
2.13 Photograph of the 40 J (3 mm diameter) cylindrical igniter being assembled. 34
2.14 The assembly of the 6 mm diameter cylindrical igniter casing. 35
2.15 Photgraph of the Endevco signal conditioner used for the pressure transducers. 37
2.16 Sample of pressure transducer calibration. 37
2.17 Schematic of the laser extinction and laser shadowgraph experimental setups. 38
2.18 Image of an ionization probe. 39

2.19 Schematic of the flame speed experimental setup. 40
2.20 Photograph of inside the chamber following an experiment. . . 40
2.21 Representative signals from a pair of ionization probes. 41
2.22 Micrograph of a R-type thermocouple coated in alumina paint 42
2.23 Micrograph of a bare R-type thermocouple. 43
2.24 Schematic of the emission spectroscopy setup. 45
2.25 Schematic of the absorption spectroscopy setup. 46
2.26 Sample spectral calibration from the neon lamp. 47
2.27 Sample spectral calibration pixel-to-wavelength mapping from the neon lamp. 48
2.28 Spectral response of the detector determined from the tungsten lamp. 49

3.1 Raw image taken from sulfur powder injection. Note the large clumps that have formed. 52
3.2 Images and optical depth contours taken from dispersal of titanium powder (406 g/m^3). 53
3.3 Mean concentrations of titanium as a function of time for a range of powder loadings. 54
3.4 Standard deviation of titanium powder concentration. 55
3.5 Mean concentrations of titanium at 400ms after injection has ended. 55
3.6 Single line-of-sight measurements for titanium dispersal. . . . 56
3.7 Measured particle concentrations with the addition of varying amounts of calcium stearate. 58
3.8 Measurements of the particle concentration with the addition of magnesium stearate. 59
3.9 Measured particle concentration with small amounts of Aerosil 200 added to the sulfur powder. 60
3.10 Radius of a stoichiometric methane-air flame as a function of time. The flame speed is taken from the slope (mm/ms). . . 63
3.11 Representative voltage traces from the ionization probes from a sulfur flame. 64
3.12 Shadowgraph image taken from a sulfur explosion. The particle concentration was approximately $280 g/m^3$. 64
3.13 Measured flame speed with pressure and ionization probes for different ignition energies. 65
3.14 Sample pressure-time data from a sulfur explosion. 66
3.15 Calculate flame speed from pressure-time data. 67
3.16 Calculated (first order approximation) ratio of the conductive and radiative heat losses at multiple positions and flame temperatures. 68
3.17 Comparison of the flame speed determined by the ionization probes and pressure-time data. 69

3.18 Maximum pressure rise (absolute pressure) for sulfur explosions within a 31 L chamber. 71
3.19 Maximum rate of pressure rise (absolute pressure) within the 31 L chamber from sulfur explosions. 72
3.20 Emission spectrum taken with the Jaz spectrometer over the UV-Visible-IR region from a 21% oxygen, fuel-rich sulfur explosion. 73
3.21 Moderate resolution (0.5 nm) emission spectrum of the UV features from a sulfur explosion. Spectrum was taken with the 444 mm focal length spectrometer and a 300 gr/mm grating. 74
3.22 Emission features of the sulfur dimer in the blue part of the spectrum. Spectrum was taken with the 444 mm focal length spectrometer and a 300 gr/mm grating. 75
3.23 Emission spectrum in the near infrared. Spectrum was taken with the 444 mm focal length spectrometer and a 300 gr/mm grating. 76
3.24 High resolution (0.15 nm) of the SO b-X transition. Spectrum was taken with the 444 mm focal length spectrometer and a 1200 gr/mm grating. 76
3.25 Simulated spectrum at 1000 K and 4500 K as produced from PGOPHER. 80
3.26 Representative filtered signals for the PMT pyrometer. Only the 825 nm and 905 nm signal are shown. 83
3.27 Calculated temperature profile from the data in Figure 3.26. The initial peak is from the igniter. 83
3.28 Fits of the thermal background from the Jaz spectrometer to determine temperature. 85
3.29 Temperature measurements of sulfur dust explosions. 86
3.30 Emission spectrum showing the possible molecular interference near 900 nm for experiments with 42% oxygen. 86
3.31 Measured peak temperatures adjusted for isentropic compression. 88
3.32 Flame speed measurements by analysis of pressure-time data for sulfur dust explosions. 89

C.1 Illustration of the energy diagram for an electronic transition of a molecule. The orange curves indicate the vibration wavefunctions. Energy levels are not drawn to scale. . . . 123

CHAPTER 1

INTRODUCTION AND BACKGROUND

1.1 Motivation

Combatting the release of harmful biological aerosols from an attack efficiently and swiftly is crucial should the situation arise. Furthermore, any bio-defeat technology should be both simple and effective. A reacting dust cloud of energetic material is one method that is receiving attention [1]. Powders, typically metals, are dispersed and ignited. The burning particle cloud has several aspects that contribute to defeat the bio-aerosol. The energy released from the burning powders creates a high temperature environment that can be lethal for biological spores. Furthermore, the flame speed of the dust flame is on the order of 10s of centimeters per second. This slow (relative to detonations) deflagration will help sustain the high temperature environment for extended periods of time with potentially a large amount of thermal radiation adding to the effectiveness. Finally, powders may be mixed or mechanically alloyed with materials that are used specifically to destroy biological samples (e.g. iodine).

The inclusion of iodine in energetic materials has been studied within the energetics community. Approaches involving aluminum-iodine pentoxide thermites [2] as well as aluminum iodine alloys [1] have shown to be effective in killing biological spores due to the release of iodine . Alumimum-iodine mechanically alloyed powders have also shown the ability to produce temperatures exceeding 3000 K [3, 4].

Other energetic materials, such as titanium-boron alloys, have been tested as well for this application [1, 4, 5]. This alloy contains the high energy density of boron and the more easily ignited titanium. The long burn time of the composite is beneficial for creating a high temperature environment for longer periods of time. In addition, titanium dioxide, a product of tita-

nium combustion, may be useful in defeating biological aerosols due to its photocatalytic properties [6].

Sulfur dust is another potential candidate and is just starting to receive some attention for bio-defeat applications. Sulfur dust has been used as a pesticide [7]. However, the more intriguing aspect of sulfur dust clouds is that they produce sulfur oxides which are chemical precursors to sulfuric acid [7]. It is well-known that sulfuric acid is extremely corrosive and dangerous to living organisms (humans included). The concept is that burning sulfur clouds will produce sulfur dioxide and sulfur trioxide. In the presence of water, sulfuric acid is formed. It is thought that sulfuric acid created will kill the spores. Other strong acids have been shown to be effective sporicides [8].

To date, very few studies have investigated sulfur dust clouds. The primary goal for the current work is to measure fundamental aspects of sulfur dust cloud combustion in terms of fundamental quantities (e.g. flame speed) and to gain insight into the physical and chemical mechanisms involved. Secondary objectives include developing required diagnostics to better understand constant volume dust explosions.

1.2 Gas Flames

Prior to discussing the mechanisms involved in multiphase combustion, it is useful to review the physics involved in gaseous flames. Flames may be considered waves whose propagation is self-sustained due to the energy release by converting reactants to products. Two types of gaseous flames exist: premixed and diffusion flames. Both types will briefly be reviewed. From a macroscopic view, dust flames are viewed as premixed flames since the fuel (i.e. particles) and oxidizer are mixed. However, individual particle flames are considered diffusion flames. This point will be further explained below.

Premixed flames start as homogenous mixtures of the fuel, oxidizer, and possibly an inert diluent. The flame can be broken into several zones as illustrated by Figure 1.1. Downstream of the flame front is the preheat zone. Conduction and convection transport energy from the flame to the cold reactant mixture gas thereby raising its temperature. Flame propagation is also assisted by the diffusion of reactive radicals and other species. Ignition occurs due to a combination of mass and heat transport that initiate chain

propagating and branching reactions. The reactants are converted to products via multiple (and often many) intermediate reactions. An activation energy (which is sometimes expressed as an ignition temperature) refers to a very simplified condition that describes the onset of combustion, if the multiple reactions are modeled as a single, global reaction. The portion of the flame where this process occurs is the reaction zone and is typically much thinner than the preheat zone and is greatly exagerrated in Figure 1.1. The maximum temperature that can be reached from the energy release in this reaction zone, *assuming equilibrium conditions*, is called the adiabatic flame temperature. Far upstream the hot product gases, (barring any heat losses) along with the inert diluent, and excess reactants, approach thermal equilibrium composition.

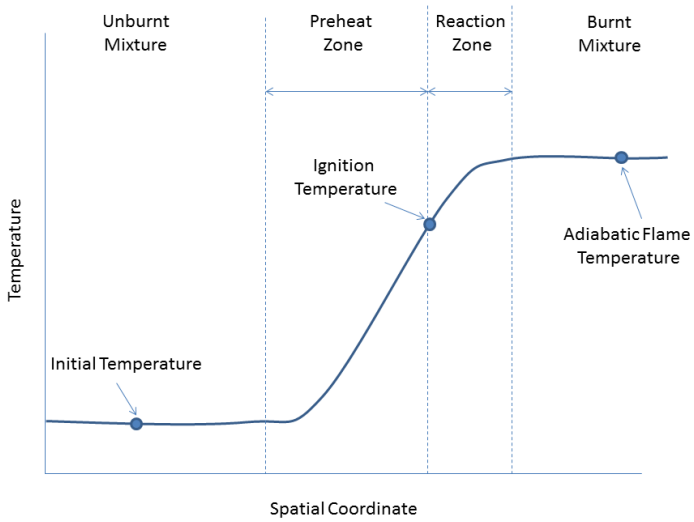

Figure 1.1: Diagram of the structure of a premixed flame front. The width of the reaction zone is greatly exagerrated.

Stoichiometric mixtures are those that contain the same ratio of fuel to oxidizer molecules in the reactants as is necessary to form the standard combustion products (i.e. all of the oxidizer and fuel can be consumed). Mixtures that contain excess fuel are called fuel-rich while those that contain additional oxidizer are referred to as fuel-lean. The fuel to oxidizer ratio compares the mass (or moles) of fuel to the mass (or moles) of oxidizer. The equivalence ratio, Equation 1.1, describes how fuel-rich or lean a mixture is by dividing the actual fuel to oxidizer ratio by the stoichiometric one.

$$\phi = \frac{(m_{fuel}/m_{Ox})_{actual}}{(m_{fuel}/m_{Ox})_{stoich}} \tag{1.1}$$

Not all mixtures are able to sustain a flame. Experimental work for almost all gaseous fuels have determined flammability limits. The lean limit is the lowest equivalence ratio able to support a flame. Similarly, a rich limit typically exists as well (with acetylene and other monopropellants being the exception [9]). The presence of too much diluent or other molecules may also prevent ignition.

Although there are several important parameters describing flame dynamics, flame speed is one of the most fundamental quantities and is useful for characterizing dust flames. Flame speed is a measure of how quickly the flame front propagates. Two regimes further categorize the flame: deflagration and detonation. Deflagration is the name given to flames that travel at rates below the local speed of sound. Across these waves the pressure is approximately constant as described by the Rankine-Hugoniot relations. On the other hand, detonations travel faster than the local speed of sound. A shock wave is supported by the heat release in the flame front in detonations. The so-called upper Chapman-Jouguet point from the Rankine-Hugoniot relations is the only stable detonation [10].

Unlike premixed flames, diffusion flames have separate streams for both the fuel and oxidizer. Each stream may also contain diluent. The fuel molecules diffuse into the oxidizer stream and vice versa. The reaction zone is located at the position where a stoichiometric mixture exists. Combustion products and heat release from the reaction diffuse outwards. As mentioned above, a flame from an individual particle is an example of a diffusion flame. As such, the concept of the diffusion flame for a system with only gaseous components (e.g. Burke-Schumann flame) is introduced to bridge the gap between gaseous and multiphase combustion [10, 11].

1.3 Multiphase combustion

The classic starting point for multiphase combustion is the droplet vaporization problem. By considering a spherically symmetric liquid droplet that is heated in a quiescent gaseous environment, it can be shown that the time

required to vaporize the droplet completely is proportional to the square of the initial droplet diameter. The partial pressure of the vaporized fuel is equal to the vapor pressure of the liquid at the liquid-gas interface. Once in the vapor phase, the fuel molecules diffuse outward [11].

In droplet combustion, a similar scenario exists where the flame provides the heat to vaporize the droplet. Figure 1.2 shows the structure of an individual droplet under combustion. The inward moving oxidizer meets the outward diffusing fuel at the flame front in the same manner as described in the previous section. This process is called diffusion limited since the controlling factor is the diffusion of the reactants to the flame front. The time to completely burn the fuel droplet is still proportional to the square of the diameter because diffusion is the limiting process. This result is shown in Equation 1.2 where ρ_s is the density of the particle, d is the initial particle diameter, ρ is the density of the gas, D is the diffusion coefficient of the gas, i is the mass stoichiometry ratio, and $m_{0\infty}$ is the concentration of oxygen far away from the particle. The flame temperature in the diffusion limit typically exceeds that of the ambient [9].

$$t_{b,diff} = \frac{\rho_s d_0^2}{8\rho D ln(1 + i m_{0\infty})} \tag{1.2}$$

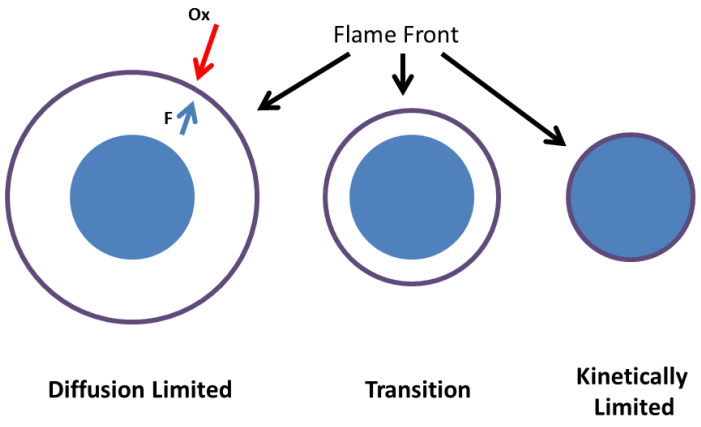

Figure 1.2: Rendering of a droplet burning under different combustion regimes.

$$t_{b,kin} = \frac{\rho_s d_0}{2i\rho m_{0\infty} k_s} \tag{1.3}$$

The burn time in the other limiting case is determined by the reaction kinetics. In this situation the reactants are able to diffuse to the flame front quick enough but the rate at which they are consumed limits the process. The time to burn a particle in the kinetic limit, Equation 1.3, scales directly with the initial diameter (i.e. d^1) as opposed to the d^2 law for the diffusion limit. The variable k_s is a reaction rate coefficient with units of length per time. In addition, the temperature of the flame is very close to ambient. A particle burning in the kinetic limit is usually dominated by reactions at or near the surface of the particle [9].

Turns [11] used a resistance analysis, anologous to electrical resistance, to determine in which regime a particle burns. A similar approach looking at the ratio of the kinetic and diffusion time scales can provide the same insight. The ratio of these time scales is called the Damköhler (Da) number. The ratio of the kinetic and diffusion limited burn times is shown in Equation 1.4 which is of the form of a Damköhler number. The particle will burn in the kinetic limit if Da is much smaller than unity and in the diffusion limit if Da is much greater than unity. When this time scale ratio is on the order of unity, then one can define a transition regime where both the kinetics and diffusion are equally important to the process.

$$Da = \frac{t_{b,diff}}{t_{b,kin}} = \frac{d_0 i \rho_s k_s}{4D ln(1 + i m_{0\infty})} \tag{1.4}$$

This analysis typically indicates that small particles tend to burn in the kinetic limit while large particles favor a diffusion controlled process. By considering scaling dependences of the diffusion coefficient (as calculated from kinetic theory), scaling dependences on temperature, T, pressure, P, and molecular weight (MW) can be determined. The diffusion coefficient is shown in Equation 1.5 where temperature is in Kelvin, pressure is in atmospheres, and molecular weight is in atomic mass units, and σ is the gas particle radius in Angstroms [12]. Particles in high pressure environments and ambient gases of higher molecular weight tend to burn in a diffusion limited manner [11, 9]. The temperature scaling is not as straight forward since the reaction rate coefficient is also typically temperature dependent.

The kinetics are related to temperature exponentially.

$$D = 2.6295(10^{-7})\frac{T^{1.5}}{MW^{0.5}P\sigma^2} \tag{1.5}$$

The Glassman criterion [9] is typically used to determine whether a particle burns in the vapor phase or a condensed phase. Metals whose boiling point is lower than their metal oxide are said to burn in the vapor phase or homogeneously. The reverse holds for materials burning in a condensed phase or heterogeneously. This criterion is a rule of thumb, since it is not true in all cases [9]. Often (but not always) particles that burn in the kinetically limited regime are dominated by heterogeneous reactions and diffusion limited particle combustion consists of a strong gas-phase (i.e. homogeneous) component. Particles burning in the transition regime are believed to have a flame front that is nearer to the particle surface than in the diffusion limited case, but not as close (or on the surface) as kinetically limited particle combustion. This point is illustrated in Figure 1.2 [13, 14] .

Combustion of individual particles and dust flames in all three of these regimes have been observed experimentally. For example, the burn time data for aluminum combustion compiled by Beckstead [15] has shown that aluminum particles burn in the diffusion limit based upon the d^2 dependence. This correlation is valid for particles with diameters from 10s of microns and larger. Shock tube work of individual aluminum particles on the order one micron demonstrated the transition away from the diffusion limited regime towards the kinetically limited regime [13, 14].

Previous work with dust flames has shown how this analysis can be extended to flames where multiple particles are burning as opposed to an individual particle. Goroshin and co-workers have analyzed both aluminum and iron flames in this manner [16, 17]. They also observed that changing the diluent gas in a flame can affect the burning regime by altering the gas diffusivity. Aluminum flames were seen to transition away from the diffusion limited regime when the diluent was changed from argon to helium [17].

Analysis by Goroshin et al. [16] used the flame speed scaling analysis from Landau and Lifshitz [18] in the diffusion limit of $\sqrt{\alpha D}$. Goroshin et al. [16] argued that flame speed should scale as $\sqrt{\alpha}$ for kinetically limited flames, where α is the thermal diffusivity. The ratio of the experimentally measured iron flame speeds with helium compared to those with argon as the diluent

was significantly larger than what woud be expected of a flame in either limiting regime. The authors concluded that the strong deviation from the theoretical scaling was due to the flame burning in the transition regime [16]. An appropriate scaling is not known for flame speed in the transition regime.

1.4 Dust Cloud Combustion

Dust cloud combustion and explosions are analogous to gaseous flames with the exception being the fuel is introduced in the solid state and consists of discrete particles. They do, however, contain aspects of both particle combustion and gaseous flames. The concept was introduced in the last section but it is worth describing dust flames in more detail. Specifically, an introduction to sulfur dust explosions and the complexities that surround dust flames in general will be given.

Dust cloud explosions have been studied for nearly a century. This field started so that researchers could better understand how to prevent accidental explosions in industrial settings such as coal mines, silos, and factories [19]. Quantities like minimum ignition energy and minimum explosive concentration were of particular interest to prevent explosions. Other parameters such as pressure rise (maximum and rate of pressure rise) within constant volume chambers were measured to enable engineers to properly design vessels that can withstand the load created by a dust explosion. Temperature and flame speed measurements provided additional insight into the combustion phenomena.

Different types of experimental facilities were developed to measure these quantities. The Hartmann apparatus is a small (1.2 L) tube that is used to determine minimum flammability limits [20]. Constant volume explosion chambers are used to measure a variety of quantities. Standards for a 20 L spherical and 1 m^3 chambers have been established although other sizes and geometries have been used in the literature [21]. Constant volume explosion vessels are used to obtain pressure measurements which indicate the severity of the explosion. Others have used long (with respect to the diameter) tubes for fundamental work on flame speed and quenching distance [22, 23].

No matter the experimental approached used or the specific dust/fuel, all dust explosion research requires the dispersal of the powder prior to ignition.

The particle injection into the chamber and subsequent dispersal is one aspect of this work that remains challenging.

1.4.1 Powder Injection

Commonly used constant volume experiments have the ability to provide an environment where gaseous composition and global particle concentration can be controlled and the pressure-time data can provide critical information on the reactivity of the powder. Despite the benefits that this experimental setup provides, it involves several processes that each introduce additional complexity. Powder dispersal is one of these processes.

The dust suspension is created by powder being injected via a burst of pressurized gas (usually air). Experiments conducted within most chambers typically use standards for the injection process (i.e. line pressure, temporal length) [19]. This injection process produces an unsteady, turbulent environment, where the particle concentration varies spatially and temporally. Laser extinction probes have been used to measure local particle concentrations. Cashdollar and coworkers [24, 25] used laser extinction probes placed inside their dust explosion facility to measure particle concentration. Kalejaiye et al. [26] used multiple discrete probes within the chamber to determine the effectiveness of particle dispersal and dust uniformity. They used statistical data to determine uniformity and the ratio of Sauter mean diameter from the experiments and particle size analysis to find the extent of particle agglomeration/break up [26]. The placement of the probes within the chamber makes the measurements intrusive and may affect the measurements.

Research has been conducted in order to understand how this turbulence affects explosiveness parameters like pressure rise. Kauffman et al. [27] used hot wire anemometry to quantitative measure pre-ignition turbulence and found that both the maximum pressure and pressure rise rate increase with the amount of turbulence. Zhen et al. [28] corroborated this influence by varying the ignition delay before ignition. They also studied the influence of post-ignition turbulence and concluded that the turbulence produced by strong igniters may influence quantities such as particle concentration and flame propagation [28].

1.4.2 Cloud Ignition

Various ignition sources relevant to these industrial settings are typically used. Electrostatic discharges and hot surfaces or gases (i.e. from an open flame) were common sources of the accidental explosions. Researchers used sparks, hot wires, and pyrotechnic igniters to initiate experiments [19]. Sparks and pyrotechnic igniters are popular ignition sources because the energy release may be easily controlled. The disadvantage to these ignition sources is that they are typically accompanied by a blast wave, albeit weak, that can potentially affect the local particle concentration.

The work by Di Benedetto et al. [29] studied the effect of ignition energy on turbulence level and deflagration parameter. They found the deflagration parameter (i.e. rate of maximum pressure rise normalized with the size of the chamber) was independent of ignition energy, but were unable to make any conclusions on the effect of turbulence. Kuai et al. [30] were able to show that there is a critical ignition energy for organic dusts for which the cloud is most explosive but they reported that no such energy was seen for metallic powders.

Although previous research has provided insight into the dispersion and ignition processes, there has been minimal experimental work investigating how the spatial distribution of particle concentration is affected by these processes. To our knowledge, only the computational investigation by Cloney and coworkers has studied this aspect. Their work was simplified by using a one-dimensional computational model which inherently removed any turbulence-induced swirling/rotational motion [31].

1.4.3 Sulfur Dust Combustion

Sulfur is one dust fuel that has not been studied extensively. Burning sulfur produces a combination of sulfur monoxide, sulfur dioxide and sulfur trioxide. The primary combustion product is sulfur dioxide because it is favored thermodynamically. The equilibrium composition, calculated from the NASA CEA program [32], of the major and several minor species in an atmospheric stoichiometric flame is plotted in Figure 1.3. The global reaction, Equation 1.6, is exothermic. The melting and boiling point of sulfur under atmospheric pressure are about 392 K and 718 K, respectively. Sulfur dioxide's

boiling point is lower at 263 K [33]. Glassman's criterion would suggest that sulfur burns in a condensed phase. Proust [34] showed experimentally that sulfur dust boiled prior to the flame front arrival, meaning that the vapor phase reactions dominate the event. Glassman's criterion may not be relevant because the properties of sulfur are much different than carbonaceous and metal fuels. The adiabatic flame temperature (discussed below) is much greater than the boiling temperatures of the fuel and oxide.

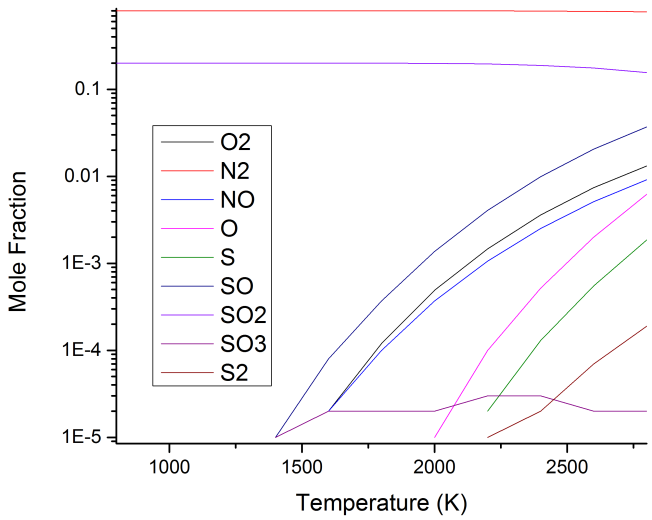

Figure 1.3: Calculated mole fractions of the important species in sulfur-air combustion.

Reaction kinetics of sulfur oxidation have been studied because of the importance of the sulfur oxides as a pollutant [11]. The University of Leeds created a reaction mechanism for sulfur oxides [35]. Because this mechanism was produced with an application towards minimizing pollutant formation, it does not include any condensed phase kinetic data which would be necessary for sulfur dust flames. Atomic and dimer sulfur are the only allotropes of sulfur that it includes. The dimer is the primary gas phase component for sulfur vapor [33] which is why Equation 1.6 is not shown in terms of atomic sulfur. Of course, other thermodynamic conditions will give rise to larger allotropes in significant quantities [33].

$$S_2 + 2O_2 \rightarrow 2SO_2 + 464.2\frac{kJ}{moleS_2}$$

(1.6)

Early work suggests that the ignition temperature of sulfur is near 530 K [33]. Minimum ignition energies (by spark) have been measured to be 0.01 mJ for very fine (on the order of one micron in diameter) sulfur powder which is among the lowest for dusts [36]. The minimum ignition energies are dependent on the type of igniter including whether the spark was from a capacitive, inductive, or resistive load [19]. The lower flammability limit (i.e. minimum explosive concentrations) has been reported as 30 g/m^3 for particles with an average diameter of 20 μm [36].

Even though the oxidation of sulfur is exothermic, it releases less energy than other energetic materials such as aluminum. The total heat release produced a pressure rise ratio of 6.8 for fuel-rich suspensions in air [19]. The adiabatic flame temperature for a stoichiometric sulfur-air flame at 1 atmosphere can approach 2000 K. The adiabatic flame temperature calculated from using the CEA program [32] is shown as a function of equivalence ratio in Figure 1.4. The stoichiometric concentration of sulfur (burning in air) is 280 g/m^3. The flame temperature has been measured to be below 1500 K for stoichiometric flames [34]. The temperature is much lower than the adiabatic flame temperature, as shown in Figure 1.4. Proust [34] conducted the experiments in a tube where heat losses (and thus no longer adiabatic) to the wall may be significant.

Nagy and Verakis reported a flame speed of 75 cm/s for a dust concentration of 500 g/m^3 for 44 μm diameter particles in air[37]. Later, Proust [34, 38] measured the flame speed of sulfur dust with two different methods over a range of equivalence ratios. Sulfur dust particles with diameters between 25 and 45 microns were suspended in air. The flames were measured to propagate between 15 cm/s for fuel-lean (50 g/m^3) and 23 cm/s for stoichiometric conditions [34].

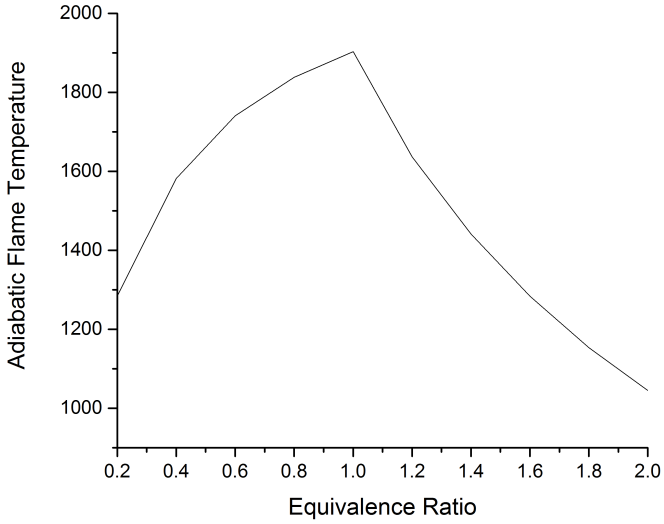

Figure 1.4: Calculated adiabatic flame temperature of sulfur-air flames.

1.5 Measurements Techniques

Conducting measurements in these potentially hostile environments can introduce other difficulties. Although devices such as thermocouples can record accurate temperature and be straightforward to use, they have a disadvantage of being intrusive. Inserting such a device may alter a flow and affect the chemistry locally [39]. Because of some of downfalls of intrusive measurement probes, it can be advantageous to use optical and spectroscopic diagnostics to probe environments typically seen in reacting dust clouds, explosions, and other reacting media whenever possible.

1.5.1 Temperature

Numerous spectroscopic methods such as emission and absorption spectroscopy [17, 40], or laser techniques like Raman scattering or laser induced fluorescence have the ability to provide gas temperatures [41]. The measured temperature is determined by finding which temperature (with possibly other parameters like pressure and concentration) provides a simulated spectrum that best fits the experimentally measured spectrum.

The basis for spectroscopic temperature measurements comes from the ability of atoms and molecules to rapidly store energy in various modes. En-

ergy can be stored within translational, rotational, vibrational, and electronic modes for molecules with translational and electronic modes being the only option for atoms [12]. Quantum mechanics specifies the discrete energy levels that exist for each of these modes. When the energy level (for any of these modes) changes, a photon is emitted or absorbed. However, only certain transitions are allowed based upon the so-called selection rules for an electric dipole [42]. Other transitions can occur but are less probable and they are due to higher order effects such as magnetic dipoles, electric quadropoles, etc. The wavelength of the photon is dependent on the difference in energy of the two states.

The result is a discrete transition. Due to the very fine spacing of the translational mode, the individual transitions cannot realistically be resolved. However, rotational, vibrational, and electronic transitions can easily be resolved with the appropriate spectrometer or interferometer. The energy involved within the transition increases from translational, rotational, vibrational, to electronic [12]. Transition of different modes (e.g. vibrational and rotational) are often coupled to each other. Higher order effects give rise to rotational distortion (i.e. no longer a rigid rotor) and anharmonic vibrational modes [42].

The energy involved in electronic transition results in the photon having a wavelength within the ultraviolet (UV), visible, or near infrared (nIR). Vibrational and rotational transitions can occur simultaneously with the electronic transition. The Franck-Condon principle states that the electron motion is much faster than the motion of the nuclei (e.g. when vibrating) that the radius of the molecule is essentially constant during the transition [42]. As such, certain vibrational states (in the final electronic state) have a higher probability of occuring. The relative probability is determined by the overlap of the vibrational wavefunctions. The square of the convolution of the final and initial vibration wavefunctions is called a Franck-Condon factor [42].

The energy levels just described are populated with a given distribution at a specified temperature. The Boltzmann distribution is used to determine the population in each level or state. Experimentally, the intensity of light from each transition dictates the relative strength of each transition. As such, comparing the intensity of at least two lines can provide a temperature [12].

Although quantum mechanics provides the individual, discrete wavelengths

for each transition, broadening of the spectral line from a variety of sources is observed. So-called natural broadening occurs due to the uncertainty principle and is the minimum line width physically possible. Other broadening mechanisms (Collisional and Doppler broadening) result from the motion of the molecules in the gas [12, 41]. Finally, the optical equipment used in the collection optics add additional broadening to the measured spectrum which is called instrument broadening.

The simulated spectrum can be calculated using the Boltzmann distribution and the equations for broadening with the spectroscopic constants that descirbe the electronic, vibrational, and rotational motion for the appropriate transition. The overall strength of each transition also needs to be included. The Franck-Condon factor represents the strength of a vibrational transition and Höln-London factors are calculated for the strength of rotational transitions for diatomic molecules.

Software, such as LIFBASE or PGOPHER, is available to complete the simulation of spectra [43]. These programs calculate the populations of each state for a given temperature and transition with the spectroscopic constants. The appropriate broadening mechanisms are included and the convoluted intensity at each discretized wavelength is calculated. A spectrum is the result. In the current work, PGOPHER was used.

Another method for measuring temperature that is particularly important for dust clouds and explosions is pyrometry [44]. Pyrometry compares the irrandiance of at least two narrow spectral bands [45]. Applying Planck's equation for thermal radiation to these measurements, a temperature can be found as shown in Equation 1.7. This measurement provides the temperature of a solid or liquid surface (i.e. condensed phases). Knowledge of the emissivity is necessary to accurately determine the temperature.

$$T = hc\frac{\epsilon_1(\lambda_1, T)}{\epsilon_2(\lambda_2, T)}\frac{I_{meas2}}{I_{meas1}}(\frac{\lambda_2}{\lambda_1})^5 \ln(\frac{1}{\lambda_2} - \frac{1}{\lambda_1}) \tag{1.7}$$

Lynch et al. [46] demonstrated that the wrong assumption in the wavelength dependence of the spectral emissivity may result in an error of as high as 1000 K for burning aluminum particles . Kalman et al. [47] showed experimentally and theoretically that the optical depth of the dust cloud needs to be considered. The apparent spectral dependence was seen to be a function of the optical depth [47]. Work by the same authors presented findings on

how the spectral emissivity is also highly dependent on material and was quantified for several common metal oxide powders [48].

1.5.2 Flame Speed

Flame speed can be calculated by monitoring physical indicators, such as temperature, light emission, flow rate or species as the wave moves through the medium. A large rise in temperature or light emission is indicative of the reaction zone of the flame. Intermediate species (e.g. OH in hydrocarbon flames) that are present in the reaction zone can be measured through techniques like laser-induced fluorenscence to infer the location of the flame front. Another approach is to monitor the flow rate of gases that is necesary to stabilize a steady flame on a burner [10].

Several types of experimental setups can be used to measure flame speed for dust clouds. Cassel [49, 50] was able to create a flat flame burner to measure flame speed. More recently, small scale Bunsen-type burners have been used to measure the propagation velocity of aluminum-oxygen-inert flames [17, 51]. The flames in these burners are curved due to the velocity distribution of the carrier gas. The reported flame speeds were calculated based upon the mass flow rate through the surface area of the flame. Scaling the measured speed with the ratio of the densities for the fresh and burnt gases is required to obtain the laminar flame speed [10]. This relationship is shown in Equation 1.8 where S_L° is the laminar flame speed, S is the measured flame speed, and ρ is the gas density.

$$S_L^o = S\frac{\rho_{burnt}}{\rho_{unburnt}} \tag{1.8}$$

Another common method is to ignite a powder dispersion within a long tube. Researchers have used this approach not only to measure flame speed but the quenching distance, as well [23, 22]. Video of the event is recorded, and the luminosity of the flame front is tracked through a region of the tube. Using this approach, a short distance is typically needed for the flame to fully develop [22]. Since heat is lost to the walls, the flame speed has some dependence on the tube diameter [34].

The final setup is a constant volume chamber. Particles are injected into the chamber, which are ignited near the center of the vessel. Like the tube

method, light from the flame front can be used to track the front, but this approach is not utilized often because of the limited optical access in the spherical chambers often used. Others have used the pressure-time data to measure flame speed. Knapton, Krier, and coworkers [52] developed a model that related the pressure to the instantaneous flame speed which increases with pressure. However, that approach does not provide the same fundamental measurement of the laminar flame speed that the methods described above do.

Dahoe et al. [53] analyzed the following situation by considering a constant volume chamber with well-insulated walls. The chamber was assumed to be filled with reactants that are perfectly mixed and stagnant. They analyzed the result of igniting such a system from the center. If the flame is not wrinkled and buoyancy is neglected, a perfectly spherical, infinitely thin (idealy) flame front would begin to propagate outwards releasing chemical energy into the system as heat. The flame front breaks the chamber into two regions, the burnt and unburnt mixtures. Since the chamber has a fixed volume and heat cannot escape due to the well-insulated walls, the pressure rises from the heat addition. Moreover, the hot combustion products within the spherical flame will expand, thus compressing the unburnt gas isentropically.

They conducted a thermodynamic analysis on the chamber. They arrived at the following equation (Equation 1.9):

$$\frac{dp}{dt} = \frac{3}{R}\left(\frac{dx}{dp}\right)^{-1}\left[1 - \left(\frac{p_i}{p}\right)^{\frac{1}{\gamma}}(1-x)\right]^{2/3}\left(\frac{p}{p_i}\right)^{\frac{1}{\gamma}} S_L \tag{1.9}$$

where,

$$x(p) = \frac{p - p_i}{p_e - p_i} \tag{1.10}$$

and p is the instantaneous pressure, p_i and p_e are the initial and maximum pressures, respectively, R is the spherical equivalent radius, γ is the ratio of the specific heats and assumed to be constant, S_L is the laminar flame speed. The analysis Dahoe el al. [53] conducted on this method included the additional assumption of a linear dependence on pressure for the mass burnt fraction, $x(p)$ (Equation 1.10). The work by Luijten et al. [54] used a multi-zone approach to develop a more rigorous definition for x, although, it is not shown here because of its length.

Nair and Gupta [55] used ionization probes within a constant volume explosion vessel to measure the local flame speed of butane-air mixtures. They applied the theoretical model by Manton et al. [56] to determine the laminar flame speed from the measurements. The expression derived by Manton and coworkers used the same assumptions as Equation 1.10. Santhanam et al. [21] used Equation 1.10 with the assumption of a linear $x(p)$, to measure flame speed from a constant volume aluminum explosion. They reported laminar flame speeds similar to those reported in the literature. Despite these results, it is still not clear whether Equation 1.10 accurately describes the flame propagation within constant volume dust explosions, because this expression has not been validated experimentally.

Also, many of the assumptions made in the analysis to obtain Equation 1.9 may not apply for dust flames. The dust injection process is turbulent which prevents the mixture to be at rest at ignition. Since dust particles are much larger than gaseous fuel molecules, the suspension is not perfectly mixed down to the same length scale as gaseous mixtures. Phase change of the particles increases the complexity. Moreover, it has been observed that the thickness of dust flames is much larger than the narrow front produced by gaseous flames due to the burn time of the individual particles [57].

1.6 Current Work

There are aspects of sulfur dust cloud combustion that still require additional work. The injection process, as described above, is a turbulent event. Some (not many) of the previous literature have addressed some of the problems surrounding the turbulent nature and the particle concentration at discrete locations within a combustion chamber. The first objective is to investigate the spatial uniformity of the powder during injection. The goal is to provide a quantitative approach, but not necessarily a standard, that describes how effectively a powder is dispersed. That information will then be used to find the most appropriate time to ignite the mixture with respect to particle concentration.

The thermodynamic analysis described in the previous section provides an approach to measure flame speed within a constant volume chamber. It has been shown that previous work on gaseous flames demonstrate the validity

of using pressure-time data to deterine flame speed. Here, we experimentally investigate the validity of using the pressure-time data to determine the flame speed of dust flames. The goal is to provide the combustion community the necessary data and analysis to use in order to measure flame speed.

The third and final objective is to better understand sulfur dust combustion. As noted earlier, limited data exists on sulfur dust flames. Only a portion of that work is applicable to dust clouds for biodefeat applications (i.e. flame temperature and speed). More importantly, no data or analysis describes the fundamental mechanisms involved in sulfur explosions (i.e. diffusion versus kinetically limited combustion). The goal is to obtain fundamental combustion parameters that explain sulfur combustion.

CHAPTER 2

EXPERIMENTAL METHODS

2.1 Setup Overview

The experimental setup, shown in Figure 2.1, was centered around the dust cloud combustion chamber. Details of the chamber and the injection process are described in the following section. Timing was controlled by a delay generator (Stanford Research Systems Model DG335). One channel was used to trigger a mechanical relay/solenoid valve for powder injection and data acquisition equipment (including a Phantom 5, not shown in Figure 2.1) to start recording data. The second channel was used to trigger the fireset (RISI Model FS-43) to initiate the explosion for the appropriate tests. A Quantum Composer delay generator (9520 series) was used when an additonal trigger signal was needed (e.g. to trigger a flash lamp). A suite of data acquisition equipment (Picoscope 4424, Omega OMB-DAQ-3005 thermocouple acquasition system) were used to collect data. The diagnostics and corresponding equipment are explained later in this chapter.

Most of the work in this dissertation involved burning sulfur powder. The main product is sulfur dioxide which is a hazard above 2 ppm [58]. To prevent harmful effects of releasing this gas, a bubbler system was constructed. The Division of Research Safety at UIUC suggested bubbling the sulfur dioxide through a mixture of calcium hydroxide dissolved in water. Following each test, the vacuum pump pulled the gas mixture in the chamber through this bubbler system before being exhausted into the building duct work. The chamber was flushed 5-10 times with air to further dilute any residual sulfur dioxide. Detectors for sulfur dioxide (Industrial Scientific, Gas Badge Plus) and hydrogen sulfide (BW Technologies, Gas Alert Clip 2) were installed in the laboratory to monitor the concentration of harmful gases.

The remaining sections of this chapter are dedicated to describing each

aspect of the setup in detail. These sections include the combustion chamber design, powders and diagnostics used for this investigation. The standard operating procedure is listed in Appendix A.

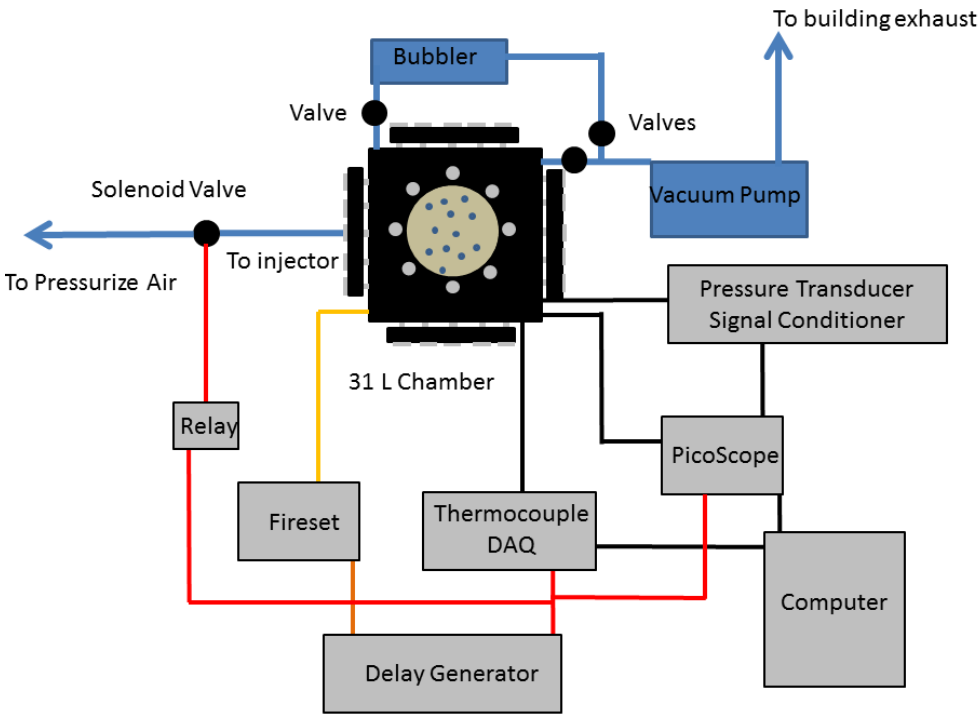

Figure 2.1: Schematic of the whole experimental setup. Blue lines-Gas flow tube, Orange Link-Delay Channel 1, Red Line-Delay Channel 2, Black Line-Data

2.2 Dust Cloud Combustion Chamber

2.2.1 Design Criteria

A constant volume explosion chamber was required for this work, which satisfied several criteria that needed to be fulfilled. The size was crucial for the dust explosion investigation. Large chambers present the difficulty of creating a spatially uniform cloud (and more expensive) while the increased surface area to volume ratio for small chambers increases the heat losses from the flame through the walls. Much of the previous work on dust flames in

the literature has been conducted in a standard 20 L chamber, similar to the size for this work. As such, the chamber should have a similar volume.

One of the more important criterion for this investigation was to design a chamber that maximized optical accessibility. This aspect is a strong contrast to the standard vessels that are typically used. Many of these chambers are spherical which makes it difficult to install large windows. Cylindrical facilities do allow for additional optical access but aside from the flat ends, optical access is somewhat limited due to the curved surface. In addition, the inside of the chamber must be easy to access for cleaning and mounting diagnostic equipment for this work and future studies. Thus, it was decided to design a cube chamber.

Maximizing the viewable portion of the chamber required more consideration than simply putting the largest window into the design. Windows must be easy to replace in case of damage. A modular design would allow that as well as possibility for quartz windows for any experiments that required ultraviolet (UV) transmissive windows. Lastly, the setup needed to be designed to withstand high explosive events.

The larger chambers have been used for high explosive experiments [5]. Their larger volume results in long term pressure levels (i.e. quasi-static pressure or QSP) to be on the order of 1 psig. A smaller volume would increase the QSP, providing larger differences between different explosives. However, not only does this increase in QSP create a larger load on the vessel, but the strength of the blast wave at the walls of the smaller chamber will be greater than that for the large chamber.

Finally, a variety of ports were needed. Gas and vacuum lines were necessary to control the gaseous environment. Several different ports were needed for pressure transducers and other diagnostic equipment. The dust flame experiments required a port to inject powder into the chamber. Ignition electrodes or wires would also be fed through. It was essential for all of these connections to seal under vacuum and pressure for the test preparation and event.

2.2.2 Chamber Design

It was decided to build a cube steel chamber with sides (internally) one foot in length. This size provided the laboratory with a vessel smaller than the existing large blast chambers but similar in size to previous dust explosion work. The total volume of a cube this size is 28.3 L. A door mounted was to the chamber by two heavy duty hinges (Mcmaster part 1852A61) which were welded to the side of the vessel. A rectangular o-ring gland for a size 462 o-ring was put into the inside of the door to seal. Four grade 8 bolts (with complementary nuts and washers) hold the door closed. A computer rendition and photograph of the final chamber are shown in Figures 2.2 and 2.3, respectively. Drawings for all of the components and assemblies in this design are located in the Appendix B.

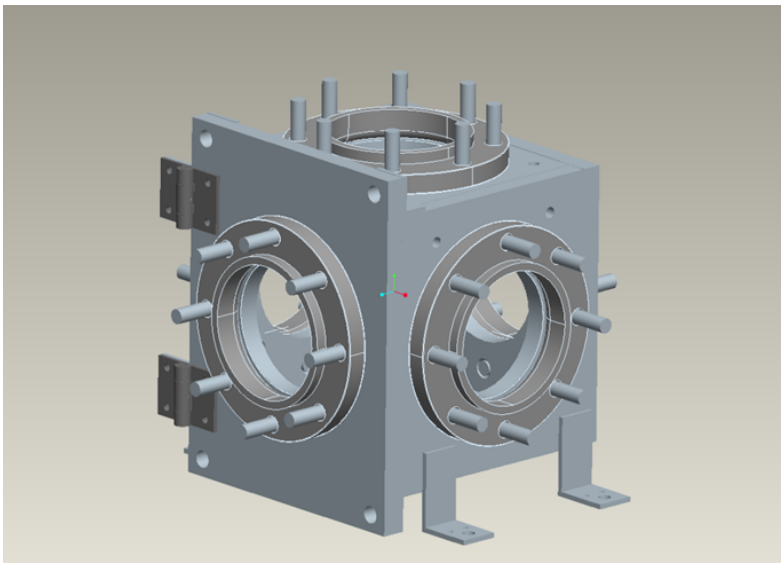

Figure 2.2: Computer rendering of the dust explosion chamber built.

After considering the options, it was decided to use a standard pipe flange to clamp windows between the flange and chamber wall. Since the windows were clamped to the outside, the additional internal volume brought the total chamber volume to 31 L. The largest sized flange that would fit on each size was a size 6, schedule 150 steel flange (Mcmaster part 68095K139). The outer diameter of this flange is 11 inches with an inner diameter of 6.72 inches. Five of the six sides have 8 three inch long, Grade 8, $3/4in - 10$ threaded rods equally spaced on a 9.5 inch diameter which were used to mount the flanges. All five of these windows are 6.7 in diameter which corresponds to the flange

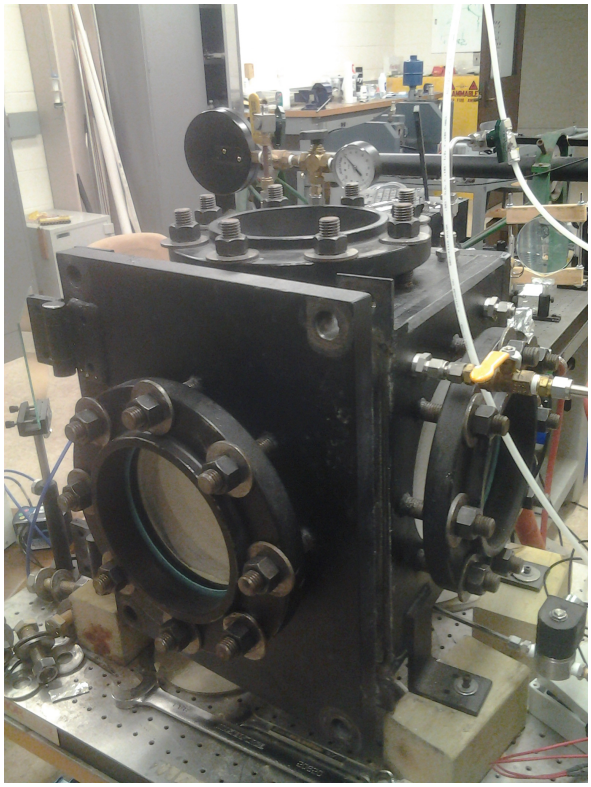

Figure 2.3: Photograph of the experimental facility fully equipped.

inner diameter. A size 168 Buna O-ring with two spliced back-up rings was used to seal the window against the vessel wall.

This design allows for the windows to be swapped easily in case of any damage. Polycarbonate (3/4 in thick) was initially used. This thickness of polycarbonate is very expensive aso it was decided to switch to acrylic (15/16 in thick) windows instead. Each window is 8.5 inches in diameter. Sheets of the clear plastic were purchased form McMaster-Carr and the MechSE water jet was used to cut them into shape. A pipe gasket was placed between the windows and flanges to avoid damaging the windows. Since the windows would likely fail (in the case of high explosive testing) before the steel chamber, windows may be replaced with end cap flanges for increased strength.

Flange end caps were modified to hold quartz windows for any future work involving ultraviolet diagnostics. The adapters were needed because the largest diameter quartz window readily available was 6 inches (Mcmaster part 1357T85). Two of these adapters were fabricated to allow for the possibility of UV absorption spectroscopy measurements. These quartz windows

adapters were made from a schedule 150, size 6, steel end cap (Mcmaster part 68095K169). An o-ring seal was used between the quartz and flange with a custom retaining ring to hold the window in place.

A total of eight $9/16in-18$ ports were put on four sides (two per side) for straight thread to 5/8 in compression Swagelok fittings. The back wall also included a $3/4in-16$ port and a 3/4 NPT port. The 3/4 NPT port allows for quickly evacuating the chamber through an NW-25 vacuum port. The bottom of the chamber has five 1 in diameter holes for multiple purposes. One of the holes was placed in the center of the chamber with the other four holes being placed 3 inches from the center one in each direction (i.e. forward, backwards, left, right). Commercially available aluminum plugs with orings (Duniway part BP-100AL) are used to seal each port when not in use. Two $1/4in-20$ holes were placed next to the center port on the inside and outside of the vessel for mounting of the powder injector and nozzle. The injector will be discussed in further detail below.

Following the design and fabrication of the chamber, it was observed that the door sealing surface was not even. This finish made the o-ring seal on the door ineffective. A polymer epoxy, J.B. Weld, was applied to the sealing surface to create a flatter surface. The cured epoxy was sanded with coarse sand paper to start. A straight edge was used to qualitatively determine the flatness. When the surface appeared even, increasingly finer sandpaper was used to provide a smooth finish.

The repair was effective since following the completion, the chamber leaked at a rate of one seventh of a Torr per minute under vacuum. The leak was more significant under constant pressure (greater than 60 psig). Despite the leak rate under higher pressure, the chamber was able to seal under the conditions imposed by sulfur explosions (less than 60 psig). A noticeable leak could be heard at times for higher pressures that were produced by aluminum explosions (greater than 100 psig). However, since the total explosion event is approximately 200-300 ms long, the uncertainty in the pressure measure for this leak rate (approx. 1 psi/min) was much less than the uncertainty from the noise of the pressure transducer signal (approx. 0.5 psi). It is recommended that the door o-ring be replaced at least after every 20-30 tests. The leak rate increased, possibly from permanant deformation of the o-ring, after that many cycles. It is also suggested that epoxy coating be checked and reapplied as needed. Patching the applied epoxy coating was done during

the course of the work presented in this dissertation. It is recommended that a more permanant solution might be used (i.e. weld filler material).

2.2.3 Powder Injection

Dust explosion experiments of this size require orders of magnitude more powder than the shock tube experiments. Many powders of interest have stoichiometric concentrations within air between 200 and 500 g/m^3 (eg, 280 g/m^3 for sulfur). The mass of powder needed for this 31 L chamber is greater than 10 g, especially since fuel-rich mixtures are also to be studied.

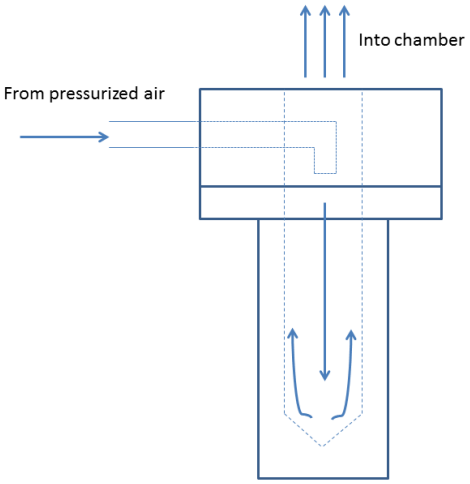

Figure 2.4: Schematic of the powder injection process. The assembly sits underneath the chamber.

A rebound-type injector was built at UIUC based upon a design used by researchers at McGill University. The two piece particle injector is mounted underneath the chambers center port. The first piece is attached to the chamber through $1/4in - 20$ screws. It contains a port on the side that attaches to a compressed air line and $1/4in$ stainless steel tube which extends to the center and is bent 90 degrees downward.

The powder is placed in an aluminum holder with a conical bottom (from a 1 inch drill bit) that attaches to the second piece of the injector with two $1/4in - 20$ screws. This allows for easy removal of the powder holder. The centered $1/4in$ inch tube elbow directs the air burst downward into the

powder holder. The pressurized burst rebounds off the bottom of the powder holder and carries the particles upwards to the chamber and dispersed by a nozzle. Above the port in the center of the chamber, a nozzle with forty, 0.0350 in diameter holes (number 65 drill bit) at a 45 degree angle. The nozzle is held in place by two $1/4in - 20$ screws.

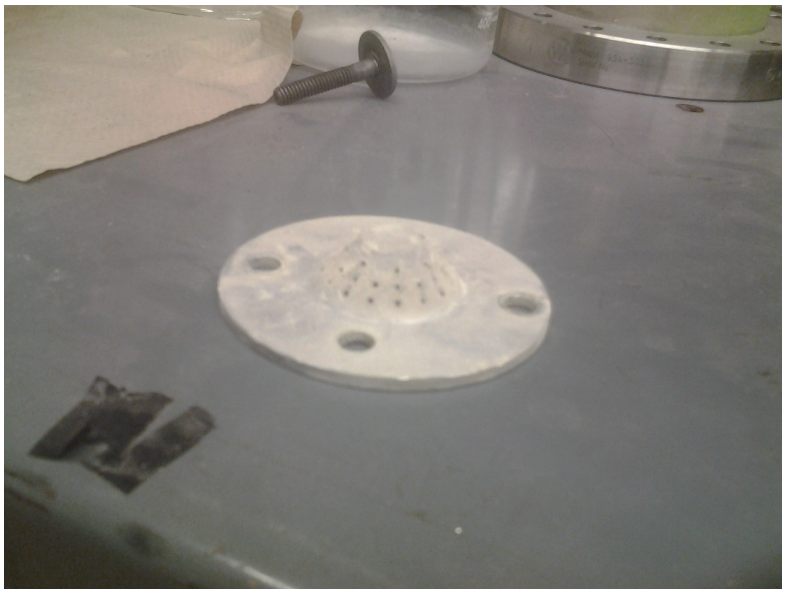

Figure 2.5: Picture of the injection nozzle.

The burst of air (or any other gas) that was needed to force the powder into the vessel increased the pressure within the vessel. At the end of injection, the pressure needs to be at atmospheric pressure (within experimental uncertainty) for the set of tests of interest. Initial tests were done to understand how long this burst should last and at what pressure this event should take place. Standards for the injection process do exist for the standard 20 L and 1 m^3 chambers, but since this chamber is not a standard size or shape (due to the design constraints), it was necessary determine the injection parameters most appropriate for this work. The initial plans for this work also included studying titanium flames. As such, up to 20 g of sulfur and titanium powder were needed to be injected to achieve the concentrations of interest. Furthermore, the same injection conditions (i.e. length and pressure) needed to be used for all experiments to avoid any dependence on the induced turbulence in the measurements. It was determined that one second long burst of air pressurized to 100 psig was able to inject over 90% of the initial powder at the high concentrations. To achieve a final pressure of 1 atmosphere, the

chamber is under slight vacuum of -1 psig.

2.3 Powders Studied

The primary powder used in this study was -325 mesh sulfur purchased from Alfa Aesar. The particle size distribution was determined using the Jeol 6060V scanning electron microscope (SEM) at the Center for Microanalysis of Materials within the Materials Research Laboratory at UIUC. A sample image is shown in Figure 2.6. At least ten particles were measured from each of the ten images taken. Many of the particles were not perfectly spherical. As such, the particle size was measured in two directions. The average of those two measurements was taken as the effective particle diameter. The measured particle size distribution is shown in Figure 2.7. The arithmetic mean and Sauter mean diameters were $23.6\mu m$ and $30.4\mu m$, respectively.

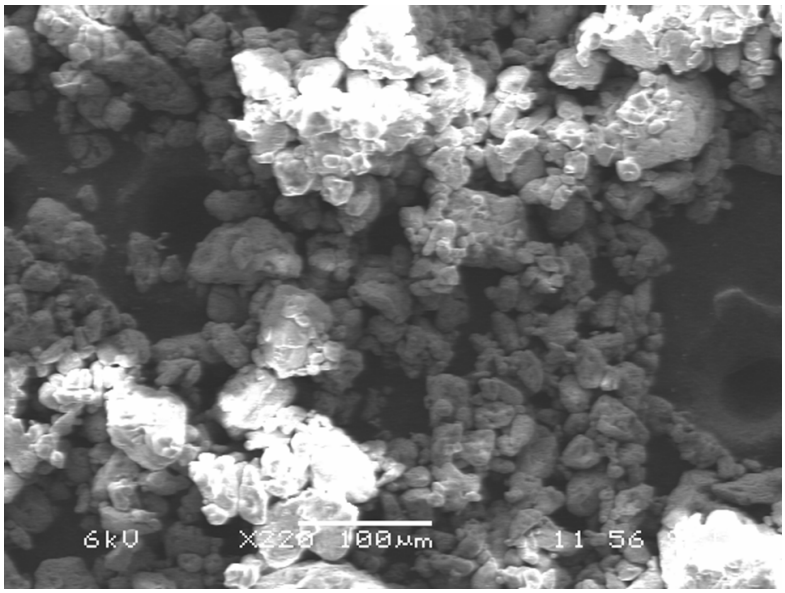

Figure 2.6: Micrograph of the sulfur powder

Three additional powders were tested as anti-caking agents. Magnesium stearate, calcium stearate, and Aerosil 200 were added to sulfur in small amounts. The stearate powders were purchased from Alfa Aesar and Aerosil 200 was obtained from its manufacturer, Evonik.

A size distribution measurement of the magnesium stearate was unsuccessful due to the morphology of the particles. The approach described above

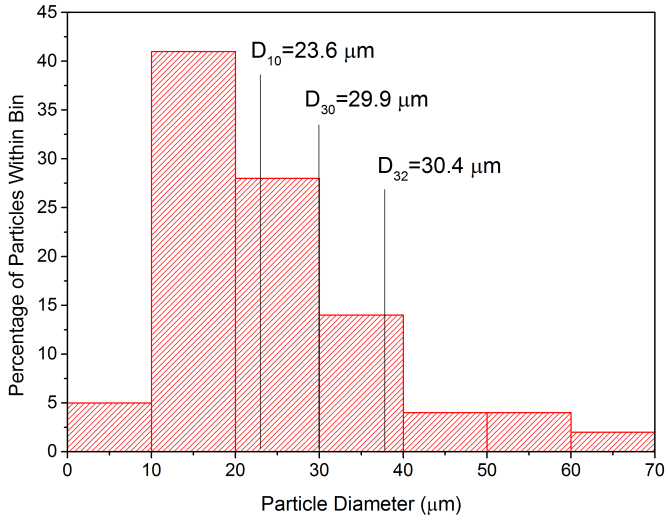

Figure 2.7: Measured size distribution of sulfur powder.

Figure 2.8: Comparison of sulfur powder with (left) and without (right) Aerosil 200.

for the sulfur particles would be inappropriate due to the high aspect ratio of the magnesium stearate powder (Figure 2.9). Aerosil 200 is a submicron, fumed silica powder. The average particle diameter according to the manufacturer is 12 nm. A size distribution was not measured as the particles were too small to be resolved by the SEM. The size distribution of the calcium stearate powder is illustrated in Figure 2.10. The averages are all slightly smaller than those measured for sulfur.

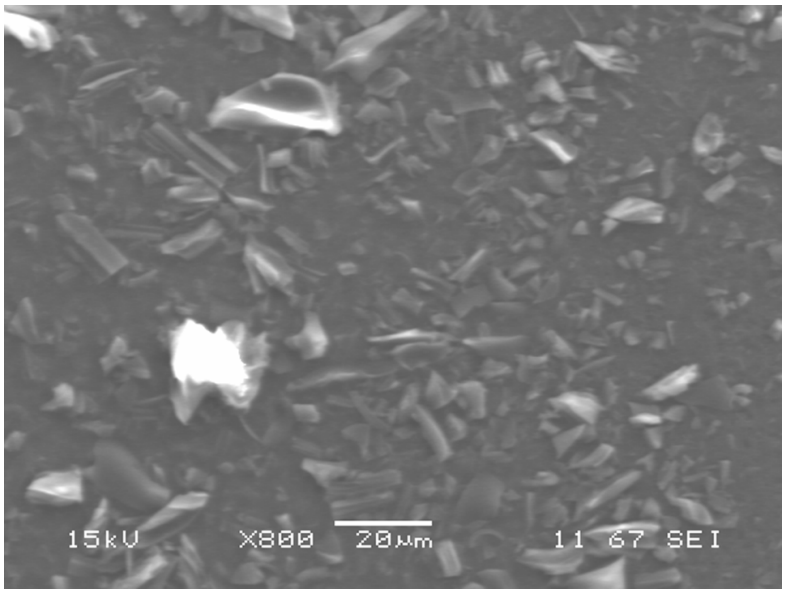

Figure 2.9: Micrograph of magnesium stearate powder

2.4 Ignition Source

The use of several types of ignition sources (hot wire, spark, pyrotechnic) were attempted in this work. However, the hot wire and spark were unable to ignite the mixtures and create self-sustained fuel lean and stoichiometric flames. In addition, the spark ignition source was extremely inconsistent because of the small tolerance for the spacing between the electrodes. If the electrodes were too far apart, the gap would be too wide for electric breakdown to occur. If the electrodes were too close to each other, dust particles would not reach the region (and thus be heated) where the plasma exists. As such, pyrotechnic igniters were decided to be used. These igniters allowed for energy release to be varied easily and resulted in more consistent

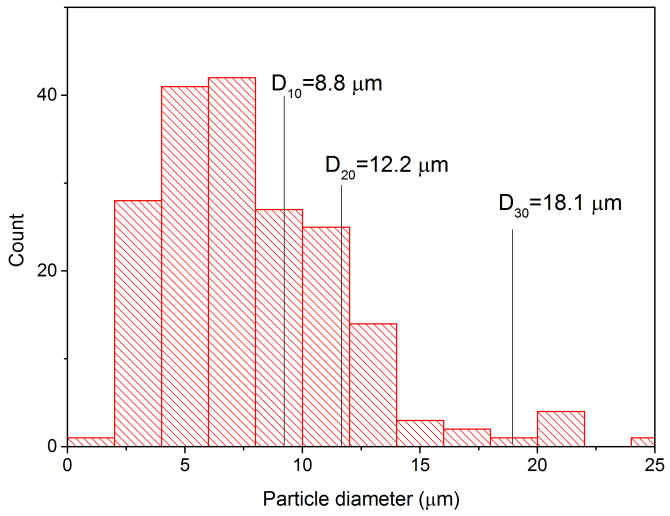

Figure 2.10: Particle size distribution of calcium stearate powder.

ignition of the dust clouds. The disadvantage to using pyrotechnic igniters is the violent nature of them. A small blast wave is created from ignition which creates additional turbulence [28].

The cost of commercial igniters prevented their use for this work so pyrotechnic igniters needed to be made in-house. Using custom made igniters provide the added benefit of having precise control of the energy release. Igniters require several components: trigger mechanism (e.g. hot wire, exploding bridgewire), fuel, oxidizer, and a binder or some method of keeping the ingredients held together. In addition, the disturbance to the cloud should be kept to a minimum in terms magnitude and length (temporally) of the perturbation.

Two types of trigger mechanism were attempted. The first was a hot wire ignition. Initially a mixture of -325 mesh titanium (Micron Metals) and potassium perchlorate (i.e. flash powder) was applied to a nichrome or tungsten wire coated with super glue. However, this method only allowed several milligrams of the mixture. A binder was then added to the pyrotechnic mixture that would permit a larger amount of the mixture to be placed onto the wire. Several different binders were explored: epoxy, rubber cement, and wood glue. The difficulty with this approach was the inability to uniformly mix the flash powder with the binder without using a large amount of the binder. Testing these wires proved to be inconsistent. Sometimes the igniter

did not burn at all while other times it partially burnt. This result is likely due to the amount of binder on the individual igniter. Instead of using a glue to hold the powder in place, a thin casing had to be used.

Thin (approximately 300 micron) plastic casings were created using the Objet Rapid Prototyping machine in the MechSE Rapid Prototyping (RP) Lab. Hollow hemispherical and cylindrical casings were fabricated with 3 mm and 6 mm internal diameter. The cylinders, open at one end, were designed to be 10 and 15 mm tall. Limitations of the Objet and perhaps the type of plastic (the exact material name is proprietary) resulted in the cylindrical casings to be shorter, typically just under 10 mm tall. Nevertheless, these casings were filled with a known amount of flash powder (initially titanium and potassium perchlorate) and an Estes igniter (model rocket igniter part 2301). The open end of the casings was sealed with a small amount of super glue to prevent the igniter and powder from falling out. The two leads from the Estes igniter extended out of the casing so they could be electrically connected to the fireset. The fireset (RISI Model FS-43, Figure 2.11) was used to initiated the igniters. The fireset charged a 1 μF capacitor to 4000 V. The capacitor is discharged when the fireset is triggered either manually or with a 5 V TTL signal. The custom igniters were set off by an exploding bridgewire within the Estes igniter which was covered with a small amount of pyrogen (exact compostions is proprietary). The energy release by the fireset/Estes igniter combination was measured (through bomb calorimetry) to be 4 J with a standard deviation of 0.6 J.

The first casings made were spherical. The idea behind the shape was that it may help in creating a spherical flame front. That hypothesis was never tested because the shape of the casing was more difficult to work with than its cylindrical counterpart. Initial testing of the 6 mm casings showed that the amount of super glue needed to seal the open end resulted in the binder seeping into the powder. That powder was unable to burn due to the excess binder. A sample of this problem is displayed in Figure 2.12. This problem was not seen with the 3 mm diameter casings (Figure 2.13) because significant less glue needed to be used. The 6 mm diameter hemispheres were used to circumvent this issue. The leads from the Estes igniters were used to poke two holes through the hemisphere and onto the model rocket igniters. The hemispheres provided a cap for the larger cylindrical casings. A thin layer of super glue was applied to the outside of the hemisphere (Figure

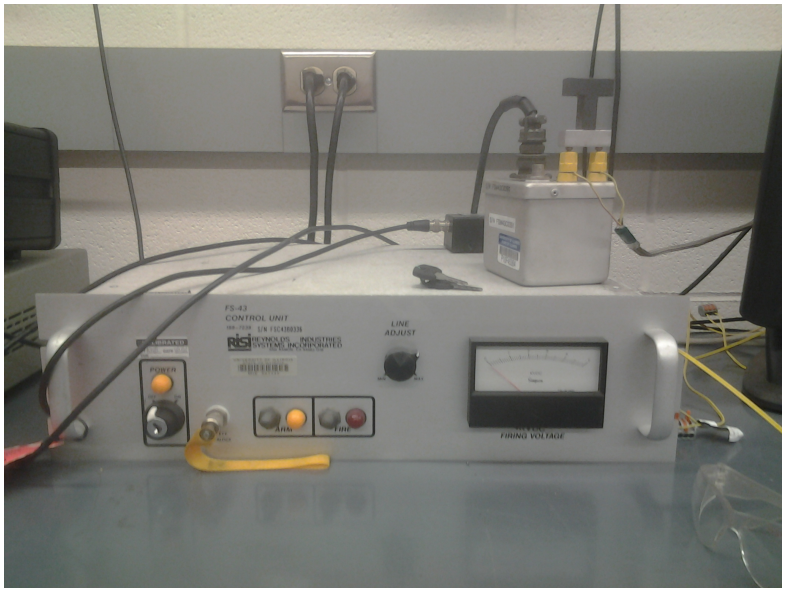

Figure 2.11: Picture of the fireset used to ignite the explosions.

2.14) and placed into the open end of the cylinder. An additional thin layer of super glue was brushed onto the outside of the casing to prevent powder from falling out. The use of a cap resulted in more consistent ignition with most of the powder burning each time.

Tests with both the 3 and 6 mm diameter casings with the titanium flash powder resulted in a relatively long luminous event captured by the Phantom 5 high speed camera. The event lasted, at times, in excess of 60 ms. The length of the event would interfere with the dust explosion and the data collected from each experiment. This powder composition, stoichiometric -325 mesh Ti and potassium perchlorate, needed to be refined such that the ignition event would be shortened as much as possible. Magnesium (-325 mesh, Sigma-Aldrich) and nano-aluminum (80 nm, Nanotechnologies) were both candidates to replace the titanium. A stoichiometric magnesium flash powder was successful in reducing the time of the event in half. However, the nano-aluminum flash powder typically lasted no more than 10 ms and was deemed the best option.

The igniters were then tested within the closed chamber to determine the pressure within the 31 L chamber from the ignition source. The recorded pressure-time data (taken at the chamber wall) revealed that a shock wave was produced by the igniter. The shock was very weak with a peak pressure at most 0.5 psig at the wall. The pressure rise from a blast wave increases the

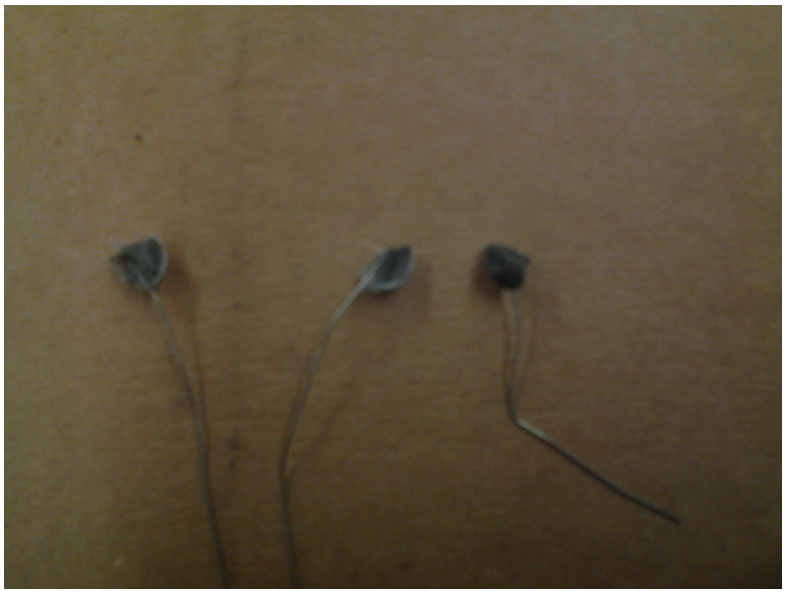

Figure 2.12: Remnants of the spherical casing igniter. Note the large amount of unburnt powder.

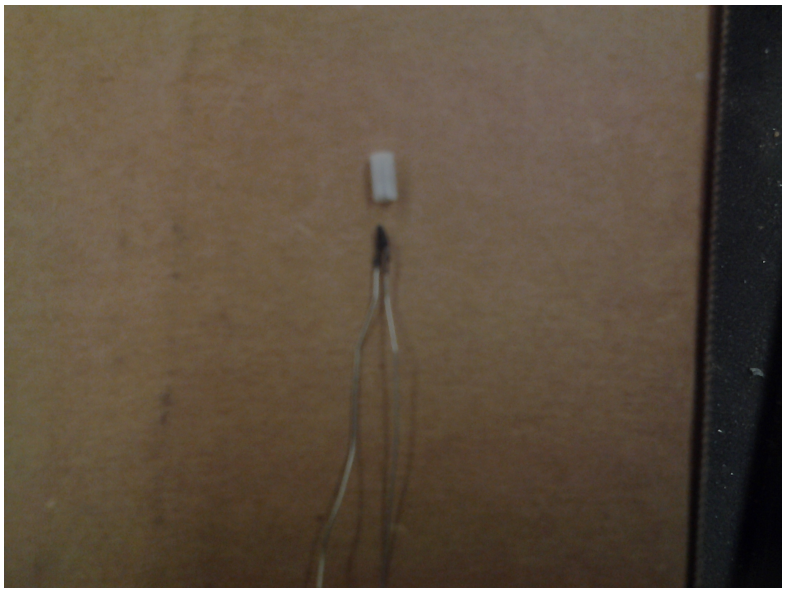

Figure 2.13: Photograph of the 40 J (3 mm diameter) cylindrical igniter being assembled.

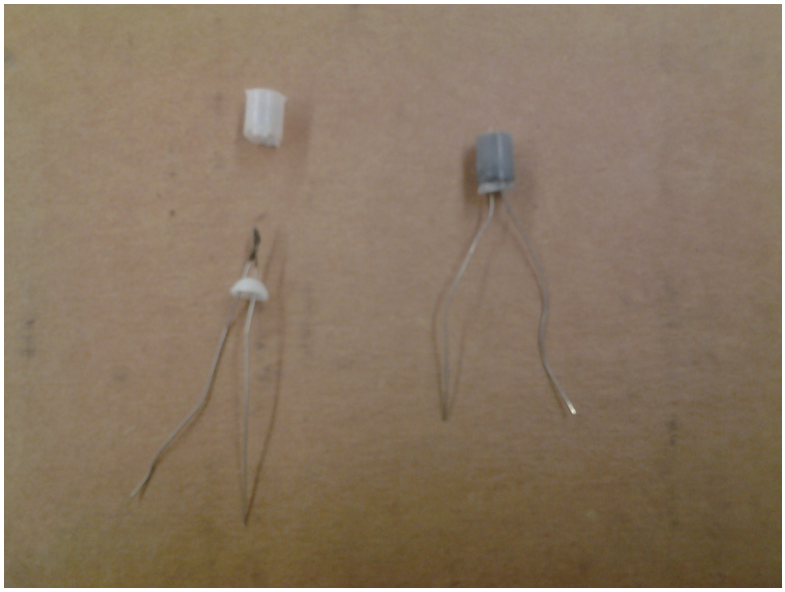

Figure 2.14: The assembly of the 6 mm diameter cylindrical igniter casing.

closer the wave is from the ignition point. No over pressure was measured form the ignition event (i.e. the igniter did not release enough gas or energy to raise the pressure of the chamber). Efforts were taken to reduce the strength of the blast while not minimizing the increase of the duration of the event. Since the nano-aluminum and magnesium flash powders both exhibited evidence of a blast wave, it was decided to work with the nano-aluminum mixture since the burn time was much shorter.

The addition of aluminum oxide (40-50 nm, Alfa Aesar) particles to the mixture was used to decrease the reaction rate in hopes of minimizing the blast. Both igniter sizes were tested. Before the addition of the inert particles, the 3 mm casing provided about 45 J of energy while the 6 mm casing released 200 J. The energy release values include the pyrogen on the Estes igniters (4.0 ± 0.6 J) and are based upon complete reaction of the powder.

All of the experiments conducted in this investigation used one of two igniters. The tests with the 6 mm casings had an average energy release of 200 J (based upon complete combustion). The Estes igniter by itself was used for a lower ignition energy of 4 J. The charges were ignited 400 ms after injection ended. The determination of this time will be discussed in the following chapter.

2.5 Diagnostics

2.5.1 Pressure

Two of the ports in the chamber each house a piezoresistive Kulite pressure transducer. The pressure transducers each were of the XTM-190 Series and are listed of having a time response of 'infinitesimal' according to the manufacturer. The limitation in practice is the sampling rate of the acquisition equipment. One transducer had a 250 psig range but was capable of measuring short term exposures of higher pressures. The design range of the second transducer is unknown. Because of the age of the device, the manufacturer did not have its serial number on file. An Endevco PR Conditioner model 106 was used for the signal conditioner. The conditioner was set to provide a 60% of the full scale output voltage of 1 V. These settings allowed for the correct balance of dynamic range and resolution. Both pressure transducers were set back from the internal wall. The sensitivity to heat and light of the explosive events produced a much higher reading than expected when the tip of the device was flush with the internal wall. In addition, the set back helped prevent dust particles from getting into the sensor. The Picoscope took 200,000 samples over a 2 second time period. Each BNC cable from the signal conditioner was terminated with a 50 Ohm resistor at the Picoscope.

The transducers were calibrated by filling the chamber a known pressure. After the pressure equilibriated, the voltage produced from the transducer was recorded. Calibration was taken from vacuum to approximately 50 psig. The response was linear over the whole range. Sample calibration data (and equation) are shown in Figure 2.16.

2.5.2 Laser Extinction Setup

The light source for two-dimensional laser extinction setup was a continuous wave (CW) 300mW, frequency doubled, Nd:YAG laser ($\lambda = 532nm$, Changchun New Industies Optoelectronics). The laser was sent through an engineered diffuser (Thor Labs part ED1-C20) to expand the beam to approximately a 125 mm diameter. A 127 mm diameter double convex lens with a 240 mm focal length was used to collimate the beam. The resulting beam was essentially uniform and no visible evidence of laser speckle was

Figure 2.15: Photgraph of the Endevco signal conditioner used for the pressure transducers.

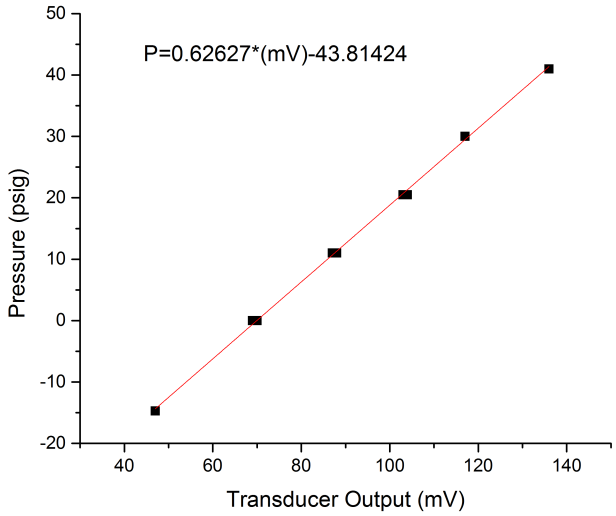

Figure 2.16: Sample of pressure transducer calibration.

observed. The collimated beam was passed through the 31 L chamber before being projected on a screen. A Phantom 5 high speed camera (Vision Research) with an $f/1.2$, 50 mm lens then recorded the image on the screen. The image was 512 pixels by 512 pixels recorded at a rate of 100 frames per second for tests without ignition and 1000 frames per second for the ignition tests. The resulting spatial resolution was approximately 3 pixels/mm. An additional 75 mW CW Nd:YAG laser (Wicked Lasers) was set up transverse to the 125 mm diameter beam. The light transmitted from this laser was recorded on a Thor Labs silicon photodiode. The second laser provided a reference optical depth measurement with a path different from the first. This setup, which was also used for shadowgraph measurements, is shown in Figure 2.17.

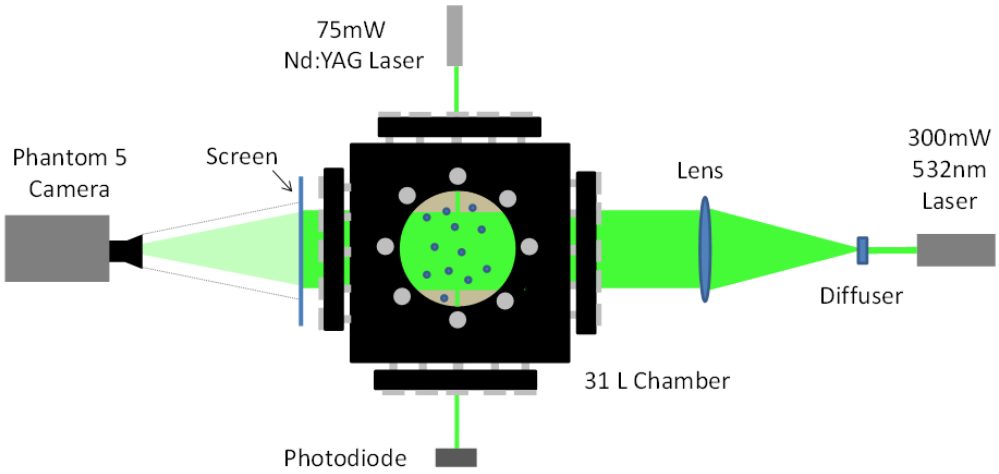

Figure 2.17: Schematic of the laser extinction and laser shadowgraph experimental setups.

Several images taken prior to powder injection were averaged and the intensity, I, of each pixel was used as the incident intensity, I_0, in Beers Law (Equation 2.1). A dark image was subtracted from each of the images just described. The intensity of each pixel in subsequent images allowed for the optical depth (OD) to be determined. This calculation provided a 2-dimensional mapping of the optical depth. Refractive indices of the bulk material were taken to calculate the extinction efficiency, Q_{ext} from Mie theory [59]. The Sauter mean diameter, D_{32}, was determined particle size distribution as discussed above. Evaluation of these physical (e.g. density, ρ) and optical properties of the particles allowed for the particle concentration to be esti-

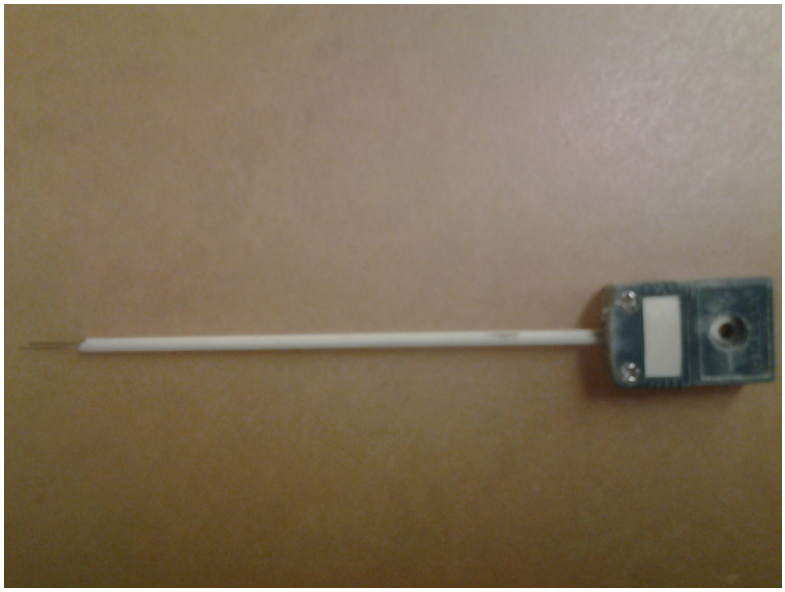

Figure 2.18: Image of an ionization probe.

mated with Equation 2.2 where L is the physical path length (355 mm). The arithmetic mean and standard deviation of the optical depth for all pixels within the illuminated area were calculated to provide a statistical analysis of the uniformity of the cloud.

$$\frac{I}{I_0} = e^{-OD} \tag{2.1}$$

$$OD = \frac{3Q_{ext}LC}{2\rho D_{32}}$$

(2.2)

2.5.3 Flame Speed Measurements

Flame speed was directly measured through the use of ionization probes. The probes consisted of a female R-type thermocouple connector (Omega part SMPW-R/S-MF), a two-bore, 1/8 inch diameter aluminum oxide tube (McMaster part 8746k14), and 0.010 inch diameter tungsten wire. The assembled probe is shown in Figure 2.18.

Two combs of the male thermocouple connecters (Omega part SMPW-

R/S-MF) were placed within the chamber. The connectors were mounted above the 25 mm ports on the left and front (i.e. closest to the door). The thermocouple extension wire (Omega part EXGG-RS-24-50) passed through a hole in an aluminum plug which was subsequently filled with epoxy to prevent leaking. The setup can be seen in Figures 2.19 and 2.20. The distance between the probes was 15.5 mm with an uncertainty of 0.76 mm.

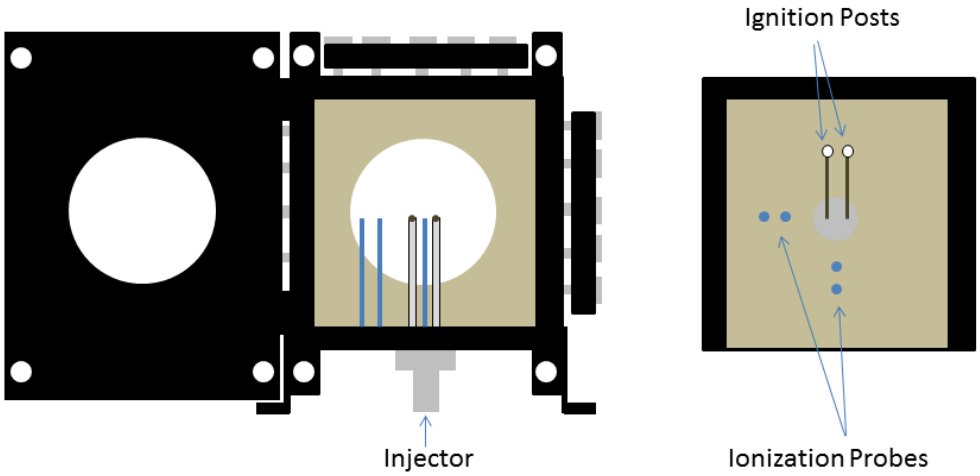

Figure 2.19: Schematic of the flame speed experimental setup.

Figure 2.20: Photograph of inside the chamber following an experiment.

The signals from the probes were conditioned by an operational amplifier

configured in an integration circuit. The output of the circuit was recorded by the Picoscope (again, set to take 200,000 samples over a 2 second time period). The time-of-arrival was taken as the time at which the signal from the ionization probe reached its first minimum as shown in Figure 2.21. The difference in these two times was used to calculate the flame speed. The primary source of uncertainty in this measurement is the use of the minima for the time-of-arrival. Consideration of using other portions of the signal (eg. half of the maximum) as the time-of-arrival produced an uncertainty of 20% of the measured velocity.

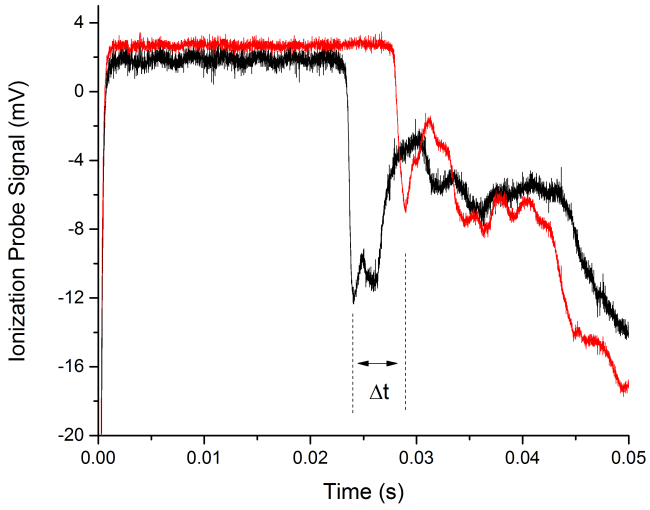

Figure 2.21: Representative signals from a pair of ionization probes.

2.5.4 Temperature Measurements

Temperature measurements were attempted with three different techniques. Thermocouples were used to determine the temperature locally. Pyrometry provided a temperature of the condensed phases within the system, while absorption and emission spectroscopy were used to probe the ground and excited states, respectively, of a gaseous species. Details of these measurements were described in the previous chapter.

For this work 50 μm R-type thermocouples (Omega part P13R-002) were needed for the elevated temperatures. This type of thermocouple is com-

posed of a platinum wire and a 87%/13% platinum-rhodium wire. These precious metals, however, can increase the reaction locally through catalytic effects. The result from the catalytic effects can be an unrealistically high temperature seen by the device [39]. To minimize such effects, the exposed section of the thermocouple was covered in a thin coating of an aluminum oxide spray paint (ZYP Coating, A aerosol). The coated and bare thermocouples were examined in the SEM and are displayed in Figures 2.22 and 2.23.

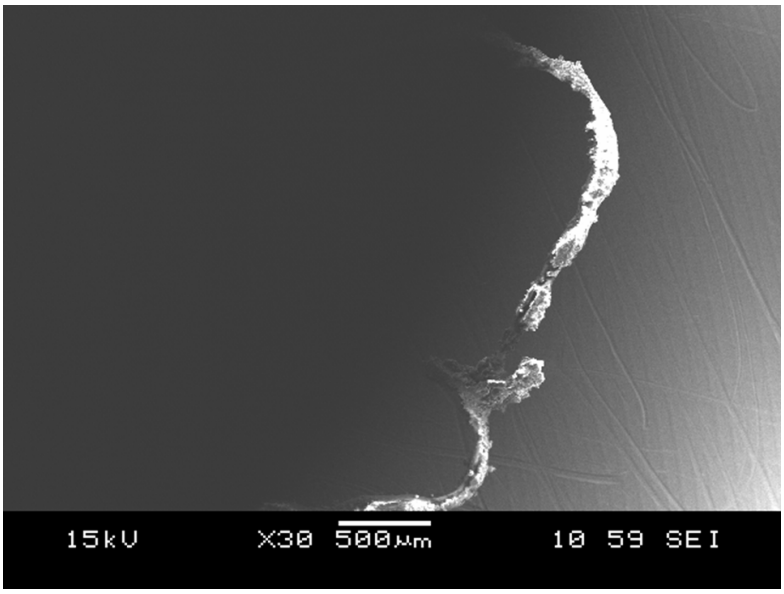

Figure 2.22: Micrograph of a R-type thermocouple coated in alumina paint

Each thermocouple was fed through a two-bore aluminum oxide tube and fastened to a R-type thermocouple connector in the same manner as the ionization probes. A bare and coated thermocouple were each placed within fuel-lean methane-oxygen-argon flame ($\phi = 0.5$). Each thermocouple was place 2.5 cm above the center of the burner. A reading was made after the signal became steady. The alumina-coated probe provided a temperature of 1423 K compared to the 1760 K measured by the uncoated thermocouple. Although the actual temperature was unknown with any certainty, these results demonstrate that the coating influenced the measured temperature.

The disadvantage of applying the coating is that it increased the diameter of the probe, which increased the temporal response. However, a lumped capacitance model for the heat transfer to the thermocouple determined that the time constant (i.e. to reach 62.3% of the final value) is on the order

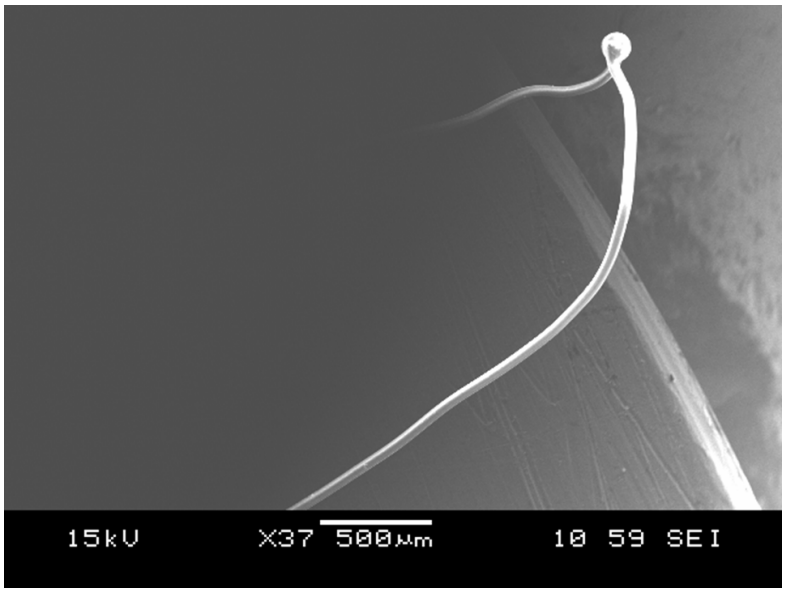

Figure 2.23: Micrograph of a bare R-type thermocouple.

of magnitude of 10 ms. This value is acceptable since the combustion event lasts several hundred milliseconds. However, the increased temporal response will still limit the accuracy of the instantaneous temperature measurement. Therefore, the thermocouple was used for measurements of the peak temperature.

Thermocouples were attached to the connectors within the dust explosion chamber previously described regarding the ionization probes. The thermocouple extension wire was connected to an Omega data acquasition (DAQ) system (Omega part OMB-DAQ-3005). Temperature was sampled every 100 μs for the first 2 seconds of each test. The DAQ system was triggered by a TTL pulse generated by the delay generator.

The elevated temperatures that the thermocouples experience require the output to be corrected for radiative losses. These losses were accounted for by considering an energy balance between convective and radiation heat transfer. Heat is transferred to the thermocouple through convection while the device loses energy through radiation to the walls of the chamber (at 300 K) and by conduction along the leads. Equation 2.3 shows the corrected temperature taken from Ref. [39] where T is temperature, ϵ is total emissivity, σ is the Stefan-Boltzmann constant, d is the diameter of the thermocouple bead, Nu is the Nusselt number, and λ is the conductivity of the thermocouple.

$$T_{corr} = \frac{\epsilon\sigma(T_{meas}^4 - 300^4)d}{Nu\lambda} \tag{2.3}$$

The bead, taken to be 0.2 mm in diameter of the thermocouple was assumed to be a sphere and the Nusselt number to be 2 [60]. The Nusselt number will likely be greater than 2 since the Reynolds (Re) and Prandtl (Pr) numbers will be nonzero. This assumption will result in the maximum correction. The expression for Nu is shown in Equation 2.4 where μ is dynamic viscosity evaluated at the surface (subscript s) and free-stream (subscript ∞) temperatures. The conductivity and emissivity were taken for air and bulk aluminum oxide, respectively, from [61] and evaluated at the appropriate temperatures.

$$Nu = 2 + (0.4Re^{1/2} + 0.06Re^{2/3})Pr^{0.4}(\frac{\mu_\infty}{\mu_s})^{1/4} \tag{2.4}$$

Optical and spectroscopic measurements of temperature were attempted through pyrometry as well as emission and absorption spectroscopy. All of these measurements provide information on the spatially integrated temperaure in at least one direction. Line-of-sight measurements, such as absorption spectroscopy, may provide spatial resolution in the plane normal to the direction of the incident light, but will not provide spatially resolved data along the line-of-sight. Emission spectroscopy and pyrometry will not provide any spatial resolution. Pyrometry measures the temperature of the condensed phases by comparing the thermal background to Planck's equation (with the emissivity included). A three-color pyrometer was used to obtain time-resolved temperature information by monitoring the emission at 700, 825, and 900 nm. The pyrometer was custom built (see Ref. [62]) and uses three Hamamatsu photomultiplier tubes (PMTs) to record the signal. The 700 and 825 nm signals are recorded by a Hamamatsu R928 PMT while an R636-10 PMT was used for the 900 nm signal. Light was collected into a trifurcated fiber optic cable where each of the three branches went to a different PMT. A Stanford Research System (SRS) 300MHz quad preamplifier (SRS model SR445) conditioned each signal. A 50 Ohm termination was used for each channel.

A fiber optic-coupled Ocean Optics Jaz spectrometer was also used for pyrometry measurements. This spectrometer records spectra from 200 to 870 nm. However, due to spectral features from SO, SO_2, and S_2 from the

ultraviolet into the visible region of the spectrum, only the thermal emission in the range of 600 to 850 nm was used to determine the condensed phase temperature. The intensity calibration for both devices was conducted with a tungsten lamp (Ocean Optics LS Cal 1) with a known spectral intensity for the spectral regions studied.

A custom f/7, 444 mm focal length Czerny-Turner spectrometer was used for the absorption and emission spectroscopy portion. A Hamamatsu charged-couple device (S70101007) was used to capture the spectra. Gratings ranging from 300 groove/mm to 4320 groove/mm were used depending on the desired resolution. For the emission measurements, an f/8 quartz lens system collected light from the chamber and focused it upon the 25 μm entrance slit of the spectrometer. When appropriate, a 515 nm long pass filter (Thor Labs part FGL515) was used to prevent second order effects within the spectrometer. This experimental setup is shown in Figure 2.24.

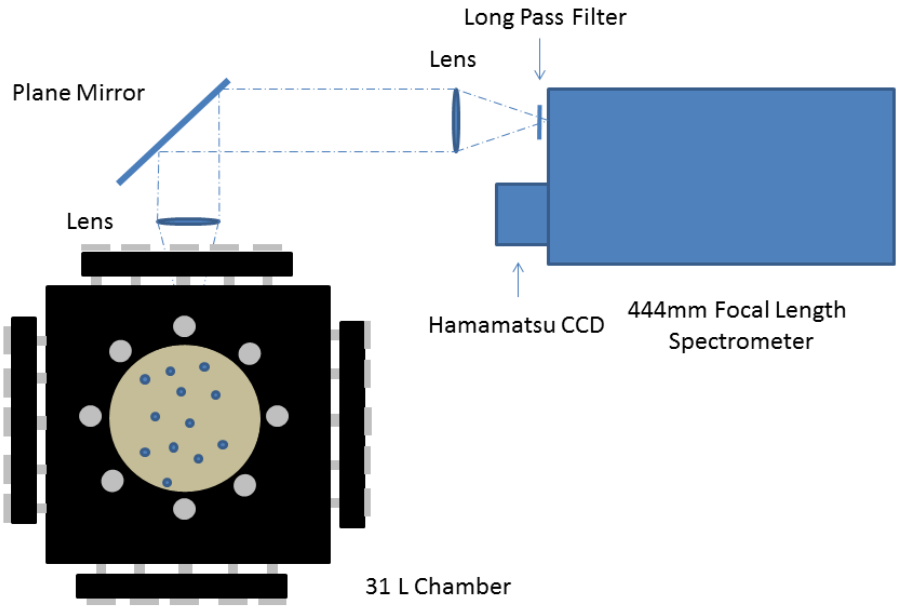

Figure 2.24: Schematic of the emission spectroscopy setup.

The absorption spectroscopy setup is shown in Figure 2.25. The source for the incident radiation was a Xenon flash lamp (Newport model 6427). The flash lamp was triggered by the delay generator and produced a flash with

a pulse FWHM of 60 μs. A quartz lens collimated the light from the lamp which was then passed through the chamber. The transmitted light was then focused onto the slit of the spectrometer. A long pass filter was again used when appropriate.

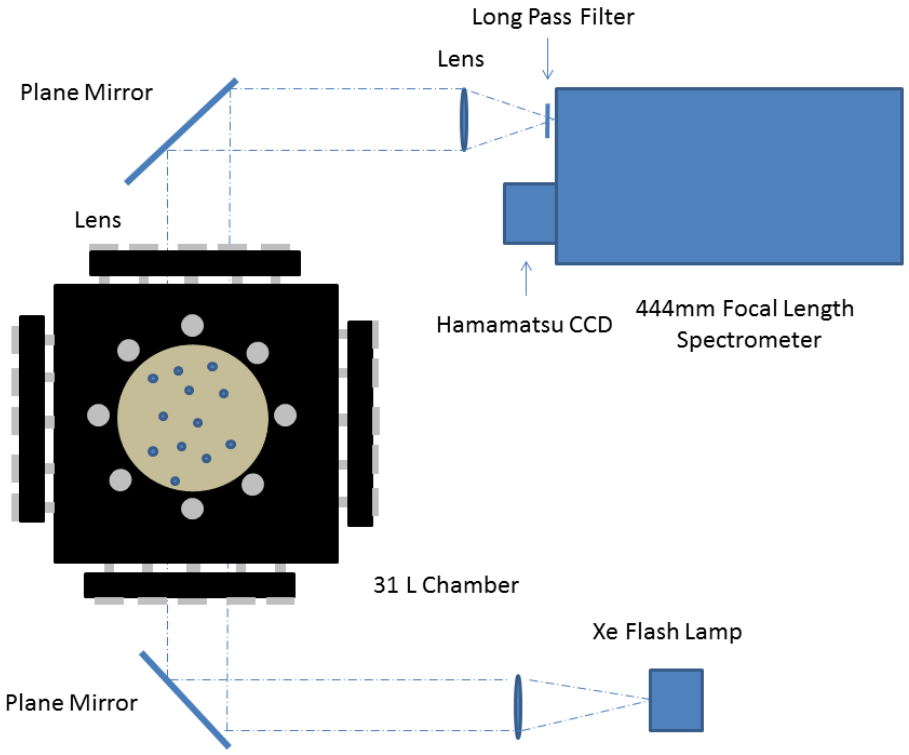

Figure 2.25: Schematic of the absorption spectroscopy setup.

Over the set of experiments conducted, spectra from 200 to 1100 nm were collected (not at once, but in intervals and different resolutions). Spectral calibration was performed with a combination of Hg-Ar and Ne lamps and a variety (ex. Al, Fe) of hollow cathodes lamps depending on the spectral location. A representative spectrum, Figure 2.26, and the pixel-to-wavelength calibration, Figure 2.27, are shown below. The software Origin Pro (version 9) was used to fit the peaks to a Gaussian profile. The center of each fit was used as the location of the atomic peak. The pixel locations were plotted against the wavelength of the appropriate atomic transitions. The spectral location of the atomic transitions were obtained from the National Institute of Standards and Technology (NIST). A second order polynomial was used to determine a mapping of pixel to wavelength. The linear coefficient was approximately equal to the theoretical dispersion. This comparison served

as a way to verify the correct spectral location was being observed. Each fit had a very high degree of correlation.

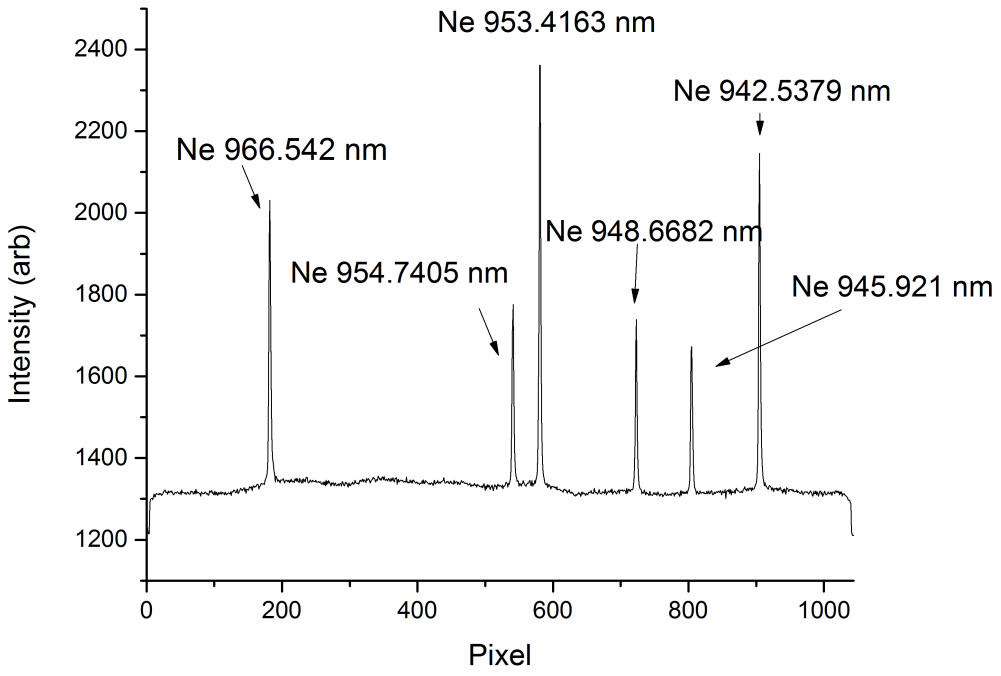

Figure 2.26: Sample spectral calibration from the neon lamp.

Intensity calibration was conducted with a deuterium lamp ($\lambda \leq 300nm$), a tungsten lamp (Ocean Optics LS Cal 1) for the visible, and a NIST traceable blackbody generator set to 1273 K for the near infrared (900 to 1100 nm). The measured intensity at each pixel location (and thus wavelength) was compared to the theoretical intensity at that wavelength from Planck's blackbody equation. Calculating the ratio of the measured and theoretical (the fraction in Equation 2.5) provided the spectral response of the detector (and optical system) with equation 2.5, where I is the intensity where the subscripts corr, th, cal, and meas represent the corrected, theoretical, calibration, and measured intensities. A sample detector response curve is shown in Figure 2.28. Quartz windows were used on the chamber for the work in the UV since the acrylic windows are not UV transmissive. All of the lenses used were quartz.

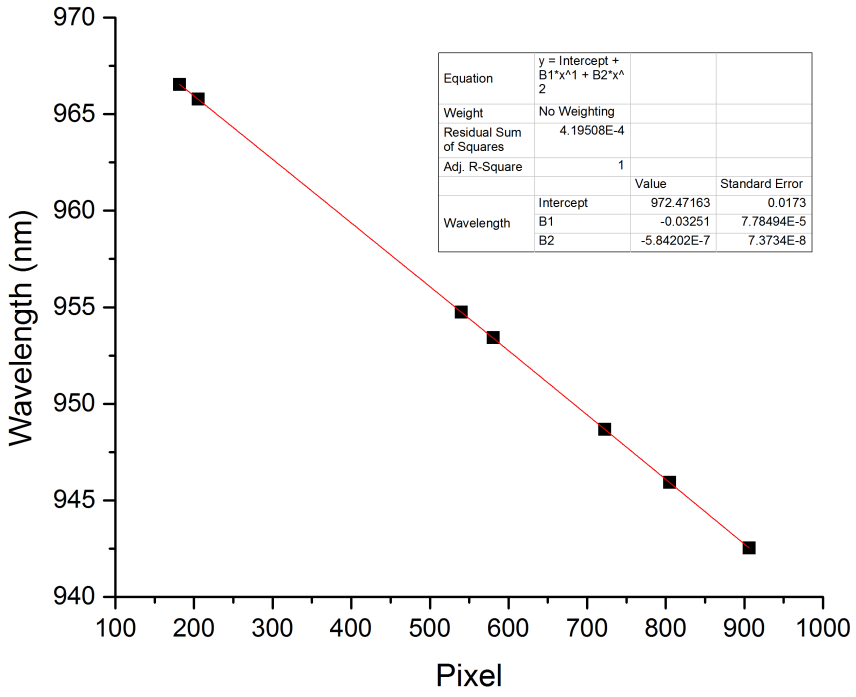

Figure 2.27: Sample spectral calibration pixel-to-wavelength mapping from the neon lamp.

$$I_{corr} = \frac{I_{th}}{I_{cal}} I_{meas} \tag{2.5}$$

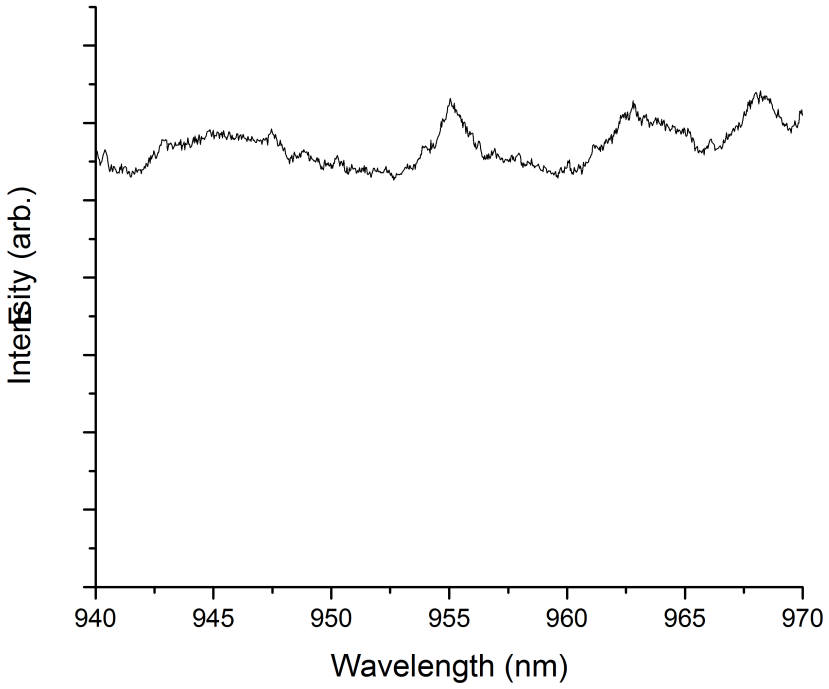

Figure 2.28: Spectral response of the detector determined from the tungsten lamp.

2.6 Experimental Test Conditions

The goal of this work is to understand not only sulfur dust explosions but to gain additional insight with constant volume dust explosions in general. The diagnostics described above were used to answer the questions posed at the end of the previous chapter. The items to be varied are:

1. Powder Dispersal Conditions
   (a) Particle Concentration: 200-560 g/m^3
   (b) Anti-Caking Agent: Calcium stearate, Magnesium stearate, Aerosil 200 (fumed silica)

2. Sulfur Explosions

   (a) Particle Concentration: 280 and 560 g/m^3

   (b) Ignition Energy: 4 and 200 J

   (c) Oxygen Concentration: 10, 21, and 42 percent (by volume)

CHAPTER 3

RESULTS AND DISCUSSION

In this chapter, the experimental results for each of the objectives are presented and discussed. The discussion will begin through the presentation of the work on the sulfur powder dispersal followed by the results of investigating the validity of using pressure-time data to determine flame speed. The chapter will be concluded by a detailed analysis on sulfur dust explosions in terms of the fundamental flame/explosion quantities and the mechanisms involved.

3.1 Powder Dispersal

The first step to creating a dust explosion is dispersing the powder. The powder injection process is very turbulent. In an ideal situation, the cloud would be ignited when it is a perfectly mixed gas-particle suspension and without turbulence. However, neither of these conditions are realistically possible. A method is needed to determine when the aerosol is well-mixed (i.e. as close to uniform as possible). The two-dimensional laser extinction technique described in the previous chapter was used for this purpose.

A known amount of sulfur powder without anti-caking agent, between 6 and 20 grams, was loaded into the particle injector after it was sifted to remove the large (i.e. millimeter to centimeter scale) clumps and agglomerations. The laser extinction measurement was used to determine qualitative and quantitative information about the powder concentration with spatial and temporal resolution. It was observed that the pure sulfur powder had extremely poor dispersion characteristics. The laser extinction data provided valuable images of the event. Large agglomerations were seen to form during the event as highlighted by the red circles in Figure 3.1. Clumps as large as about 10 mm in diameter were seen which is 2-3 orders of magnitude larger

than the primary particle size.

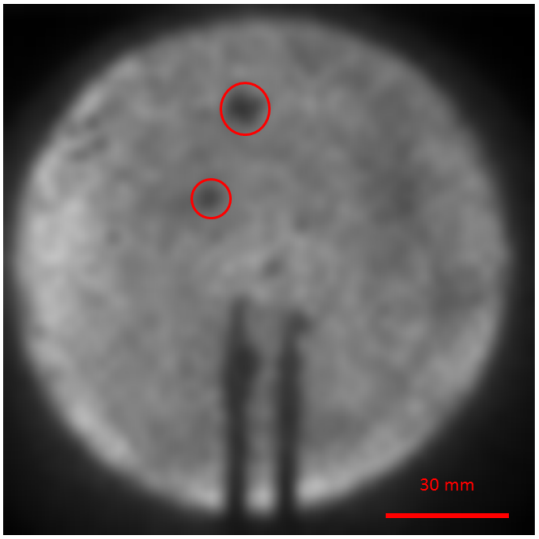

Figure 3.1: Raw image taken from sulfur powder injection. Note the large clumps that have formed.

This result was not unexpected based upon prior experience of handling of the powder. However, it was necessary to conduct similar experiments with a powder that was known to be easier to disperse. Micron-scale metallic powders were observed to be considerably easier to disperse. Titanium flames were initially of interest in conjuction with the sulfur work so it seemed appropriate to use titanium powder for the next set of experiments. These tests provided a method to ensure that the difficulty dispersing sulfur was in fact due to the nature of sulfur powder and not the injection process and/or the experimental setup.

3.1.1 Titanium Dust Dispersal

Optical depths of titanium clouds were measured ranging from about 100 (fuel-lean) to 700 (fuel-rich) g/m^3 . The stoichiometric concentration for a titanium-air flame is 410 g/m^3. Representative images and optical depth contours from a 406 g/m^3 titanium dust cloud are shown in Figure 3.2. The laser lit background quickly darkens as more powder entered the field-of-view. Ignition wire feedthrough posts casts the shadow seen in the bottom half of the images. The bottom row displays the contours of optical depth for a 406

g/m^3 titanium particle cloud towards the end of injection and after injection ended. As described by Equation 2.2, the optical depth is directly proportional to particle concentration, so that uniformity in terms of optical depth is equivalent from a qualitative point-of-view to uniformity of the particle concentration. Approximately 200 ms after injection ends, it was seen qualitatively that the optical depth became more uniform spatially, indicating that the suspension was well mixed as turbulence began to decay. It should be noted that this measurement is a line-of-sight technique, meaning that the measured concentrations are averaged over the line-of-sight perpendicular to the plane of the images.

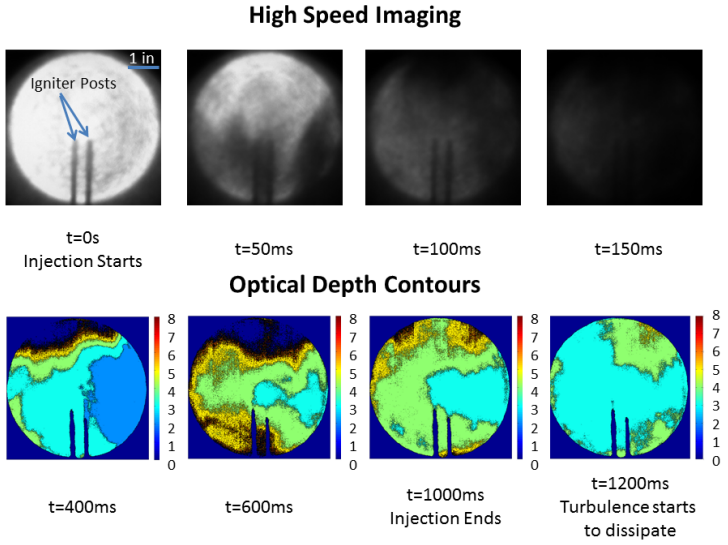

Figure 3.2: Images and optical depth contours taken from dispersal of titanium powder (406 g/m^3).

A statistical approach, similar to Kalejaiye et al. [26], was used for a quantitative analysis of the spatial distribution. For each frame, the mean and standard deviation of the optical depth over all of the pixels were calculated. By applying Equation 2.2, the mean and standard deviation of particle concentration were obtained and are displayed in Figures 3.3 and 3.4, respectively. The mean values are initially higher than the expected concentration before decreasing. The mean concentration started to converge but with a slight decay in concentration. This decay was likely due to particle settling. A similar trend was seen qualitatively for the standard deviation values. The decrease in standard deviation is indicative of a higher degree of spatial

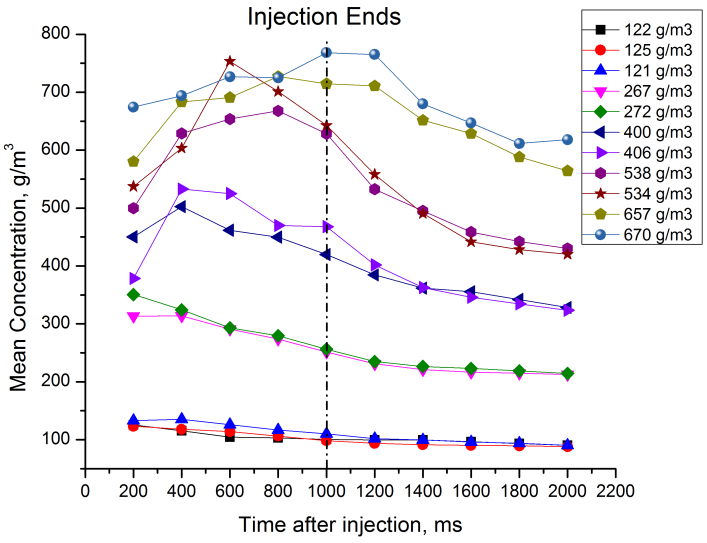

Figure 3.3: Mean concentrations of titanium as a function of time for a range of powder loadings.

uniformity. Moreover, the decrease in these values (i.e. mean and standard deviation) occured at the same time as the increase in uniformity seen in Figure 3.2. This result confirms the observation seen by the qualitative results above.

The measured mean concentration was approximately equal to the expected concentration at a time of 300-400 ms after injection ended. The expected concentration was calculated based upon the amount of powder injected. The combination of the cloud becoming more uniform and the mean concentration reaching the expected values makes this time range most appropriate to ignite the cloud. The measured mean concentrations for all the conditions tested are shown graphically in Figure 3.5 at 400 ms after injection ended. Note that the uncertainty bars are based upon statistical uncertainty and not experimental error. Each concentration was run at least twice, and the run to run variation was within the statistical uncertainty. This consistency was also observed from the time-resolved plots in Figures 3.3 and 3.4.

Increased uncertainty for the particle concentration is due to two factors. First, as the optical depth increases, it becomes more difficult to distinguish small differences in concentration, due to the logarithmic nature of Beers Law. Secondly, optically thicker clouds yield lower counts for each pixel,

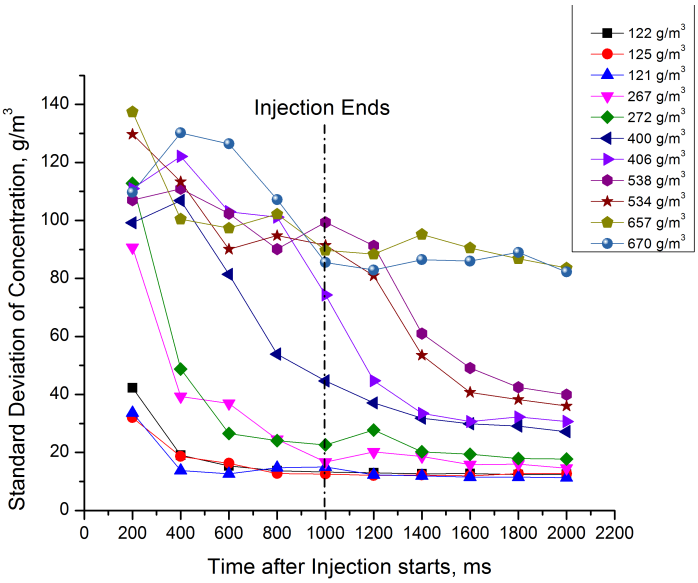

Figure 3.4: Standard deviation of titanium powder concentration.

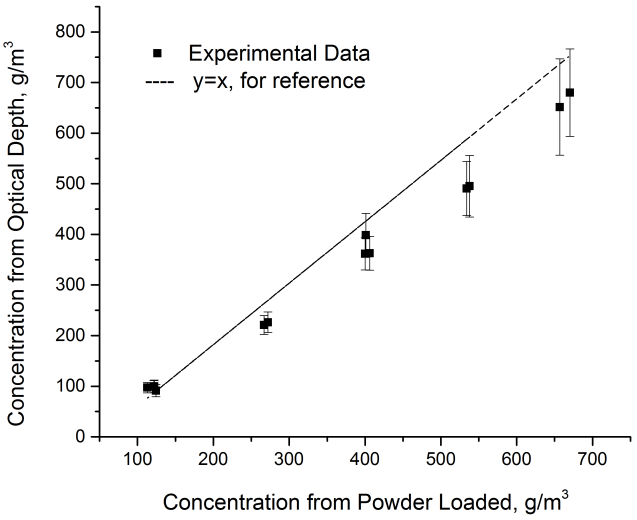

Figure 3.5: Mean concentrations of titanium at 400ms after injection has ended.

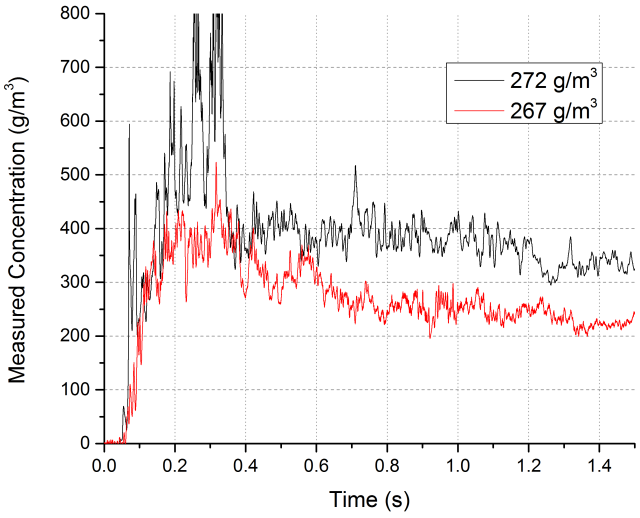

Figure 3.6: Single line-of-sight measurements for titanium dispersal.

reducing the signal-to-noise ratio.

Extinction measurements from the 75 mW laser provided a measurement along a single line-of-sight perpendicular to the two-dimensional measurement. The single line-of-sight, however, yielded limited information due to shot-to-shot uncertainty. This variation is displayed in Figure 3.6. These two measurements displayed a difference of 100 g/m^3 compared to a difference of less than 10 g/m^3 for the mean concentrations discussed above for similar concentrations.

The only difference in the two paths was the position of the wire feedthrough for the igniter. To account for any effect these posts may have on the injection process or flow field, the wire feed through was moved to a different position such that the new path of the 300 mW laser was equivalent to the path perpendicular to the original. Tests of two concentrations (100 and 400 g/m^3) were made with this modified setup and the mean concentrations were well within the experimental uncertainty and are among the data displayed in Figure 3.5. This result suggests that the path direction has a minimal effect and that some degree of symmetry exists in regards to the uniformity of the cloud.

The two-dimensional measurement contains many (approximately 100,000) lines-of-sight. Each pixel represents an individual line-of-sight so that the this approach produces a statistically significant number of samples (i.e. each

pixel provides a measurement). Therefore, the data provide a mean concentration that is statistically representative of the particle concentration within the system. A single line-of-sight measurement does not necessarily provide an accurate measure of the particle concentration or uniformity. It is recommended that as many lines-of-sight be used as possible, especially if the uniformity of the particle cloud is requireed.

3.1.2 Sulfur

The approached used for the titanium dust provides the necessary data to determine the effectiveness of sulfur powder dispersion. The titanium work also confirmed that the problems seen initially during injection were caused by the sulfur powder and not the experimental setup or approach.

Pure sulfur powder was injected into the chamber to obtain a baseline measurement of the mean concentrations measured. The optical depth of the sulfur clouds changed very little over a range of concentrations from 80 to 500 g/m^3. The mean particle concentrations at 400 ms after injection ended are plotted in Figure 3.7 as the red circles. These observations were likely affected by particle agglomeration. The measurement from the lowest concentration yields a concentration close to the expected value. As the particle loading increases, so does the discrepancy. We believe that this result was due to the average interparticle distance. Higher particle concentrations will result in smaller distances between the particles making it more probable for the particles to agglomerate from electrostatic forces. The strength of the electrostatic forces and the tendency to agglomerate may play a role in determining the dustiness of a powder in addition to the reasons given by Klippel et al. [63].

Clearly, the poor dispersion characteristics of sulfur, as described here quantitatively and above qualitatively, are not satisfactory for dust explosion experiments. The use of three anti-caking agents (calcium stearate, magnesium stearate, and Aerosil 200) were tested to improve the dispersion characteristics. The anti-caking agent was combined with sulfur powder and mixed within a tumbler for 3 hours to ensure uniformity.

Calcium stearate was tested first. It was observed that by adding 5% (by mass) of the powder to sulfur, the measured concentration was much

closer to the expected concentration than without any anti-caking agent, as illustrated in Figure 3.7. However, the deviation still increased as the particle concentration increased. The calcium stearate content was then doubled to try to improve the dispersion at the higher concentrations. This change appeared to help, although it was decided that this large amount of anti-caking agent was too much. The goal was to add only a small amount of powder, such that the flame would not be augmented by the heat release or sink from the additional powder. One percent by mass of the calcium stearate was added to the sulfur, but the measured concentration was significantly lower than the expected.

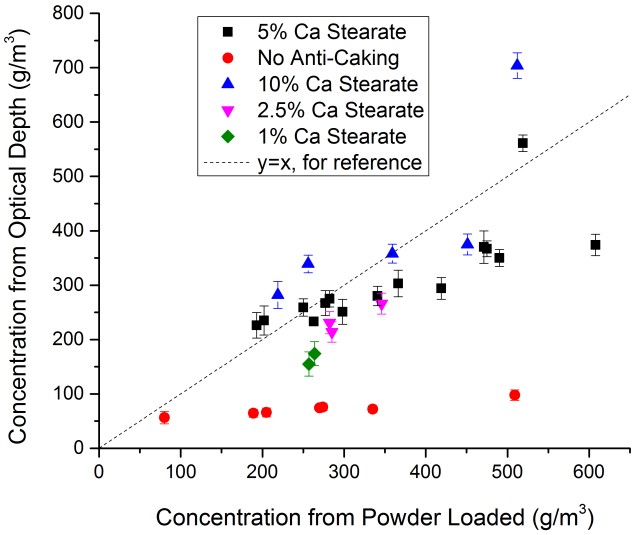

Figure 3.7: Measured particle concentrations with the addition of varying amounts of calcium stearate.

The magnesium stearate additive was examined next, starting at one percent by mass. Near 250 g/m^3 the measured mean concentration was near the expected. The performance dropped off considerably near 500 g/m^3. A similar observation was made after the magnesium stearate concentrations was increased to 5% by mass. These data points are shown in Figure 3.8. It took ten percent of the magnesium stearate to achieve proper dispersion. Again, this was considered too much.

The third additive tested was the submicron Aerosil 200 powder. Initial tests used 1% by mass of the anti-caking agent. Qualitative observations of the dispersed sulfur and Aerosil 200 mixture showed a significant improve-

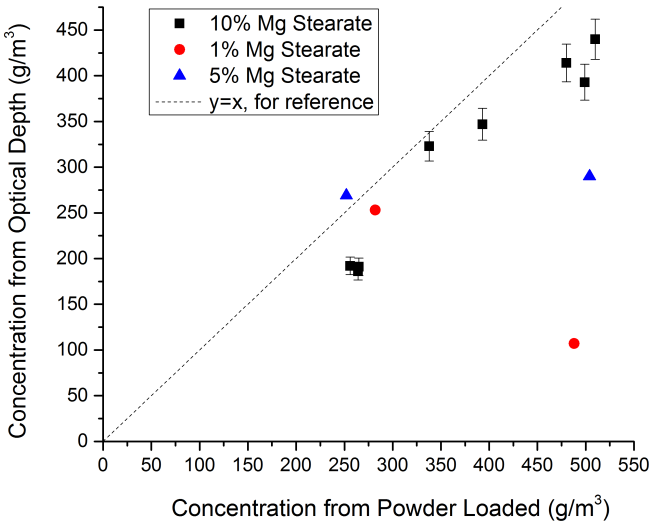

Figure 3.8: Measurements of the particle concentration with the addition of magnesium stearate.

ment. The laser extinction measurements confirmed the previous observations. The measured mean concentrations at 400 ms after injection ends for the mixtures are also shown in Figure 3.9. Lower concentrations showed excellent agreement to the expected values. As the concentration increased past stoichiometric (280 g/m^3), a slight disagreement is seen. The disagreement grows at particle loadings greater than the location of this inflection point.

A mixture of 3% by mass of Aerosil 200 and sulfur was tested to attempt to move this inflection point to higher concentrations. Surprisingly, the experiments showed that the increase in the anti-caking agent increased the deviation at concentrations near 500 g/m^3. A similar phenomena was observed by Gold et al. [64]. We speculate that the increase in Aerosil 200 increases the likelihood of agglomerations due to an increase of surface area. The anti-caking particles are on the order of 10 nm in diameter and have high specific surface area. From handling the pure Aerosil, we have noticed that the powder very easily sticks to the spatula, walls, etc. and thus believe that was the reason for the increase agglomerations.

The injection pressure was increased to 600 psig to help break up the agglomerations at the higher concentrations. The mass of the air injected was held constant so that the injection time was decreased to 250 ms. The

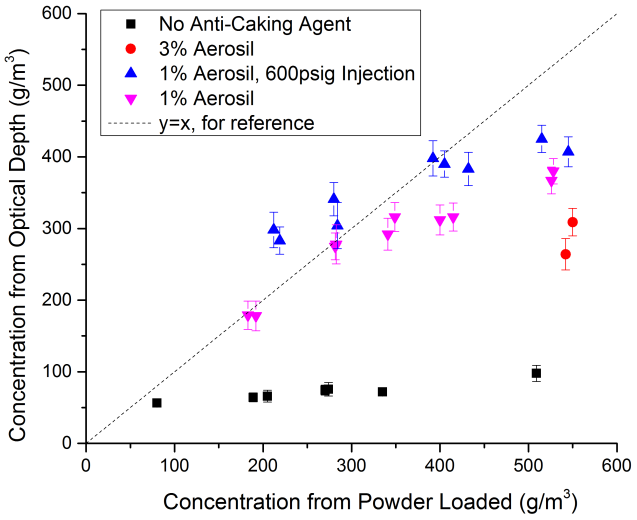

Figure 3.9: Measured particle concentration with small amounts of Aerosil 200 added to the sulfur powder.

higher pressure appeared to help significantly at the high particle loadings. However, we observed an apparent increase in the measured concentration at low powder loadings, while previous results showed excellent agreement. Because of this result, it is concluded that the increase seen at all concentrations is due to particles breaking up during injection [26]. The fracturing decreases the Sauter mean diameter of the particles in the suspension. Since the size parameter from Mie Theory is much greater than unity, the extinction efficiency is still close to the limiting value of two [59]. Therefore, by using Equations 2.2, it can be shown that the optical depth increases because the only variable that changes is the Sauter mean diameter. But, the lack of post experiment analysis makes it difficult to verify or determine to how much fracturing occurred.

The addition of each of the anti-caking agents resulted in some degree of improvement for sulfur dust dispersion. It was seen that the use of Aerosil 200 provided the best performance and should be used to disperse sulfur powder effectively. This conclusion is based upon the combination of uniformity, as described above, and the amount of anti-caking agent needed to achieve that degree of uniformity. This result is likely due to the ultrafine nature of the Aerosil powder. Gold et al. [64] determined the fineness of similar fumed silica particles to be the reason for the improved flowaility in their work,

however, they did not provide an explanation. It is conjectured that the size of the Aerosil particles allows the anti-caking agent to partially coat the sulfur particles more effectively than the much larger calcium and magnesium stearate powders. The Aerosil 200-sulfur mixture was examined in the SEM. The SEM was unable to provide the necessary resolution to observe how well the sulfur particles were coated so this hypothesis was unable to be verified.

This measurement is limited by the fact that this technique only provides line-of-sight averaged concentration values. It is difficult, if not impossible, to extract full three dimensional information from these data. Techniques like Abel deconvolution may not be appropriate because the concentration may not be radially symmetric [65]. If the cloud is symmetric, the work by Young [66] has shown that Abel deconvolution may be used even in these optically thick conditions. The use of internal probes can provide localized information, but they are also intrusive. Without optical access, using internal probes is the only option. The lack of optical access for chambers used in the literature partly do not contain the same amount of optical access as the chamber used here and may be the reason, at least in part, why the approach used here has not been used.

One last aspect of this measurement is worthy of discussion. The extinction efficient used to calculate the particle concentration is equal to 2 from Mie theory. The value of 2 physically means that a cross-sectional area twice that of the geometric cross-section of a particle affects light passing through it, which is a result of diffraction. It is possible that the diffracted light still reaches the screen but at a different location on the screen than the one expected from the initial direction of the light. We believe that the large optical depths created by the dust cloud reduce the likelihood of the diffracted light reaching the screen. Multiple scattering will essential increase the physical path length and hence reduce the amount of light transmitted. Although we do believe this effect did not significantly affect the measurements, it is worth investigating this issue in the future.

3.2 Pressure-Time Validity

Flame speeds can be measured multiple ways, as discussed in the Introduction. It was observed from some preliminary work that methods like tracking

the emission from the flame front or through shadowgraph were unable to provide quantitative results. The multiple scattering from the cloud between the detector and the flame front creates a diffuse light source. The large optical depths make it hard to track the flame front accurately with schlieren or shadowgraph. The simplicity of using pressure data to measure speed should avoid the problems experienced with other techniques and can even be used in chambers without optical access.

It was decided to use ionizaton probes, similar to the work of Nair and Gupta [55], but for dust flames instead of the gaseous flames that they studied. Prior to performing sulfur tests with the ionization probes, several experiments with a premixed, stoichiometric methane-air flame were conducted. These experiments allowed for the technique to be verified before use with the sulfur powder. Laser shadowgraph was used to confirm the times-of-arrival measured by the ionization probes.

The laser shadowgraph setup used a continuous wave, frequency-doubled Nd:YAG laser (Chingchun Industries) and a Phantom 5 high speed camera (Vision Research). The beam was expanded with an engineered diffuser (Thor Labs) and collimated with 120mm diameter, 240mm focal length lens (Anchor Optics). The methane and air were mixed within the 31 L chamber. The mixture was left for approximately 10 minutes to ensure a homogeneous mixture and to let turbulence from the filling process dissipate. A 4 J pyrotechnic igniter (Estes) was used to initiate the reaction. Although this igniter released more energy than needed to ignite a methane flame [9], it was used for consistency, since it would be used for the sulfur dust flames.

The flame radius for the methane-air flame is plotted as a function of time for both the shadowgraph and ionization probe data in Figure 3.10. The times-of-arrival indicated by the ionization probes were taken at the point where the ionization probe signal peaked, as mentioned in the previous chapter. The data points in the steady flame propagating region were fit to a line where the slope of that line was the flame speed. It is clear from Figure 3.10 that both techniques provide similar result of 2.60 and 2.63 m/s for the ionization probes and shadowgraph, respectively.

A perfectly stirred reactor (PSR) code from Cantera was used to calculate the ratio of the densities for the burnt and unburnt mixtures. The GRI Mechanism was used for the chemical kinetics data [67]. From mass continuity, the laminar flame speed is defined as the product of the measured flame

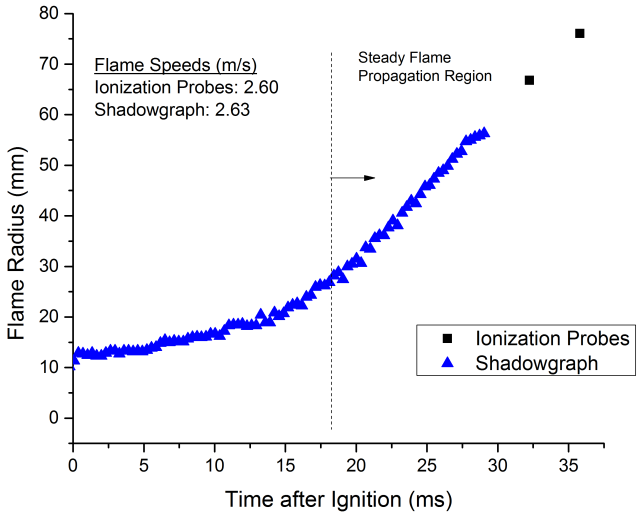

Figure 3.10: Radius of a stoichiometric methane-air flame as a function of time. The flame speed is taken from the slope (mm/ms).

speed and the ratio of the burnt to unburnt mixture densities as shown in Equation 1.8. The laminar flame speed was determined to be approximately 35 cm/s for both measurements. This value is in good agreement with the flame speed of 34 cm/s as reported by Bradley and Andrews [68].

Following the methane tests, two concentrations of the sulfur mixture were tested. A near stoichiometric concentration of $264 \pm 34 g/m^3$ and a fuel-rich condition of $498 \pm 53 g/m^3$ were ignited with a pyrotechnic igniter. Both 4 J and 200 J igniters were used to explore any effect of ignition energy on the measurements. Each of the four combinations of the tests was repeated at least eight times. The uncertainty in the concentration is due to the distribution of the measured powder mass injected.

A pair of ionization probe traces from a sulfur flame is shown in Figure 3.11. The time when the first voltage drop reaches a minimum for each trace was taken as the time when the flame front reached the probe. Laser shadowgraph confirmed this arrival qualitatively. The front, indicated by the left arrow in Figure 3.12, was seen to reach the probe location, as shown by the right arrow, at the same time (within the temporal resolution of the camera) as the voltage drop. The Δt shown in Figure 3.11 was used to calculate the flame speed. An uncertainty of 20% of the nominal value was associated with each measurement which is mostly due to the time-of-arrival

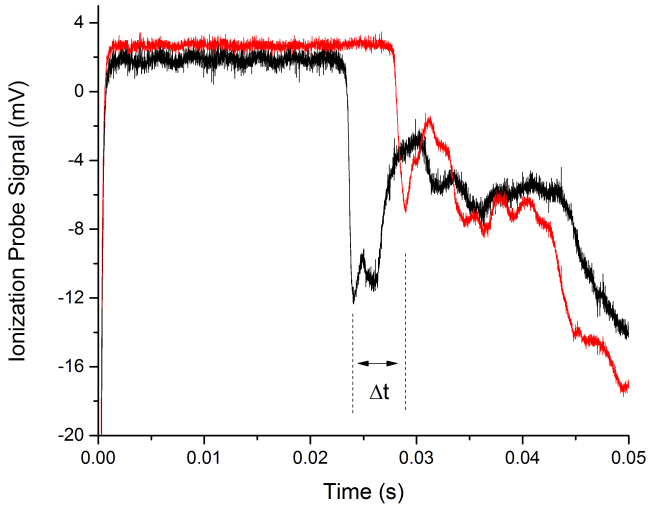

Figure 3.11: Representative voltage traces from the ionization probes from a sulfur flame.

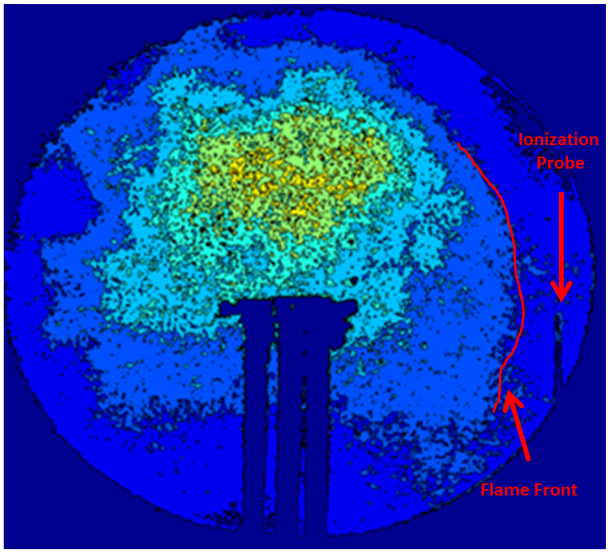

Figure 3.12: Shadowgraph image taken from a sulfur explosion. The particle concentration was approximately $280 g/m^3$.

measurement. The density corrections were calculated using Cantera [69] and the SOx mechanism from the University of Leeds [35].

The flame speeds measured by the ionization probes for all conditions are shown in Figure 3.13. A large amount of data scatter is seen for both ignition energies and concentrations. It is concluded that the range of flame speeds observed is at least in part due to the turbulence that remained in the system after the injection process. This point is supported by the asymmetry observed by the highly irregular front seen by the shadowgraph image, Figure 3.12. The flame speeds measured in each direction for a single experiment were observed to vary more than 50% in some cases. Moreover, there were instances where the signal from two probes in a single pair would indicate the flame had arrived at the same time. This observation is likely due to the flame approaching the ionization probe pair from a side-on approach rather than head-on as would be expected for a spherical flame.

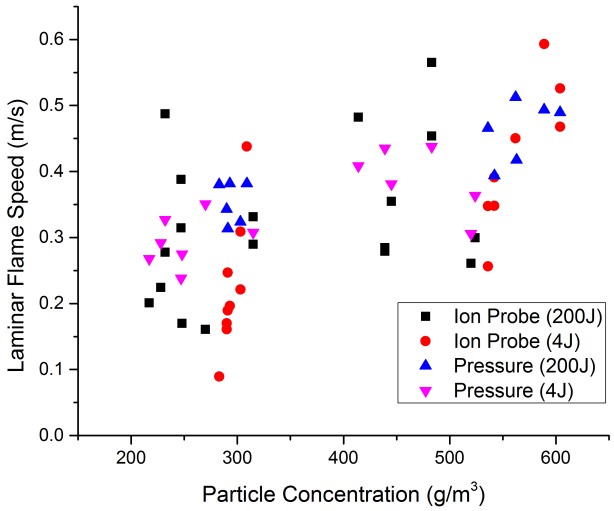

Figure 3.13: Measured flame speed with pressure and ionization probes for different ignition energies.

The laminar flame speed was then calculated from the pressure-time data using Equation 1.9. The ratio of the specific heats, γ, was taken to be 1.4 and the vessel radius, R, was calculated assuming a sphere with the same volume as the chamber used. The linear mass burnt fraction x(p) (Equation 1.10) was also used. A representative pressure-time curve and its first derivative from a fuel-rich sulfur flame are shown in Figure 3.14. The corresponding

calculated laminar flame speed is shown as a function of time in Figure 3.15.

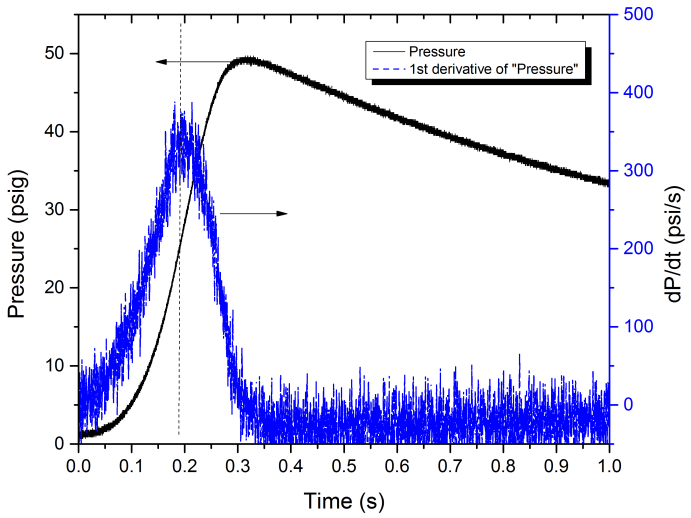

Figure 3.14: Sample pressure-time data from a sulfur explosion.

The calculated laminar flame speed initially oscillates significantly due to a low signal to noise ratio from the pressure transducer signal. These oscillations dampen as the pressure rises. Despite the oscillatory nature, each calculated curve was observed to oscillate around a constant value until the time where dP/dt is a maximum. The time of the maximum rate of pressure rise is indicated by the vertical lines in Figures 3.14 and 3.15. The laminar flame speed from the pressure data was taken as the average speed from 20 ms after ignition to the time where $(dP/dt)_{max}$ was reached. The time of 20 ms was used to limit the influence of the low signal-to-noise ratio of the pressure data very close to the instant of ignition. The decrease in laminar flame speed after $(dP/dt)_{max}$ was also observed by Santhanam et. al [21]. The reason for the decrease in flame speed is very likely due to heat losses. As the flame approaches the walls of the vessel, additional heat is lost to those walls which are near room temperature. The rate of pressure rise, which is related to the rate of heat release, decreases because some of that energy is absorbed by the chamber walls. The rate of pressure rise is proportional to flame speed (see Equation 1.9) so that a decrease in flame speed is observed.

The amount of energy lost to the chamber walls is difficult to quantify because of the complexity of the problem. However, the relative importance

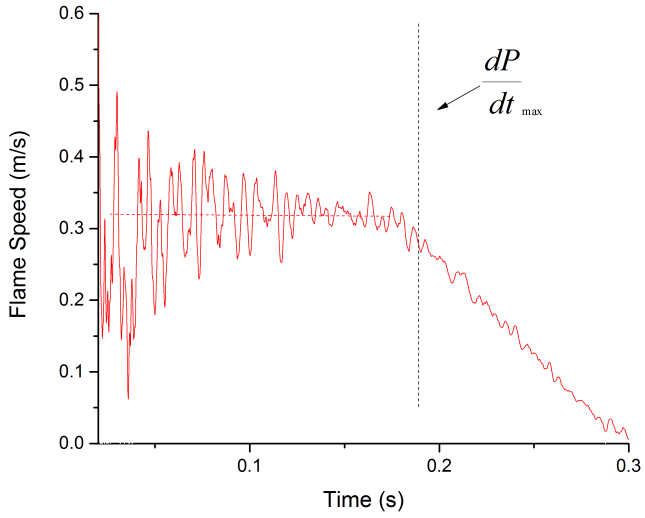

Figure 3.15: Calculate flame speed from pressure-time data.

of conduction versus radiative losses may be analyze qualitatively. The ratio of conductive to radiative losses, Equation 3.1, were approximated for different flame temperatures and location (i.e. distance between the flame and the wall) where k is the thermal conductivity, ϵ is the emissivity, σ is the Stefan-Boltzmann constant, Δx is the distance between the flame and the wall, and T is the temperature at the location indicated by its subscript. Since the emissivity of the powder is unknown, the ratio of the heat losses were calculated as a function of emissivity. Figure 3.16 shows the results from these calculations.

$$\frac{Q_{cond}}{Q_{rad}} \approx \frac{k}{\epsilon\sigma} \frac{(T_{flame} - T_{wall})}{\Delta x} \frac{1}{T_{flame}^4 - T_{wall}^4} \tag{3.1}$$

Radiative heat transfer is the dominant loss mechanism when the ratio is much less than unity (i.e. less than 0.1), while conduction is most important when the ratio is greater than 10. At the intermediate values (i.e. between 0.1 and 10), radiative and conductive losses are comparable. High temperatures and large values of the emissivity favor radiative dominanted heat losses, which is to be expected since thermal radiation is dependent on those two parameters. For most of the conditions in this calculation set, radiation is either dominant or comparable to conduction, as illustrated in Figure 3.16. This observation means it is unlikely that observed decrease in calculated

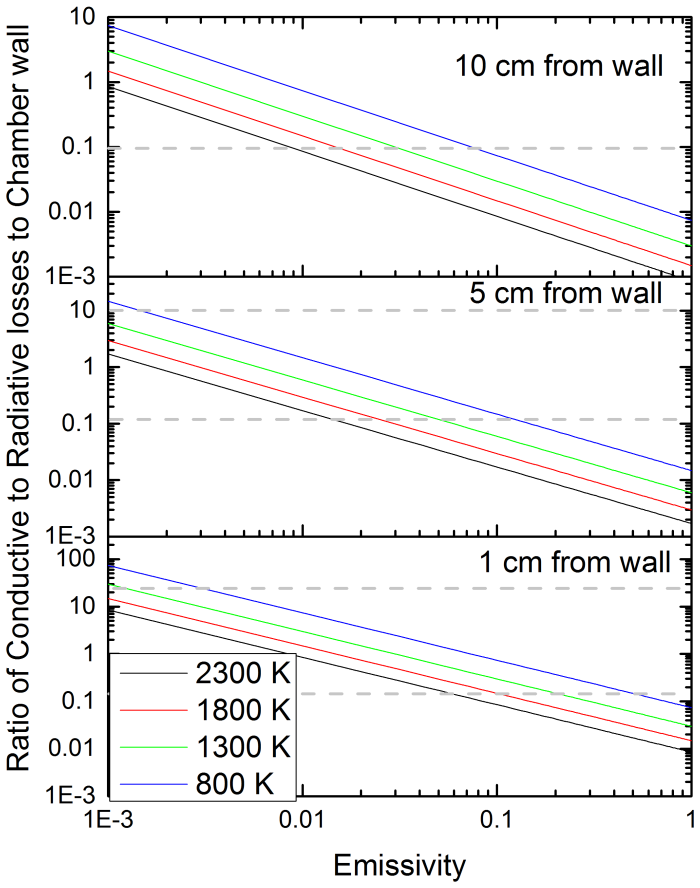

Figure 3.16: Calculated (first order approximation) ratio of the conductive and radiative heat losses at multiple positions and flame temperatures.

flame speed is due to conduction.

The calculation assumed a linear dependence on temperature along the distance between the flame and the chamber wall. It is more likely that the gradient used in the calculation is greater than in the experiment so that conductive losses are even less important (until the flame is very close to the wall). Moreover, effects from the optical depth and multple scattering by the unburnt particles were not considered in the calculation. The actual amount of thermal radiation reaching the wall will significantly increase as the flame approaches the walls due to the exponential nature of Beer's Law. From this reasoning, we believe that the increased amount of thermal radiation intercepted by the chamber wall as the flame grows is the cause for the decrease in the calculated flame speed.

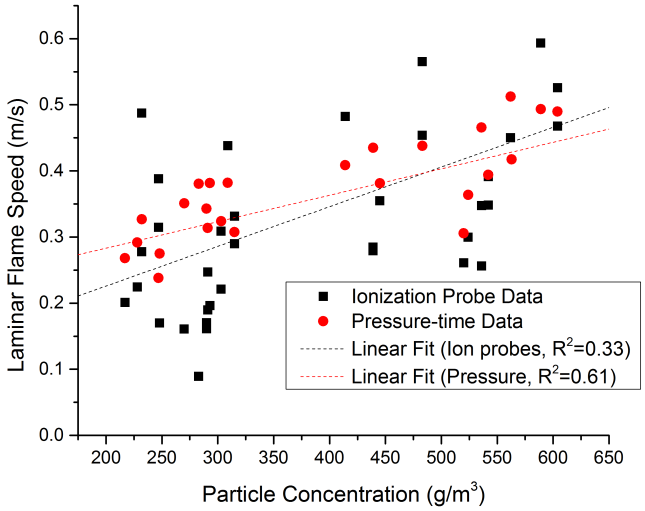

Figure 3.17: Comparison of the flame speed determined by the ionization probes and pressure-time data.

The calculated laminar flame speeds from the pressure data and the ionization probes are plotted in Figure 3.17. Reasonable agreement is seen between the two measurement techniques. The flame speed of 23 ± 6 cm/s reported by Proust [38] was approximately 20% lower than the stoichiometric flame speed measured in the current work. This result suggests that it is plausible to use pressure-time data to estimate laminar flame speed. The higher flame speeds measured here are likely due to increased turbulence here, although, it is difficult to prove without any doubt, because the level of turbulence was

not measured in either study.

However, as discussed above, the measurements from the ionization probes and shadowgraph indicate that the explosive event was still turbulent from the lack symmetry. As such, it is somewhat inappropriate to use this technique to determine the *laminar* flame speed. It better represents the flame speed of an equivalent spherical flame with the same mass consumption rate. With that being said, the pressure-time data does provide a measure of a flame speed based upon the degree of turbulence. This result should still allow comparisons of flames in different conditions to be compared as long as the degree of turbulence is kept constant (i.e. injection parameters, ignition delay and energy).

3.3 Sulfur Dust Combustion

To this point, this work has demonstrated how to effectively disperse sulfur dust, to determine the appropriate delay between the end of injection and ignition, and to show that pressure-time data may be used to measure flame speed. Using the results from these previous sections and additional measurements, the work discussed now will provide insight into the combustion process and mechanism of sulfur dust flames. Pressure rise, spectroscopic measurements, flame temperature, and flame speed (both as a function of oxygen and particle concentration) were made and will be discussed. Following the presentation of these measurements, a discussion of the analysis of this data will focus on determining the details of sulfur dust combustion.

Since the motivation of this work is the application of sulfur dust flames to counter biological warfare, it was decided to conduct the tests in air. Changing the the particle concentration and the oxygen content allowed for the effect of stoichiometry and heat release to be tested and thus provide insight into the fundamental mechanisms involved. The conditons tested here are only a small subset of what can be tested, but it is sufficient for the reasons just listed.

3.3.1 Pressure Data

One of the most fundamental measurements for constant volume explosions is the pressure rise. The last section showed the importance of pressure data and how it is related to flame propagation. The overall pressure rise within a constant volume chamber is a measure of the heat release. The maximum pressure rises are shown in Figure 3.18 with the theoretical maximum pressure rise in the adiabatic limit. It was observed that the pressure rise increased with particle concentration and increasing oxygen concentration and is consistent with work by Cashdollar et al. [70] after scaling their pressure data to account for the different chamber volumes between this work and that reported in Ref [70].

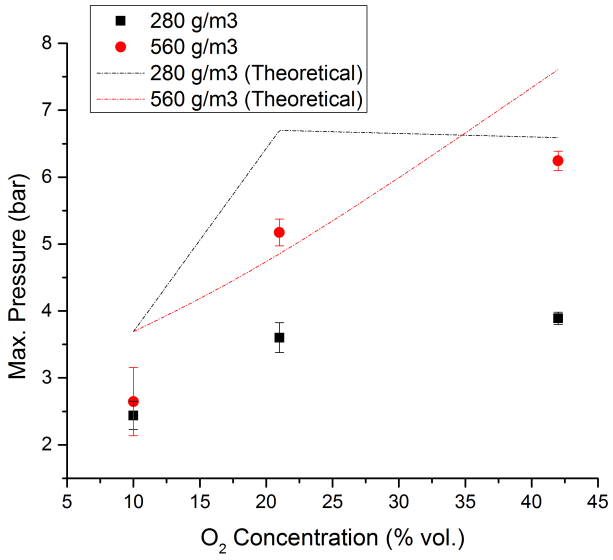

Figure 3.18: Maximum pressure rise (absolute pressure) for sulfur explosions within a 31 L chamber.

The increase in pressure rise (and thus heat release) was larger for experiments ranging between the 10% and 21% oxygen cases than the 21% and 42% oxygen tests. This result is expected for the lower particle concentration since the relative change in pressure by increasing the oxygen concentration calculated in the adiabatic limit has the same qualitative dependence on the oxygen content.

The 560 g/m^3 condition with 21% oxygen resulted in a pressure rise greater than the adiabatic pressure. This result may be due to particle settling from

increased agglomerations during the experiment. An increase in agglomerations at the higher particle loadings were reported in Section 3.1. If additional particles fall out of the suspension, it will bring the equivalence ratio closer to stoichiometric for these conditions. The adiabatic pressure will increase and approach the value seen for the lower particle loading. A similar effect of particle settling should then be expected for the 10% and 42% oxygen conditions. The difference in the adiabatic pressure rise for 10% O_2 is negligible because the maximum theoretical pressure rises are almost identical. The adiabatic maximum pressure in the oxygen enriched case will be lower because of the increased particle settling. For all of these conditions, it is challenging to quantify how much the pressure should change theoretically. The particles suspended in the bottom portion of the chamber will of course settle first. This region is out of the field-of-view for optical access and thus would not be noticed in the results from Section 3.1.

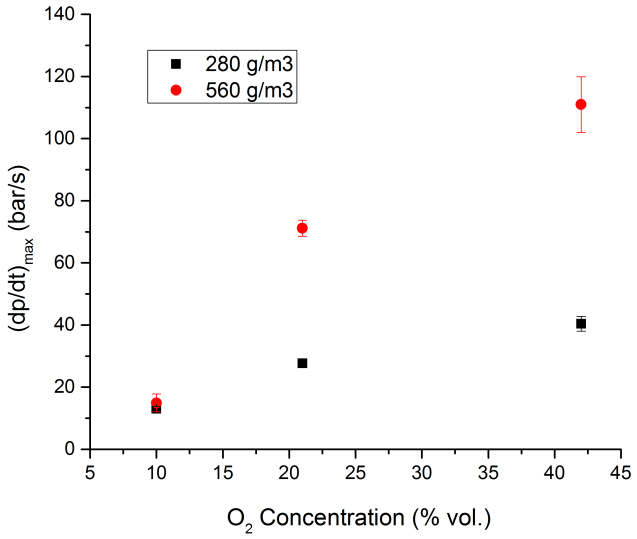

Figure 3.19: Maximum rate of pressure rise (absolute pressure) within the 31 L chamber from sulfur explosions.

The maximum rate of pressure rise was seen to increase monotonically with oxygen concentration. For oxygen concentrations above 10% by volume, the rate of pressure rise is greater for higher particle concentration. Figure 3.19 displays this information. The rate of pressure rise indicates how quickly the heat is being release. The importance of this quantity can be seen in Equation 1.9, where the rate of maximum pressure rise is directly proportional to the

flame speed.

3.3.2 Emission Spectroscopy

Spectroscopic measurements were used to provide qualitative and quantitative information (i.e. temperature). Two spectrometers were used: the Ocean Optics Jaz spectrometer and a custom 444 mm focal length Czerny-Turner spectrometer. It should be noted that emission (sufficient to be recorded) was only seen for the fuel-rich 21% oxygen test and the 42% oxygen tests (both particle concentrations). None of the other conditions provided enough signal.

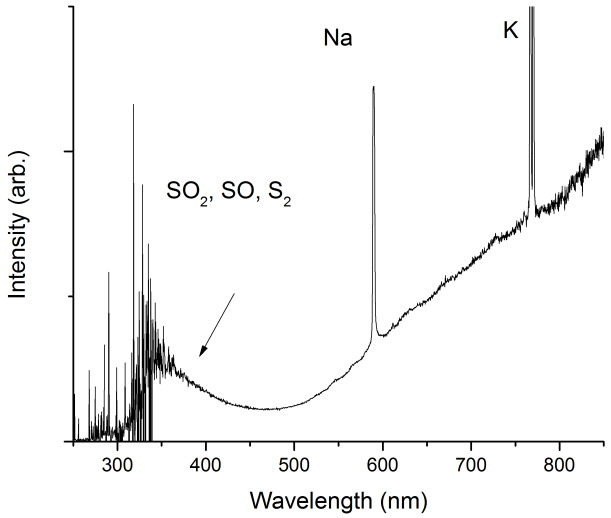

Figure 3.20: Emission spectrum taken with the Jaz spectrometer over the UV-Visible-IR region from a 21% oxygen, fuel-rich sulfur explosion.

The Ocean Optics spectrometer provided spectra over a wide spectral region. A sample spectrum is shown in Figure 3.20. In the UV portion of the spectrum, a broadband feature is observed in emission. This feature is likely the convolution of SO and SO_2 [71]. The B-X transition of S_2 begins to appear in this region as well [72, 73]. Above approximately 550 nm to 850 nm, a strong thermal background was observed. After removing the sodium and potassium atomic peaks, which arise from impurities in the powder, this background may be fit to a temperature by Planck's equation. The fitting details will be discussed in the following section on flame temperature.

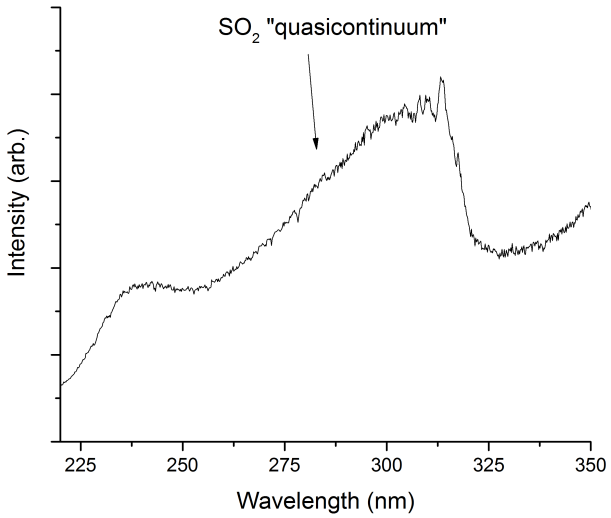

Figure 3.21: Moderate resolution (0.5 nm) emission spectrum of the UV features from a sulfur explosion. Spectrum was taken with the 444 mm focal length spectrometer and a 300 gr/mm grating.

The 444 mm spectrometer was used to provide higher resolution spectra of the broad feature seen in Figure 3.20 and extending further into the near infrared, beyond the range of the Jaz spectrometer. Figure 3.21 shows a higher resolution spectrum of the UV features. The quasicontinuum near 280-290 nm is very likely from SO_2. A portion of the SO B-X transition is located at wavelengths greater than 300nm. The B-X transition of S_2 also begins in this region and is then seen (see Figure 3.22) at higher wavelengths moving into the visible portion of the spectrum. Several of the strong bands in this transition are labeled [72, 74].

The emission from S_2 requires that the fuel was in the gas phase. This observation likely means that sulfur combustion has a gas-phase (i.e. homogeneous) component, confirming the result from Ref. [34]. Recall that the Glassman criterion dictates that if the boiling point of the oxide is lower than the fuel, it burns heterogeneously. However, this rule-of-thumb does not apply to sulfur. The low boiling point of sulfur (718 K) is much lower than other materials that follow the Glassman criterion (e.g. boron) [9].

It is impossible to quantify the concentration of sulfur in the gas-phase by only using emission spectroscopy. Therefore, even though this observation suggests that there is a gas-phase component, it is not clear if the reaction is

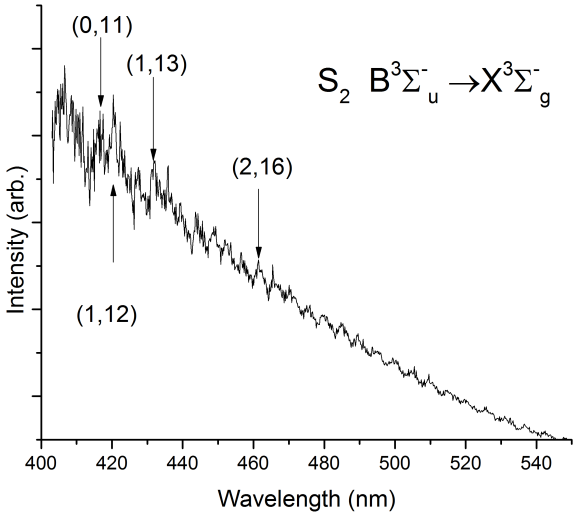

Figure 3.22: Emission features of the sulfur dimer in the blue part of the spectrum. Spectrum was taken with the 444 mm focal length spectrometer and a 300 gr/mm grating.

dominated by gas-phase chemistry. The previously discussed emission of the sulfur oxides does not necessarily indicate a strong gas phase component. The products of sulfur combustion, like carbon, are in the gas phase. Thermally populated excited states of the oxides could still result in emission.

The limited range of the Ocean Optics spectrometer required the 444 mm spectrometer to be used to investigate further into the near infrared. Figure 3.23 shows features at wavelengths near 1 micron. The electric dipole forbidden b-X transition of sulfur monoxide was observed near 950 nm. A higher resolution spectrum on the SO b-X transition shown in Figure 3.24. There is also a feature seen closer to 1 micron. This feature could not be indentified and does not appear to be from a known transition of a sulfur-containing molecule. Transitions of molecules containing silicon were also checked since the anti-caking agent was silicon dioxide. We were still unable to identify the transition. Since a long pass filter was used, it cannot be from any second (or third) order effects.

The ground state of the b-X transition ($^3\Sigma^-$) has a spin multiplicity of 3 and the excited electronic state is a singlet. Since a photon does not have a spin, this transition is forbidden by the electric dipole transition selection rules [42]. These so-called forbidden transitions can occur (with different

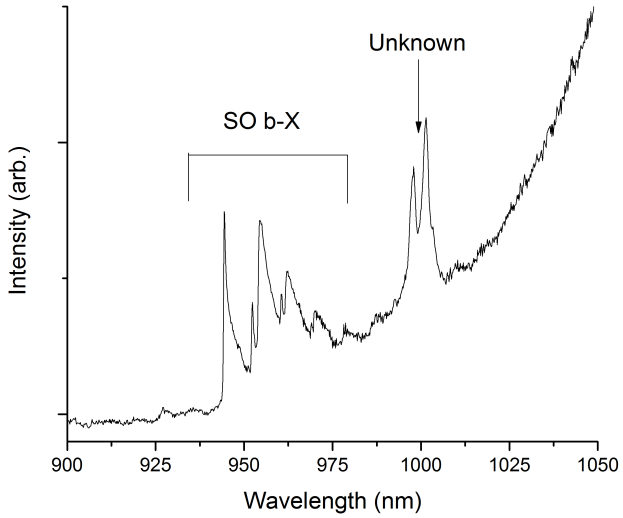

Figure 3.23: Emission spectrum in the near infrared. Spectrum was taken with the 444 mm focal length spectrometer and a 300 gr/mm grating.

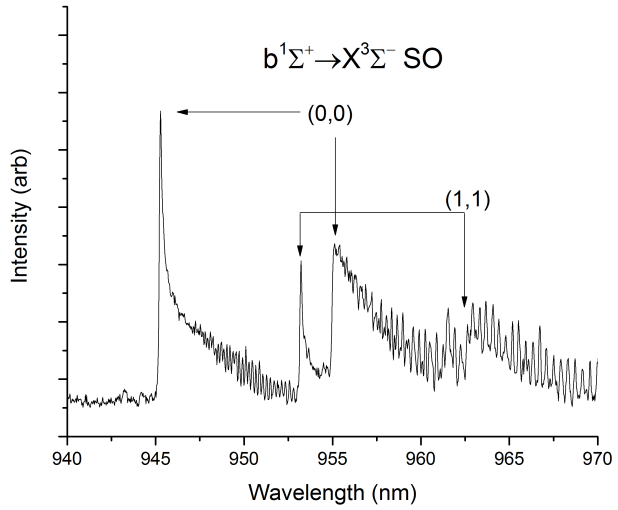

Figure 3.24: High resolution (0.15 nm) of the SO b-X transition. Spectrum was taken with the 444 mm focal length spectrometer and a 1200 gr/mm grating.

selection rules) but with a smaller probability. The transition is not specified as a magnetic dipole or electric quadrapole in the literature but we believe that it results from a magnetic dipole.

The spin multiplicity of 3 for the ground state requires the quantized electronic spin angular number, S, to be equal to unity. When $S \neq 0$, the spin angular momentum is no longer parallel with or coupled to the internuclear axis of the molecule, while the orbital angular momentum is parallel to the internuclear axis because it is zero for a Σ state [42]. Thus, the coupling rules follow Hund's case B [42]. Herzberg [42] also explains that the rotation of the molecule produces a small magnetic moment in the direction of the resultant vector, $\overrightarrow{K}$, of the nuclear and orbital angular momenta. This magnetic moment couples $\overrightarrow{K}$ and $\overrightarrow{S}$ (i.e. the spin angular momentum vector) [42]. The significance of this coupling is explained with Schlapp's work [75]. The change in symmetry (+ to −) of the wavefunctions for the electronic states involved in the SO b-X transition are forbidden by the selection rules of magnetic dipoles. However, Schlapp [75] shows that a molecule in an intercombination (i.e. non-zero change in spin) transition can occur because of spin-orbit coupling. This scenario exists with the SO b-X transition. The spin-orbit coupling (which is caused by a magnetic moment) in the $^3\Sigma^-$ state is likely the reason why the SO b-X transition occurs. Since a magnetic moment is formed, it is probable that the transition is of the magnetic dipole variety. An oxygen band, $^1\Sigma_g^+ \rightarrow^3 \Sigma_g^-$, is due to a similar transition and is a known magnetic dipole, suggesting that the previous analysis is correct [76].

3.3.3 Absorption Spectroscopy

Absorption spectroscopy probes the ground state of a molecule or atom. This fact can allow temperature measurements to be made from species despite whether the emission is due to a thermally populated distribution or from a nonequilibrium process.

Absorption measurements were attempted by collimating the light from a xenon flash lamp and passing it through the chamber. This measurement was applied to the SO b-X transition and some of the other features seen in the visible and ultraviolet. The scattering of the incident light from the particles resulted in over 95% of the incident light being attenuated through

the chamber in the UV to the blue part of the visible regions of the spectrum. The amount of light that was actually transmitted resulted only in approximately 100 counts on the detector. Furthermore, the augmentation of the spectral distribution of the light from the particle scattering (neglecting gas absorption) is unknown. These reasons made the absorption experiments observations of little value.

Absorption was also attemped in the near infrared for the forbidden b-X transition of SO. More light was transmitted (about an order of magnitude), which is likely due to the longer wavelengths and the smaller extinction cross-sections of the particles at those longer wavelengths [59]. Despite the increase in transmitted light, no absorption was observed. As much as 1000 counts were recorded on the detector. The shot noise is approximately $\pm 3\%$ at that level. Forbidden transitions are much less likely to occur [42] so the fraction absorbed over the 355 mm path length is small. It is possible that absorption did occur but was not above the noise level.

3.3.4 Spectroscopic Model

It was decided to determine the rotational temperature of the experimental SO b-X spectrum. First, a model needed to be created to simulate the spectrum. The free software PGOPHER was used [43]. This program takes the spectroscopic constants (input by the user) and calculates the line by line intensities for each rotational transition (from the first 500 rotational levels) within the (0,0) and (1,1) vibrational bands. It then convolves each line with a line shape to simulate the spectrum. A Voigt profile was used with a full-width-half-maximum of 0.15 nm (the same as the experimental spectrum in Figure 3.24). Spectroscopic constants were taken from the work of Colin [77] for the excited state and from Herzberg [42] for the ground state. The values for the ground and excited electronic states are shown in Table 3.1 where T_e is the energy of the electronic state, ω_e is the angular vibrational frequency, $\omega_e x_e$ is the first order anharmonic constant, α is the rotational distortion constant, γ is the spin-rotational coupling constant, B_e is the rotational energy, r_e is the equilibrium internuclear distance, D_e and β are constants describing the centrifugal distortion.

The spectroscopic constants in Table 3.1 were used in Equations 3.2, 3.3,

Table 3.1: **Spectroscopic Constants for the SO b-X model.**

State	$X^3\Sigma^-$	$b^1\Sigma^+$
T_e, cm^{-1}	0	10509.97
ω_e, cm^{-1}	1149.2	1067.66
$\omega_e x_e, cm^{-1}$	5.6	7.8
α, cm^{-1}	0.005736	0.0063
γ, cm^{-1}	-0.00572	0
B_e, cm^{-1}	0.7208171	0.7062
D_e, cm^{-1}	1.134e-6	1.2e-6
β, cm^{-1}	0	0.1e-6
$r_e, \mathring{A}$	1.4811	1.5001

and 3.4 to find the band origin, rotational constant, and cetrifugal distortion constant for each vibrational state, respectively. Higher order anharmonic effects were ignored because the spectroscopic constants were not available in the literature. The values for each of the vibration state were calculated and entered into PGOPHER.

$$E = T_e + \omega_e(v + 1/2) - \omega_e x_e(v + 1/2)^2 \tag{3.2}$$

$$B = B_e - \alpha(v + 1/2) + \gamma(v + 1/2)^2 \tag{3.3}$$

$$D = D_e - \beta(v + 1/2) \tag{3.4}$$

The program internally calculates Höln-London factors [43] (i.e. transition strength for rotational lines). The Franck-Condon factors had to be calculated externally. There were no experimentally measured Franck-Condon factors for each of these vibratonal transitions so they were calculated theoretically. Specifically, because of the way PGOPHER was written, the square root of the overlap of the vibrational wavefunctions (i.e. Franck-Condon factors) was required. The integral of the product of the vibrational wavefunctions for each transition was calculated numerically using Simpson's rule for numerical integration [78]. A sample calculation is shown and explained in further detail in Appendix C. The square root of the Franck-Condon factors for the (0,0) and (1,1) transitions were 0.9685 and 0.9065, respectively. These values may seem to be closer to unity than expected for a forbidden electric

dipole transition. However, the equilibirum internuclear distances are 1.48 and 1.50 $\mathring{A}$ for the ground and excited state, respectively. Because the values are close in magnitude, a large amount of overlap in the wavefunctions is reasonable. The small probability for a specific transition to occur is a product of the Franck-Condon factor, rotational line strengths (i.e. Höln-London factors in this case), and oscillator strength [42, 41]. Only the oscillator strength is required to be much less than unity for a forbidden transition, so it may be possible to have Franck-Condon factors of the magnitude reported above.

All of the discussed values were entered into a PGOPHER file. Simulated spectra were produced at different temperatures and with the same Voigt full-width-half-maximum (i.e. resolution) as the experimentally measured spectra. Two spectra, each at a different temperature, are illustrated in Figure 3.25.

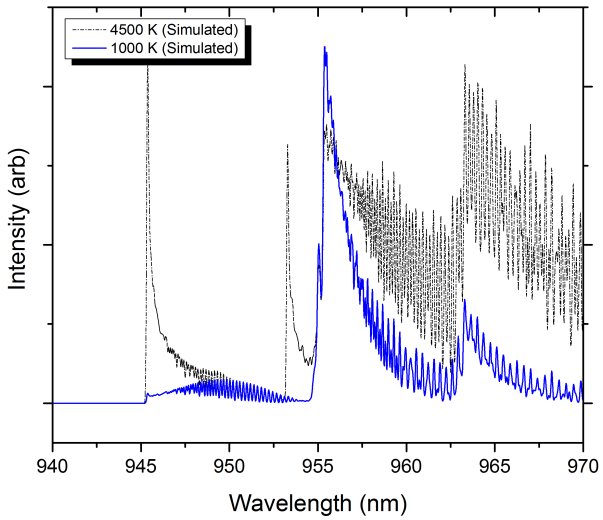

Figure 3.25: Simulated spectrum at 1000 K and 4500 K as produced from PGOPHER.

3.3.5 Model and Experiment Comparison

The higher resolution spectrum, Figure 3.23, was compared to the simulated spectrum from PGOPHER. The multiple bandheads for each vibrational band are likely due to the spin multiplicity of the ground state. To verify

this hypothesis, the simulation was run with a fictitious singlet ground state. The PGOPHER file contains an entry field for the spin quantum number (i.e. spin multiplicity). For the simulation described above, that field for the ground state spin value was set to $S = 1$ (i.e. a triplet). The fictitious singlet ground state was created by only changing S from unity to zero. The band heads (one for each vibrational transition) located at 945 and 953 nm no longer appeared in the simulated spectrum. Thus, it is likely that these band heads arise from the ground state multiplicity. To our knowledge, the observation of those bandheads has not been reported in the literature.

Without rigorously fitting the experimental spectrum to the calculated spectrum, it was determined that this transition was indeed from a nonequilibrium process. The ratio of the heights of the two band heads for the (0,0) transition (at 945 and 955 nm) from the experimental spectrum do not approach that of the simulated spectrum until temperatures greater than 4500 K. In other words, the intensity of the band head at 945 nm was observed to be greater than the intensity of the band head at 955 nm in the experimentally measured spectrum. The simulation does not show those same relative heights until temperatures greater than 4500 K. This temperature is greater than the adiabatic flame temperature (which is an equilibrium thermodynamic quantity), thus it is likely not in rotational equilibrium. A similar analysis of the (1,1) band heads provided evidence for the same conclusion.

The emission is believed to be due to chemiluminescense. The source for the populated excited $^1\Sigma^+$ state is likely to due to the following set of reactions listed as Equations 3.5 and 3.6 [79]:

$$O_2(^1\Delta_g) + SO(^1\Delta_g) \rightarrow O_2 + SO(^1\Sigma_g^+) \tag{3.5}$$

$$SO(^1\Delta_g) + SO(^1\Delta_g) \rightarrow SO + SO(^1\Sigma_g^+) \tag{3.6}$$

The latter equation (Equation 3.6) is favored energetically (i.e. less endothermic) over Equation 3.6 [79]. Since during combustion SO and O_2 have comparable concentrations (through equilibrium calculations), it is possible that Equation 3.6 is the favored path.

3.3.6 Flame Temperature

As mentioned above, the temperature was measured through traditional means (i.e. via thermocouple) and optics. The previous discussion demonstrated that an equilibrium temperature was unable to be obtained from the SO b-X transition. Absorption measurements were also unsuccessful because of the combination of high optical depth and the weakly absorbing (and possible low concentration of SO molecules in the $^1\Sigma^+$ state) SO b-X transition. This transition was the only observed spectral feature that could be used for a temperature measurement because it was sufficiently free of interferences from other spectral features. The convolution of the molecular emission in the UV would present an extremely difficult, if not impossible, task of obtaining an accurate temperature measurement. The addition of a small quantity of another powder into the mixture could be used as a tracer to assist in measuring the temperature spectroscopically. The tracer material would be chosen and used to produce a species that emits and/or absorbs in a spectral region that was previously absent of molecular and atomic spectral features. Without those measurements, the temperature of the sulfur flames were only measured by thermocouple and pyrometry.

Both measurements were used to determine the peak temperature. The thermocouple provided the peak temperature locally while pyrometry measurements indicated the peak temperature within the field of view of the pyrometer. The spatially integrated pyrometry signal are always biased towards the hottest regions due to the strong temperature dependence on the intensity of thermal radiation. Pyrometry data was collected with the 3-color PMT pyrometer and the Jaz Ocean Optics spectrometer. It should be noted that only the 825 nm and 905 nm signals were used because the 700 nm channel did not provide sufficient signal level. The integration time for all data collected by the spectrometer was 10 ms.

Representative traces of the time-resolved data provided by the PMT pyrometer are displayed in Figure 3.26 with the calculated temperature using the gray body approximation as shown in Figure 3.27. The early peak seen in Figure 3.27 was due to the emission from the pyrotechnic igniter. It was observed that the maximum temperature from the sulfur explosion occurred near the time that the rate of pressure rise was maximum. The peak temperature was recorded for each experiment.

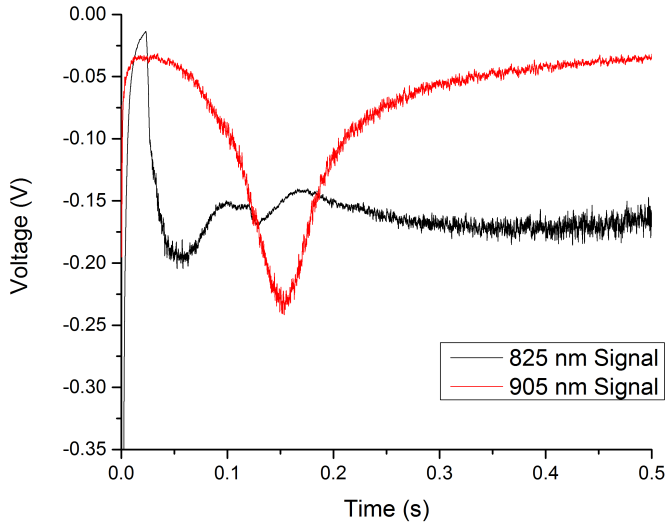

Figure 3.26: Representative filtered signals for the PMT pyrometer. Only the 825 nm and 905 nm signal are shown.

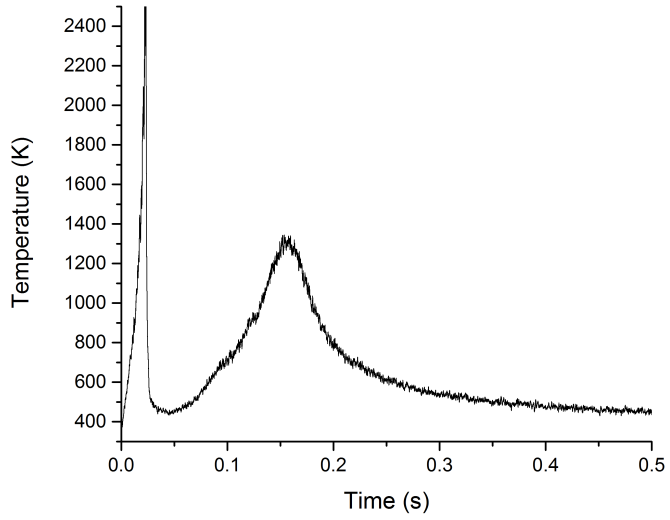

Figure 3.27: Calculated temperature profile from the data in Figure 3.26. The initial peak is from the igniter.

Figure 3.28 shows a spectrum taken from the Jaz spectrometer. Each subplot is representative of a separate assumption for the spectral emissivity. It is seen that the gray body approximation provides the highest temperature and is thus an upper limit on the flame temperature. The gray body assumption was used throughout the data analysis. The absence of high temperature emissivity data prevents the use of a more accurate assumption. Furthermore, recent work on the optical depth effects on the spectral emissivity have demonstrated that the functional wavelength dependence can decrease significantly at high optical depths [47]. These high optical depths were observed in Section 3.1. The use of a gray body is still not necessarily completely justified because the work in Ref. [47] used a specific set of refractive indices in the model. However, the optical properties of the powder were not known at the elevated temperatures so the appropriate spectral emissivity was also unknown. A gray body was believed to be the most appropriate assumption for the spectral emissivity because of the optical depth.

The elevated temperatures measured were a result of the temperature rise from both the heat release and the compression of the gases as the pressure rose. The measured peak temperatures from pyrometry and the thermocouples are shown in Figure 3.29. Only thermocouple data was obtain from the 10% oxygen tests, because the pyrometry signals were very weak and much lower than the noise level. The PMT pyrometer was used only for the 21% because of a spectral interference near 900 nm when the oxygen level was increased to 42% by volume. One possible source of this interference, as displayed in Figure 3.30, is the emission of molecular oxygen [80]. The thermal background from the Jaz spectrometer was fit for each of the tests for the oxygen enriched conditions. As such, no time-resolved data was obtained for these conditions.

The dashed lines represent the adiabatic flame temperatures calculated. The temperature was adjusted by considering the heat absorbed by the anticaking agent. This change in temperature was minimal (typically less than 10 K). It should be noted that this adjustment is a first order approximation since it did not include the equilibrium composition to be recalculated at the final temperature.

It was observed that the peak temperature steadily increased for the lower particle concentration from approximately 800 K to about 1300 K for the thermocouple measurements (corrected for radiative losses) as the oxygen

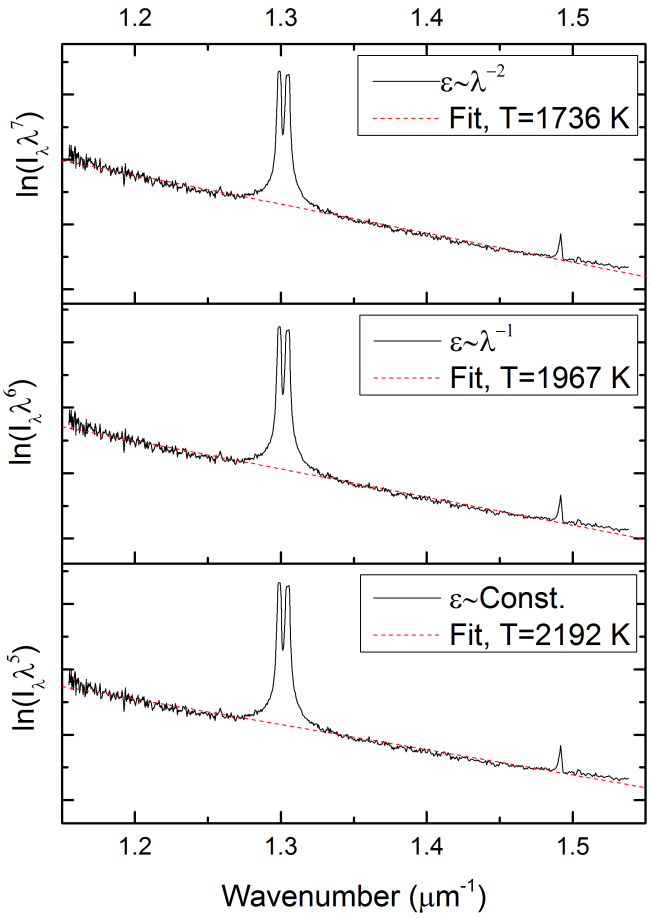

Figure 3.28: Fits of the thermal background from the Jaz spectrometer to determine temperature.

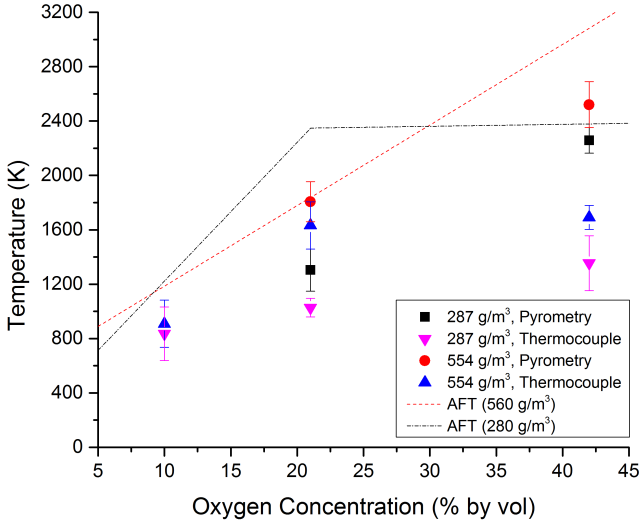

Figure 3.29: Temperature measurements of sulfur dust explosions.

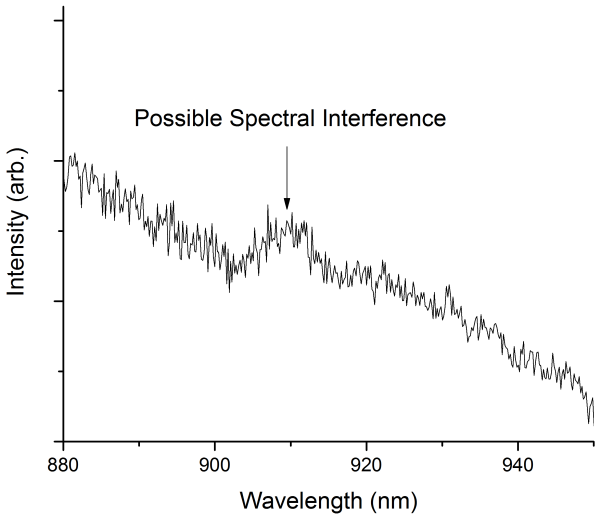

Figure 3.30: Emission spectrum showing the possible molecular interference near 900 nm for experiments with 42% oxygen.

content was increased from 10% to 42%. The increase in temperature from 21% to 42% oxygen from the pyrometry measurements was much greater as the maximum temperature exceeded 2000 K. This large difference is likely due to the fact that pyrometry measurements are biased towards the highest temperatures within the field-of-view while the thermocouples measured the local temperature.

A large temperature difference between the pyrometry and thermocouple measurements was also seen for the 21% and 42% oxygen tests at the higher particle loading. The temperature was observed to increase with particle loading for all oxygen concentrations. The average peak temperature for the 10% oxygen case was the lowest of the conditions for the 560 g/m^3 tests at 909 K.

The increase in temperature as oxygen concentration increased was likely due to the amount of energy liberated in each condition. The pressure data indicated that the maximum pressure rise (i.e. heat release), Figure 3.18, increased with oxygen concentation.

Since the pressure rise increased the temperature through compression, it is useful to compare the measured temperatures with the effect of gas compression taken into account. It was assumed that the compression was isentropic until the point in time where the rate of maximum pressure rise was observed. This assumption is valid because of the results discussed in Section 3.2. The PMT pyrometer provided time-resolved temperature data, so that the instantaneous pressure data could be used to adjust the temperature as a function of time. The pyrometry data from the Jaz spectrometer and thermocouple data did not provide the same time-resolved data. As such, peak temperatures were adjusted to account for the pressure rise at at $(dp/dt)_{max}$ where peak temperatures were observed to occur from the time-resolved data. The adjusted temperature data are shown in Figure 3.31.

The observed temperature increase with oxygen concentration is still valid. The maximum change in temperature resulting from this calculation was approximately 36% which was from the 42% oxygen, 560 g/m^3 case. The temperature in 21% oxygen rose to 842 and 1270 K for the thermocouple measurements of 280 and 560 g/m^3, respectively, as compared to the lower oxygen concentration, which were close to 800 K. Pyrometry data displayed slightly higher temperatures for both cases. Using a gray body assumption for emissivity, the measured mean peak temperatures were 1010 and 1370

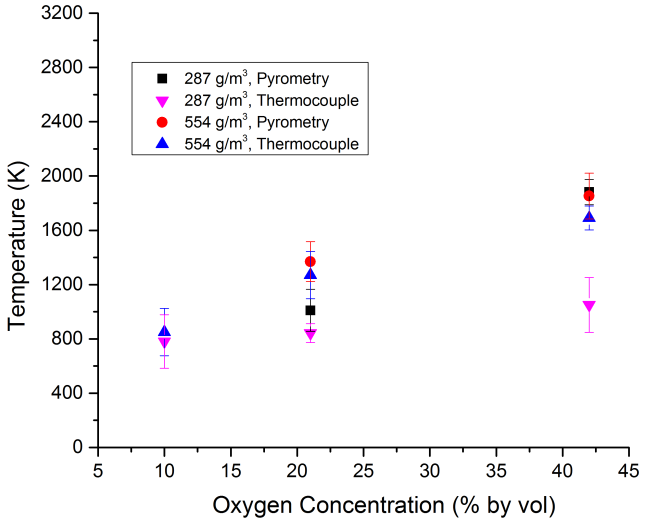

Figure 3.31: Measured peak temperatures adjusted for isentropic compression.

K with 21% oxygen for the 280 and 560 g/m^3, respectively. The measured temperatures increased further for the 42% oxygen cases. The thermocouple temperature increased to 1692 K for the 560 g/m^3 tests and to approximately 1050 K for the 280 g/m^3 experiments. The mean peak temperature with 42% oxygen measured by pyrometry was 1881 and 1853 K for 280 and 560 g/m^3, respectively.

3.3.7 Flame Speed

Since the pressure-time data was determined to be an accurate way of measuring flame speed within the constant volume explosion chamber, it was decided to use that diagnostic to determine how particle and oxygen concentrations affected the flame speed. The same approach that was used to determine flame speed, as discussed above, was applied to the other conditions. The data for all of the particle and oxygen concentrations are summarized in Figure 3.32.

The individual data points for the 21% oxygen case were displayed in the previous section (see Figure 3.17). The averages at that oxygen concentration also includes additional data points taken after the completion of that portion of the work. A monotonic increase in flame speed was observed with the

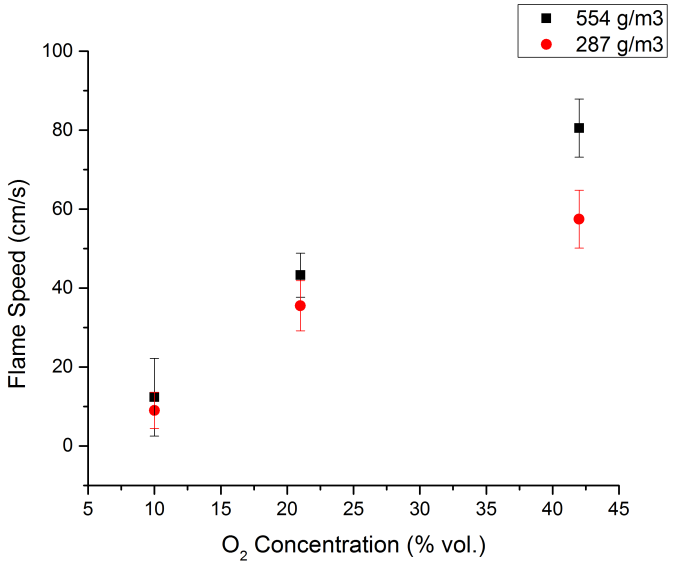

Figure 3.32: Flame speed measurements by analysis of pressure-time data for sulfur dust explosions.

increase in oxygen concentration. A similar trend was shown in Figure 3.19 for the $(dp/dt)_{max}$ data. Since the flame speed was calculated from the pressure data (and S_L scales with dP/dt), it is expected to see a similar dependence. This result shows that the rate of maximum pressure rise may be used to determine how flame speed scales between different conditions. For a given oxygen concentration, the higher particle loading condition (i.e. higher equivalence ratio) has a greater flame speed.

Our results are very different than what is typically observed for gaseous flames. Gas flames typically have a flame speed that peaks near stoichiometry and decreases as the equivalence ratio deviates further from that condition [10]. This difference is what distinguishes dust flames from other combustion phenomena. Dust flames have characteristics of both premixed and diffusion flames, as explained in the opening chapter. The propagation of premixed gaseous flames is based upon the gas phase transport of heat and mass. Dust flames, which are premixed on a macroscopic level, operate on the same mechanisms but the difference is the length scale that gas and dust flames are each considered premixed. Because dust flames are composed of small diffusion flames (i.e. from each particle), the spacing of those diffusion flames is a crucial aspect for flame propagation. Larger particle loading means that the interparticle distance is smaller and thus, quantities like heat

are transported over shorter distances to reach the next particle.

3.4 Combustion Mechanism Discussion

Combining information that each different measurement provides, one can make key conclusions for the fundamental mechanisms of sulfur dust combustion. These are:

1. Maximum pressure rise data showed that more heat was released as the oxygen content was increased. For a given oxygen concentration, the pressure rise increased with powder concentration.

2. Gas-phase emission from sulfur oxides and S_2 suggests that sulfur has a gas-phase component, but the extent of the gas-phase chemistry is unknown.

3. The flame speed increased monotonically with oxygen concentration. A slight increase was observed with particle concentration for a given oxygen concentration.

4. The peak flame temperature was seen to increase significantly from the 10% oxygen case to the 21% oxygen for the higher particle loading. Less increase in temperature was seen for that powder loadings as the oxygen content increased to 42%. The lower particle loading saw a steady, albeit, smaller increase in temperature

As listed above, the data suggest that sulfur burns in the gas phase. However, the data do not suggest anything about the limiting process(es) during combustion. Multiphase combustion processes can occur in two limiting regimes: diffusion and kinetic limited [9]. Therefore, it is necessary to conduct analysis that will provide insight into that aspect of the mechanism.

3.4.1 Damköhler Number Analysis

Calculation of the key Damköhler number will aid in this discussion. As discussed in the introduction, this Damköhler number is the ratio of the chemical and diffusion time scales. A chemical time scale was determined

by simulating an adiabatic, constant volume, PSR with the SOx mechanism from University of Leeds [35]. The ratios of sulfur (in the form of S_2), oxygen, and nitrogen that were present in the chamber after injection were used as the initial conditions. This calculation is only limited to the gas-phase with atomic and dimer sulfur being the only allotropes included. The initial pressure was 1 atmosphere and the initial temperature was set to 1300 K. The elevated temperature was needed to initiate the reaction. The time step was set to 1 microsecond. The chemical time scale was taken as the time it takes for the temperature to go from 10% to 90% of the total temperature change. The temperature change was the difference from 1300 K to the adiabatic flame temperature. A summary of the chemical time scales are shown in Table 3.2.

Table 3.2: **Summary of the Chemical Time Scales.**

	$10\%O_2$	$21\%O_2$	$42\%O_2$
$280g/m^3$	329 μs	18 μs	14 μs
$560g/m^3$	219 μs	58 μs	4 μs

The diffusion time scale is inversely proportional to the diffusion coefficient, D, which was calculated from kinetic theory [12]. The expression for the binary diffusion coefficient is listed as Equation 1.5 and taken from Laurendeau [12]. The binary diffusion coefficient of oxygen through nitrogen was first calculated. The temperature was taken to be the measured flame temperature from pyrometry that was not adjusted to take into account the temperature rise from compression. This value was the temperature that was experienced by the gases near the particles. The pressure was taken as 1 atm. The reasoning for this assumption was that at the time when the flame front passed the thermocouples and ionization probes, the pressure within the chamber had not significantly risen.

Since the units of the diffusion coefficient are $[\frac{m^2}{s}]$, an appropriate area was needed to determine the time scale. The cross-sectional area of the sulfur particle (using the Sauter mean diameter of 30.4 μm) was used. The precise area is not particularly of concern since this analysis is based upon the order of magnitude and scaling of the Damköhler number. The resulting diffusion time scales and the Damköhler numbers are listed in Tables 3.3 and 3.4.

The use of area does raise one concern, which is the dependence of Da with

diameter. Equation 1.4 showed that the dependence is d^1. If the analysis is conducted with the same particle sizes, this effect should be minimal. The change in pressure during the experiment may also affect Da. If we only consider the relative change in Da between each condition, this effect should also be minimized since the pressure rise will at most only change by a factor of approximately two. The maximmum pressure rise for 21% O_2 is only approximately twenty percent lower than the 42% oxygen concentrations (for each particle concentration). Therefore, the analysis with the Damköhler numbers will be limited to a relative comparison of Da between two conditions as opposed to using the exact value of Da to determine which regime the flame burns.

Table 3.3: **Summary of the Diffusion Time Scales.**

	$10\%O_2$	$21\%O_2$	$42\%O_2$
$280g/m^3$	99.0 μs	44.7 μs	16.7 μs
$560g/m^3$	87.6 μs	28.5 μs	14.1 μs

Table 3.4: **Summary of the Damköhler Numbers.**

	$10\%O_2$	$21\%O_2$	$42\%O_2$
$280g/m^3$	0.3	2.5	1.2
$560g/m^3$	0.4	0.5	3.5

A significant increase (i.e. by an order of magnitude) in Da is seen as the oxygen concentration increased from 10% to 21% for the lower particle concentration. A similar increase is observed for the 560 g/m^3 concentration as the oxygen content rises from 21% to 42%. This increase suggests that as the oxygen concentration increases, diffusion becomes more important which is counterintuitive. The reasoning is that oxygen was not the only quantity that changed. The temperature also increased and that affects the chemistry more significantly than diffusion (i.e. exponentially versus $T^{1.65}$). The exponent on temperature (1.65) includes the temperature dependence from the collision integral [81]. The more intriguing aspect of this observation is that for both of the particle loadings, diffusion becomes more important as the flame transitions from fuel-rich conditions to stoichiometric. Stoichiometry for the 280 g/m^3 and 560 g/m^3 concentrations is when there is 21% and 42% oxygen by volume, respectively.

The chemical time scale for the 280 g/m^3 condition drops by about 2 orders of magnitude over the same change in oxygen concentration. As the oxygen content was further increased, only a minimal change was seen. The lack of a further reduction in chemical time scale suggests that the chemistry is approaching its maximum reaction rate for that condition (i.e. amount of sulfur). As far as stoichiometry is concerned, it is believed then that a further increase in oxygen (to 84%) for the 560 g/m^3 loading will lack the same change in chemical time scale. In fact, after running the PSR code, the chemical time scale for the further increase in oxygen (resulting in the same equivalence ratio as the 42%, 280 g/m^3) was 2.4 μs agreeing with the previous hypothesis.

The second component of the Damköhler number is the diffusion time scale which, as mentioned above, is inversely proportional to the diffusion coefficient. The diffusion coefficient scales as $T^{1.65}$ and $MW^{-0.5}$. Because of this scaling, even if the temperature were to increase by 1700 K (bringing the temperature up to about 3100 K, the adiabatic flame temperature, for the hottest measured condition), the diffusion time scale would only decrease by about a factor of about 2.8. Similarly, if the diffusion of two other species besides O_2 and N_2 were considered (i.e. SO, SO_2, S_2), the diffusion time scale would change by less than a factor of 2 (increase or decrease). Therefore, the diffusion coefficient will not change significantly (i.e. an order of magnitude) for mixtures of sulfur compounds, oxygen, and nitrogen.

3.4.2 Flame Speed Scaling Analysis

The above discussion only provided insight into how the flames in each condition burned relative to one another. Analysis of the flame speed and temperature can be used to further specify the combustion mechanism. It was observed that the temperature and the flame speed for the 10% oxygen cases were considerably lower than the other conditions. The lower temperature would more likely have a greater affect on the kinetics than diffusion. The diffusion coefficient scales as $T^{1.65}$, however, the reaction rate is related to temperature Arrheniusly (i.e. exponentially). Thus, the lower temperature flame will be nearer to the kinetical limit than diffusion limited). The Damköhler number was in fact observed to be lowest for that condition.

That analysis still does not explain why the temperature was lower. Recall the maximum pressure rise was lowest for both particle concentrations for that (i.e. 10%) oxygen concentration. This observation means that the least amount of energy release went into heating the gases within the chamber when compared to other conditions. The 10% oxygen case was fuel-rich for both particle loadings which means that oxygen was the limiting reactant. The excess sulfur particles act only as heat sinks and do not contribute to the heat release. In other words, the contents of the chamber (both gas and particles) contain approximately the same heat capacity as the other oxygen conditions but with less heat release for each respective particle concentration. The lower heat release means that the overall temperature will be lower.

As the oxygen content increased, so did the overall heat release, since more powder was being burned. The larger heat release created a higher temperature environment, which in turn increased the reaction rate. The faster reaction rate can be explained in Figure 3.19 as the increase in the rate of pressure rise and in Figure 3.32 with the flame speed data.

The scaling of the flame speed should be dependent on the burning mechanism. Landau and Lifshitz [18] state that the flame speed for a thermally driven combustion wave scales as $(\alpha/\tau_{comb})^{0.5}$, where τ_{comb} is a combustion time scale. Goroshin et al. [16] argued that for a diffusion limited flame, τ_{comb} scales inversely proportional to the diffusion coefficient of the gas. If the flame is diffusion limited, the flame speed should scale as $(\alpha D)^{0.5}$. Goroshin et al. [16] contended that if this thermally driven flame is kinetically limited, the difference in mass diffusivity of the gas mixtures (i.e. in each condition) should not play a role, thus the flame speed should scale with $(\alpha)^{0.5}$. This logic was used for the current work. The theoretical scaling for the diffusion and kinetically limited flames are shown in Tables 3.5 and 3.6, respectively. The velocity ratios from the data of the current work is displayed in Table 3.7.

Table 3.5: **Flame Speed Scaling in the Diffusion Limit.**

	$\frac{V_{10\%}}{V_{21\%}}$	$\frac{V_{21\%}}{V_{21\%}}$	$\frac{V_{42\%}}{V_{21\%}}$
$280 g/m^3$	0.64	1.00	1.73
$560 g/m^3$	0.52	1.00	1.43

Table 3.6: **Flame Speed Scaling in the Kinetic Limit.**

	$\frac{V_{10\%}}{V_{21\%}}$	$\frac{V_{21\%}}{V_{21\%}}$	$\frac{V_{42\%}}{V_{21\%}}$
$280g/m^3$	0.89	1.00	1.15
$560g/m^3$	0.85	1.00	1.09

Table 3.7: **Measured Flame Speed Ratios**

	$\frac{V_{10\%}}{V_{21\%}}$	$\frac{V_{21\%}}{V_{21\%}}$	$\frac{V_{42\%}}{V_{21\%}}$
$280g/m^3$	0.25	1.00	1.62
$560g/m^3$	0.29	1.00	1.86

It is observed that the ratio of experimentally measured velocities from the 21% and 42% oxygen cases (for both particle concentrations) are much closer to the ratio predicted by the diffusion limited theory. This result, in conjuction with the previous discussion, suggests that oxygen enriched sulfur dust flames burn in the diffusion limit.

Intuitively, it would be expected that an oxygen enriched flame would burn in the kinetic limit since a higher concentration of oxygen is closer to the particle surface and potentially significantly reducing the diffusion time scale. However, the oxygen concentration is only one aspect of these flames. The temperature measurements show that the flame burns hotter as more oxygen was added to the system. The diffusion time scale does decrease with temperature ($T^{1.65}$), but it is not affected as much as the kinetics, which scale exponentially with temperature. The increase in temperature causes the chemistry to occur much faster, resulting in the diffusion process to be the limiting step.

Decreasing the oxygen concentration to 10% does not fit the scaling ratios predicted by kinetically or diffusion limited flame. The experiments with higher oxygen concentrations produced very consistent data whereas the 10% oxygen concentrations had a larger spread. The larger spread is not well represented by the data shown here. On multiple occasions, the 10% oxygen tests did not ignite (for both powder concentrations). It is possible that perhaps a flammability unit was approached by these oxygen depleted conditons.

3.4.3 Sub-atmospheric Sulfur Flames

It was decided to test an addition experimental condition that would confirm that this approach for the analysis is correct. The 21% oxygen, 560 g/m^3 condition was run but with an initial pressure of 1/3 atm (after powder injection). The lower pressure should push the burning mechanism towards the kinetic limit. The same analysis conducted and discussed above was repeated for ths new condition.

The average flame speed (for the new condition) was measured to be 82.8 $\pm$ 7.0 cm/s with a temperature of 896 K. The velocity ratios, theoretical and experimental, are displayed in Table 3.8. The ratios are relative to the 21% oxygen, 560 g/m^3 condition under atmospheric pressure. The experimental ratio is between the ratio calculated based upon diffusion and kinetically limited flames. This result suggests that the flame is transitioning towards the kinetic limit, but has not reached that limit. Given that the test conditions were chosen to move toward this type of transition was expected, these calculations support the general trends suggested by the analytical approach.

Table 3.8: **Low Pressure Test Flame Speed Ratios Relative to** 21% **Oxygen at 1 bar**

Measured	Diffusion Limited	Kinetically Limited
1.91	2.72	1.47

3.5 Closing Remarks

In the opening chapter multiphase combustion was introduced by first discussing a fuel droplet burning. It is necessary to explain how dust explosions, while similar, can be much different. These differences have been mentioned throughout.

In summary, the droplet problem, from which the d^2 and d^1 scaling laws arise, specifies several ideal assumptions that are not applicable in dust flames. First, it assumes that the gas is quiescent [11]. This condition is not met due to the turbulence within the system from the injection process. Analysis of the droplet problem including convective losses results in a modified diffusion limit. For low Reynolds numbers, the diameter depen-

dence changes from d^2 to $d^{1.5}$ and the exponent will decrease further for large Reynolds numbers [9]. It terms of particle size scaling, the difference between the diffusion limit and kinetic limit will diminish. Due to the complexity of the problem, it is challenging to determine how this will alter the dependence on quantities like molecular weight, pressure, etc. The convective heat tranfer coefficient, which is needed to calculate convective heat transfer, is determined by correlations of the Nusselt number (for example, see Equation 2.4) [60]. Many of these correlations are complex equations, some of which are empirical. Because of this fact, it is difficult to determine the exact scaling of quantities, e.g. temperature.

Finally one must determine if the dust particles burn independently of each other. So a second condition that must be determined is the droplet spacing. The droplet combustion analysis assumes that there are no interactions with other particles [11]. The spray combustion community uses a group combustion number to estimate if the particles burn individually or together within a larger group flame. A group combustion number is defined by Glassman [9] as follows:

$$G = 3(1 + 0.276Re^{0.5}Sc^{0.5}LeN^{\frac{2}{3}})\frac{R}{S} \tag{3.7}$$

where Sc is the Schmidt number (ratio of momentum and mass diffusivities), Le is the Lewis number (ratio of thermal and mass diffusivities), N is the number of particles, R is the particle radius, and S is the average particle spacing [9]. The ratio of R and S is equal to the cube root of the quotient of the particle mass loading density (i.e. g/m^3) and the particle density [19] and is on the order of 0.1 for the conditions tested in this work. The number of particles within the chamber for a given test is off the order of $10^8 - 10^9$. Both Sc and Le will be on the order of 0.1 to 1. The Reynolds number is unknown because the velocity was not measured but it is likely orders of magnitude larger than $10^{-8} - 10^{-9}$. Therefore, using Equation 3.7, G will be much greater than 10^{-2}. A group number of less than 10^{-2} is specified for individually burning particles to occur [9].

It is clear that the physical conditions present in dust explosions are not the same as the environment considered in the droplet problem nor is a dust flame exactly like a premixed gas flame for that matter. The point of this short discussion is to emphasize that the complexities involved within this

phenomena are not be *completely* described by the ideals in either extreme. So, to apply concepts solely from the problem of an individually burning droplet, is inappropriate.

CHAPTER 4

CONCLUSIONS AND RECOMMENDATIONS

Sulfur dust explosions were investigated experimentally using a constant volume combustion chamber. A 31 L dust cloud combustion chamber was designed and built specifically for this work. The chamber design focused on the ability to make optical measurements for dust flames and high explosive testing.

4.1 Powder Dispersion

In addition to establishing a 31 L combustion/blast chamber, this work has demonstrated a methodology to determine the effectiveness of powder dispersion. The use of a two-dimensional laser extinction technique provided insight into the powder dispersion process. A statistical analysis used the mean and standard deviation of particle concentration from those measurements to determine:

1. The most appropriate time to ignite the cloud based upon the mean concentration approaching the expected value and a high degree of uniformity as indicated by the standard deviation.

2. The performance of anti-caking agents in their ability to help disperse easily agglomerating powders, such as sulfur.

It is recommended that using many lines-of-sight can provide valuable information on the uniformity of particle clouds. As shown earlier, the use of a single line-of-sight measurement may not be statistically accurate for the mean concentration. Moreover, it does not provide any information on the uniformity of the suspension.

The determination of the ignition time delay is based upon the experimental setup used here with the specific injection conditions (i.e. back pressure,

duration). Therefore, it may not necessarily be appropriate to use this timing for other setups. It is encouraged that the technique and analysis discussed in this work should be applied when sufficient optical access is available.

Future research is needed to understand how the ignition source affects the particle concentration. The blast wave created by pyrotechnic and spark igniters can disrupt the uniformity. It is important to understand to what degree this blast wave affects the particle concentration locally. If there is a substantial increase in local concentration from the blast wave, it may lead to an artificial increase in flame speed or pressure rise data.

4.2 Pressure-Time Validity

Ionization probes were used to measure the local flame speed within the chamber. Although the data contained a high degree of scatter, it was concluded that there was sufficient agreement with the flame speeds calculated from the pressure data. The scatter present in the ionization probe data was concluded to be cause by the turbulence within the chamber. The flame front was not observed to be spherical, which also contributed to the scatter in the data. It was determined that it is not appropriate to call the calculated flame speed laminar because of these reasons. This measurement can be used to estimate flame speed within dust flames, specifically for comparison purposes if the turbulence level is constant. The maximum rate of pressure rise was also seen to scale similarly to flame speed. This quantity may also be used to determine how flame speed will scale under different particle loadings.

These experiments were conducted with sulfur powder only. Burning sulfur produces a gaseous product so that it is not completely similar to metal dust flames which have condensed products. It is reasonable to question the validity of these results for metal fuels that are important in the energetics community. This concern is believed to be minimal because the rate of pressure rise is mostly determined by the heat release. The presence of an initially solid fuel volatilizing may increase the amount of moles in the gas phase, increasing the pressure. The stoichiometry of sulfur combustion results in the same number of moles of gas after the event as there were intially. Fuels with condensed phase products remove oxygen from the gas phase when the solid oxide is formed. The effect of this difference may result

in a slight change in the calculated flame speed.

The geometry of the combustion chamber used may also affect the resulting flame speed. The presence of a spherical wall may potentially change the manner in which the flame propagates because of different flow patterns. Although the flames observed within the cube chamber were not perfectly spherical or symmetric, it did not appear that this issue played a strong role. The shadowgraph measurement showed a circular-like flame front over the distances where the ionization probes were places. The Nevertheless, it is recommeneded that future research study the effects of geometry to quantify any potential difference.

4.3 Sulfur Dust Combustion

The mechanisms involved in sulfur dust combustion were studied through emission spectroscopy, measuring pressure data, flame speed, and flame temperature. Spectroscopic measurements indicated the presense of S_2 in the gas-phase. This result suggested that sulfur dust burns at least partially in the gas-phase, contrary to what was predicted by the Glassman criterion. It was determined that diffusion becomes significantly more important as the oxygen concentration increases. The scaling analysis between the 21% and 42% oxygen cases concluded that the flames were diffusion limited. Ten percent oxygen by volume was believed to approach the minimum oxygen concentration needed for a sulfur explosion to occur. Sub-atmospheric pressure flames displayed evidence of the mechanism moving towards the kinetic regime.

The conditions tested here are a subset of the possible conditions. It is recommended that the future research with sulfur dust combustion investigates other gaseous environments. Decreasing the pressure will further shift the mechanism towards the kinetic limit. Initial pressures above atmospheric conditions will likely continue to be diffusion limited. Changing the diluent from nitrogen could also potentially alter the combustion mechanism. The use of a inert, monatomic gases (i.e. helium, argon) will increase the flame temperature because of their smaller heat capacity. The higher temperatures will increase the reaction rate. However, diffusion will become faster due to the higher temperatures and lower molecular weight in the case of helium.

These conditions will likely increase the flame speed. Additional experiments will provide insight into how the combination of these effects will alter the combustion mechanism.

Research is also needed to understand combustion of individual sulfur particles. Specifically burn time measurements for particles under different ambient pressures, temperatures, and particle sizes can provide valuable information on the combustion mechanism for an isolated particle.

The work here did not consider the effects of particle diameter. All of the work, as described in previous chapters, used -325 mesh (i.e. particles less than 44 μm in diameter). Creating narrower particle size distribution for the quantity of powder needed to create the dust flames was not practical. However, controlling the particle size would provide additional scientific data. The smaller particles, when isolated and suspended in a stagnant gas, will theoretically burn towards the kinetic limit.

The mix of condensed and gas phases within each experiment adds to the complexity. Because sulfur melts and boils at temperatures much lower than other solid fuels, it may be possible to investigate sulfur flames purely in the gas phase. This type of experiment would contribute to the understanding of a pure sulfur-air flame without the need to consider effects from particles or turbulence present in the experiment.

The ability to isolate all of these effects would be unique for a solid dust fuel. This type of work could potentially be used to better understand dust flames and how the differ analytically from gaseous fuels as well as the combustion of individual particles. As discussed at the end of the previous chapter, there is a need to develop a theory specific to dust flames. The physical properties of sulfur make this fuel the ideal candidate to understand and develop the necessary theory to achieve a deeper understanding of dust flames.

APPENDIX A

STANDARD OPERATING PROCEDURE

The standard operating procedure used is listed below.

for i=1:graduation

1. Chamber Prep
    (a) Prior to starting any preparation, be sure that the fireset is shunted and the key is out.
    (b) Vacuum and/or wipe down chamber walls, windows, and igniter posts.
    (c) Clean copper ignition wire holders with ethanol and steel wool to insure good electrical contact.
    (d) Place igniter into alligator clips on the igniter posts
    (e) Place window insets in front of each window to protect them from the flame. Use a small piece of aluminum tape to hold in place.
    (f) Fill powder holder with desired powder and amount. Coat o-ring with vacuum grease and place it within the gland.
    (g) Use two 1/4-20 screws to fasten powder holder to the rest of the injector assembly. Note the tick marks on each piece for proper alignment.
    (h) Take out, clean, and grease the door o-ring. Be sure to clean the gland as well. Reinsert the o-ring.
    (i) Close the door and tighten bolts. Be sure the o-ring is entirely within the gland.
    (j) Vacuum down the chamber.

(k) Once the chamber is at vacuum, fill the chamber with the desired gas mixture and pressure.

(l) Close ALL valves including those leading to the vacuum and pressure gages to prevent damage.

(m) Check that all diagnostics and electronics (including solenoid valve and pulse generator) are ready.

(n) Open tank for the gas used for powder injection and be sure it is attached to solenoid valve at 100 psi(or desired pressure).

(o) Double check everything and the test is ready to be run.

2. Ignition Circuit

(a) Start with the fireset off and shunted

(b) Set desired delays for the solenoid valve and ignition on the pulse generator.

(c) Insert and turn fireset key to the ON position

(d) Charge the fireset to 4000V by holding down the ARM button.

(e) Continue to hold ARM button until AFTER ignition.

(f) Press EXC or Run (depending on device used) on the pulse generator to run test.

3. Post-experiment

(a) Congratulations on making it to this point (assuming you still have all of your limbs).

(b) Shunt and turn off fireset. Be sure to remove the key.

(c) Vent the contents of the chamber through appropriate system (i.e. bubbler, dust collector etc.).

(d) Save all data.

(e) Flush the chamber with air (or other gas) as needed

(f) Vent chamber to room exhaust so no pressure or vacuum exists within the chamber.

(g) Remove bolts from the door. Have a shop vac ready to prevent aerosolized dust from escaping.

(h) Once all airborn dust is vacuumed, continue to clean up chamber. Collect residue if wanted. Be sure to measure the amount of powder remaining in the powder holder for accurate concentration measurement.

end for loop

APPENDIX B

CHAMBER DRAWINGS

The following pages contain the technical drawings and a computer rendering of the 31 L dust cloud combustion facility.

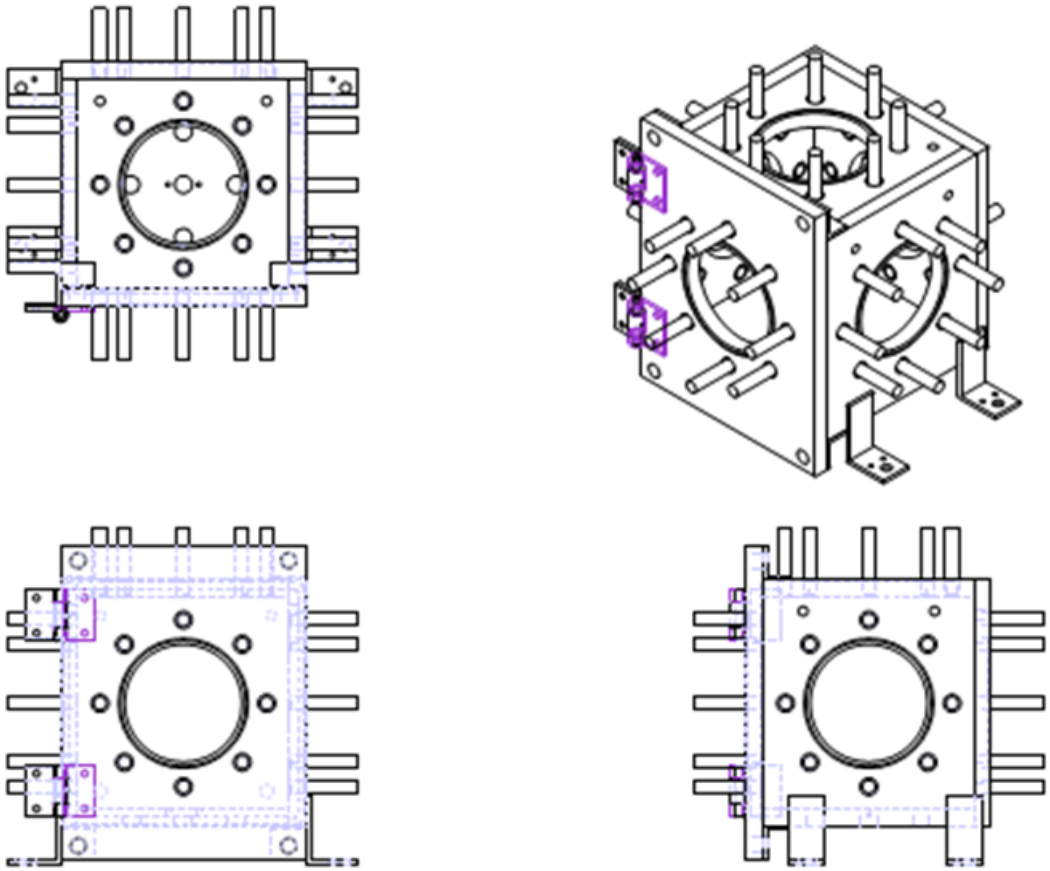

Note: This is sheet is just for illustration purposes.

Joe Kalman, UIUC MechSE

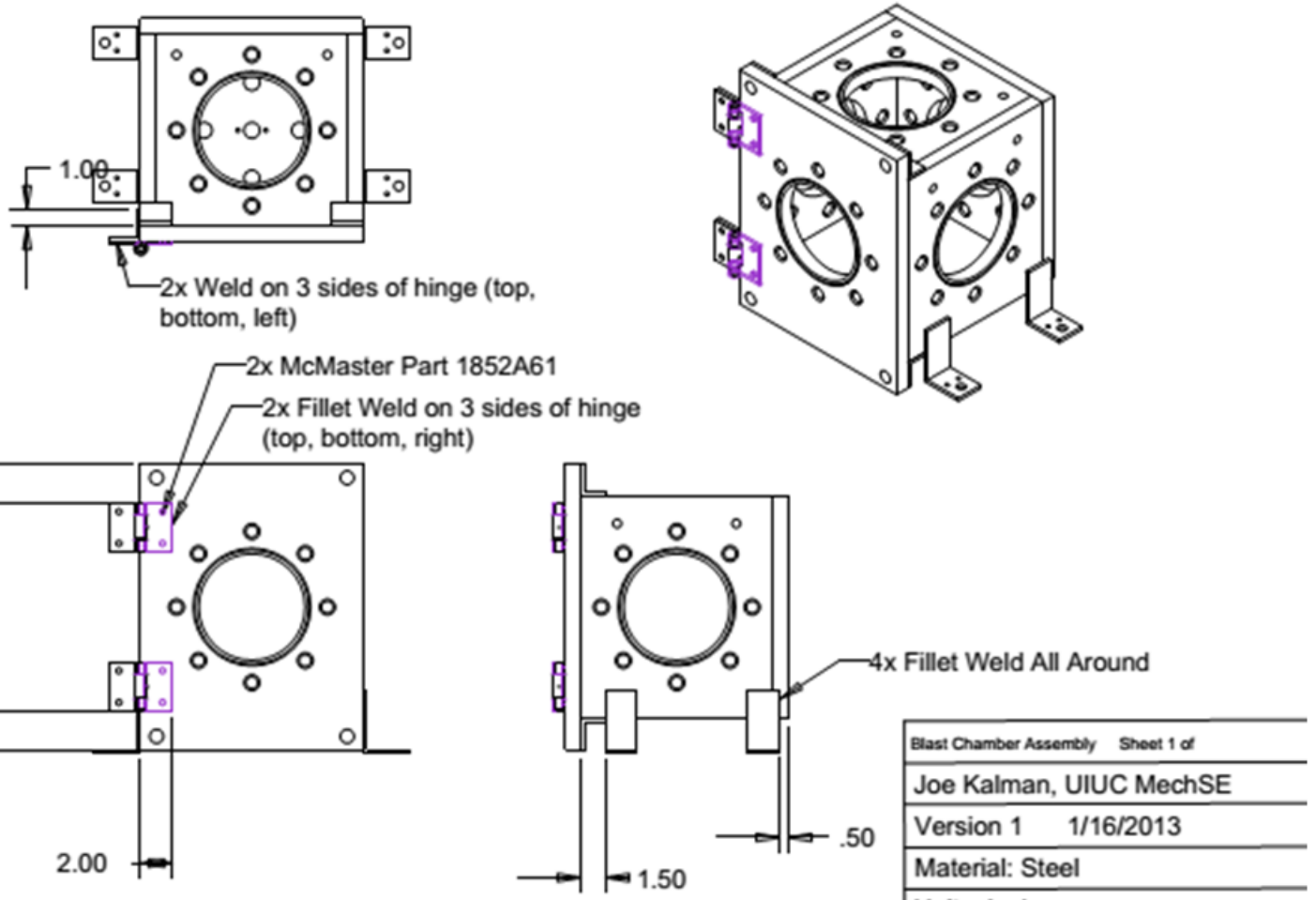

Blast Chamber Assembly	Sheet 1 of
Joe Kalman, UIUC MechSE	
Version 1	1/16/2013
Material: Steel	
Units: Inches	
Scale: 0.125	

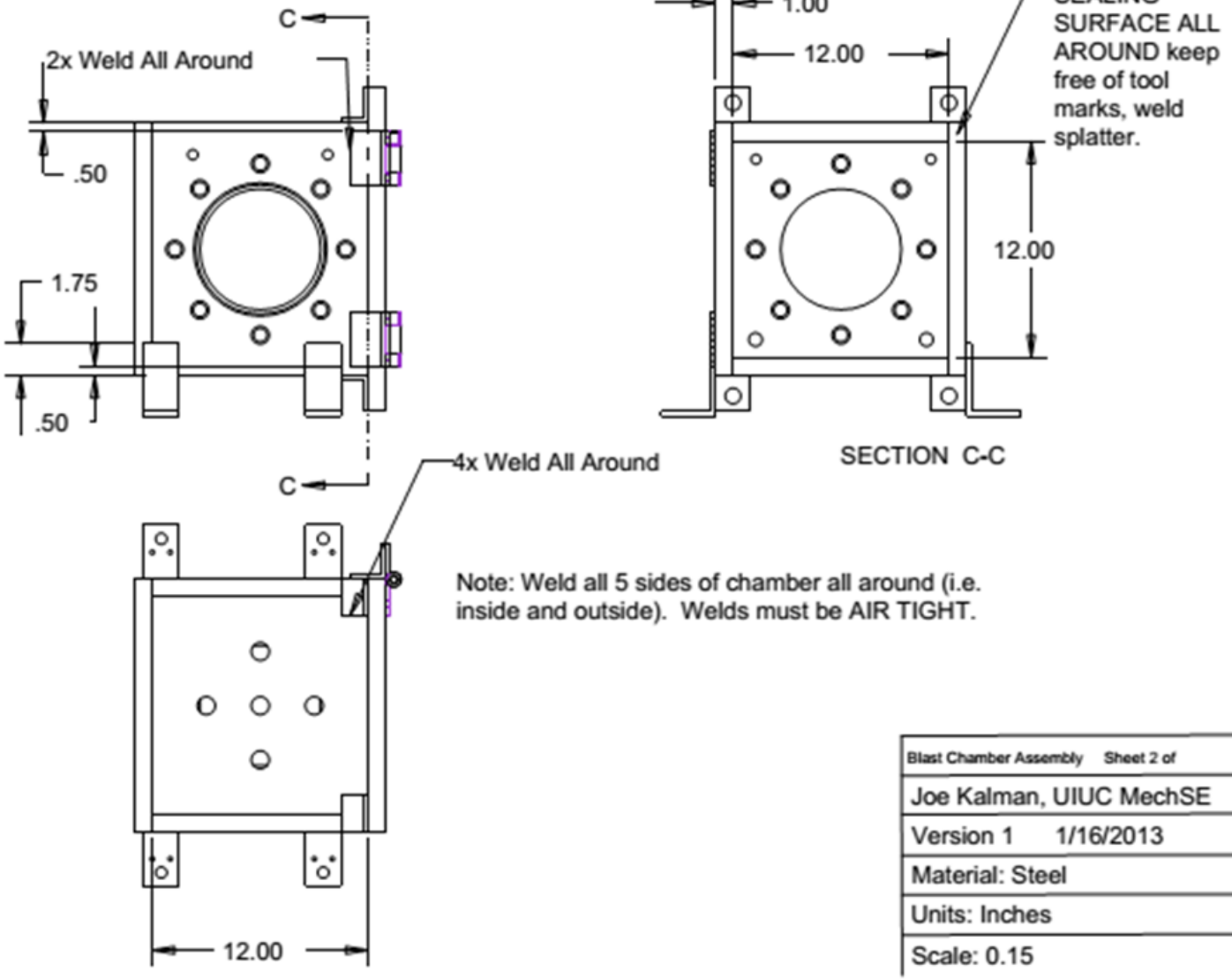

Note: Weld all 5 sides of chamber all around (i.e. inside and outside). Welds must be AIR TIGHT.

Blast Chamber Assembly Sheet 2 of
Joe Kalman, UIUC MechSE
Version 1 1/16/2013
Material: Steel
Units: Inches
Scale: 0.15

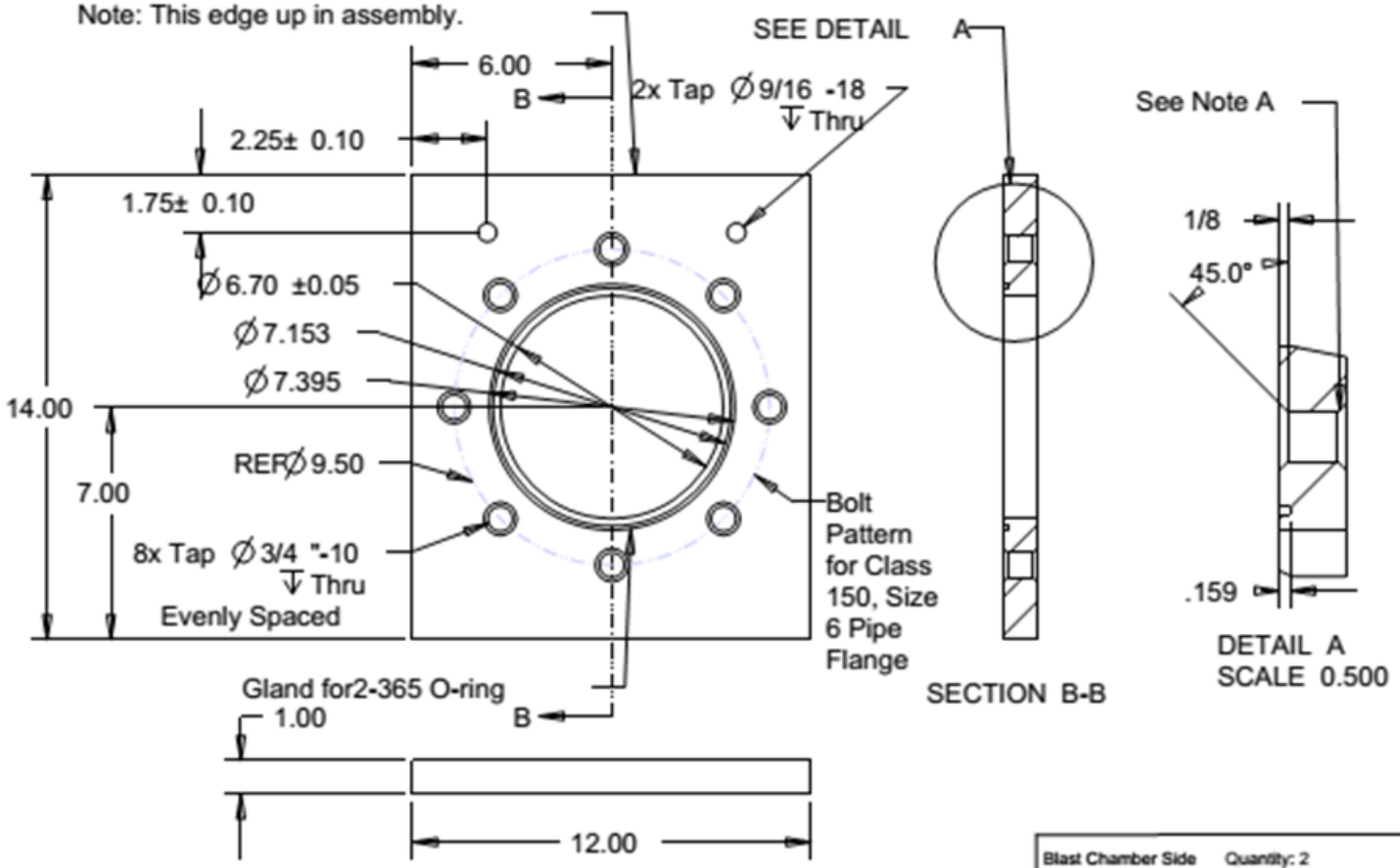

Note A: Countersinks dimensions are suggestive. 3/4"-10 threaded rod is threaded into the tapped holes and welded on both sides. The countersinks shown are filled with weld material. Welds are ground smooth on both sides. Threads closest to surface will not be used.

Blast Chamber Side Quantity: 2
Joe Kalman, UIUC MechSE
Version 1 1/16/2013
Material: Steel
Units: Inches
Scale: 0.25

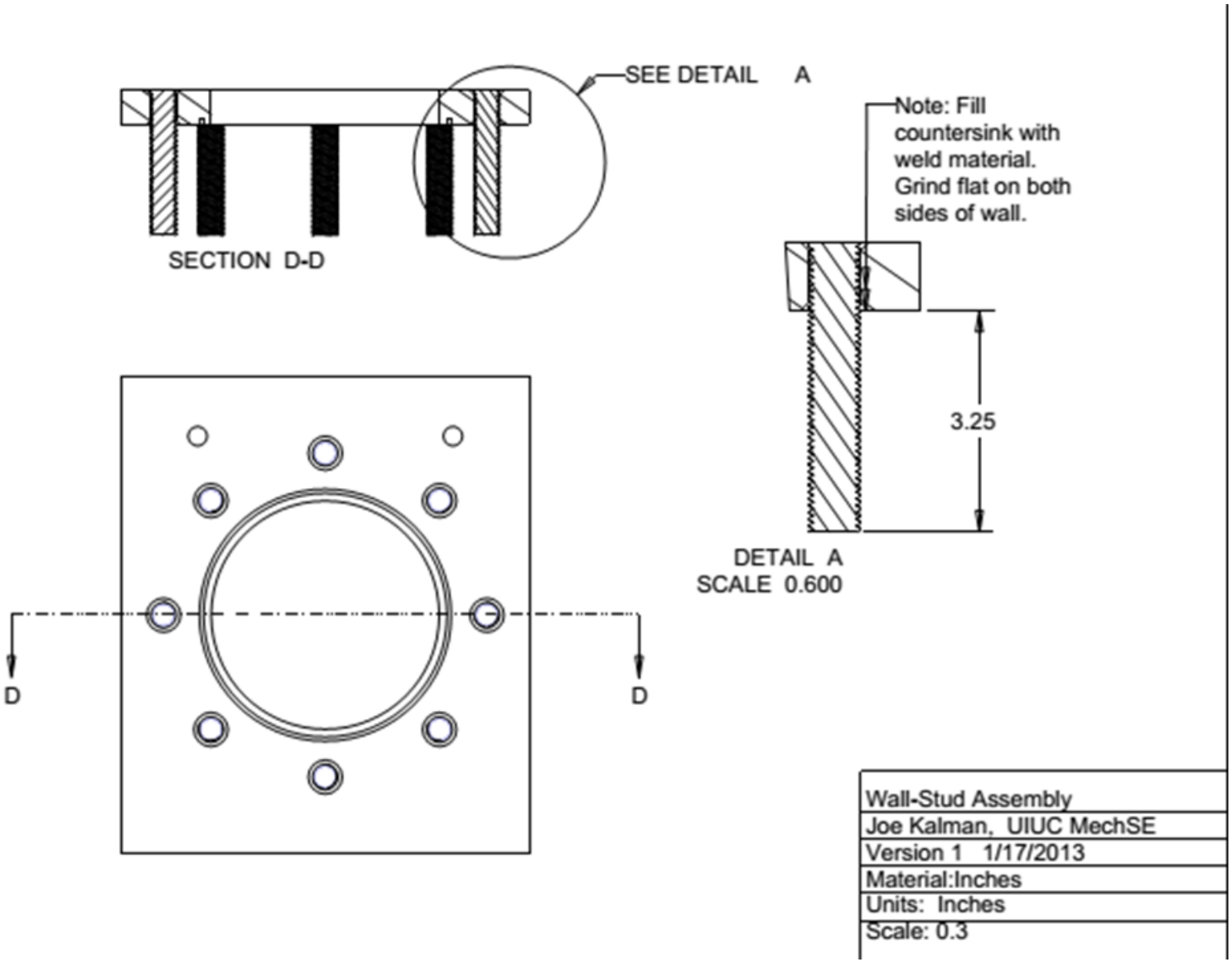
SEE DETAIL A
SECTION D-D
Note: Fill countersink with weld material. Grind flat on both sides of wall.
3.25
DETAIL A
SCALE 0.600
D
D
Wall-Stud Assembly
Joe Kalman, UIUC MechSE
Version 1 1/17/2013
Material:Inches
Units: Inches
Scale: 0.3

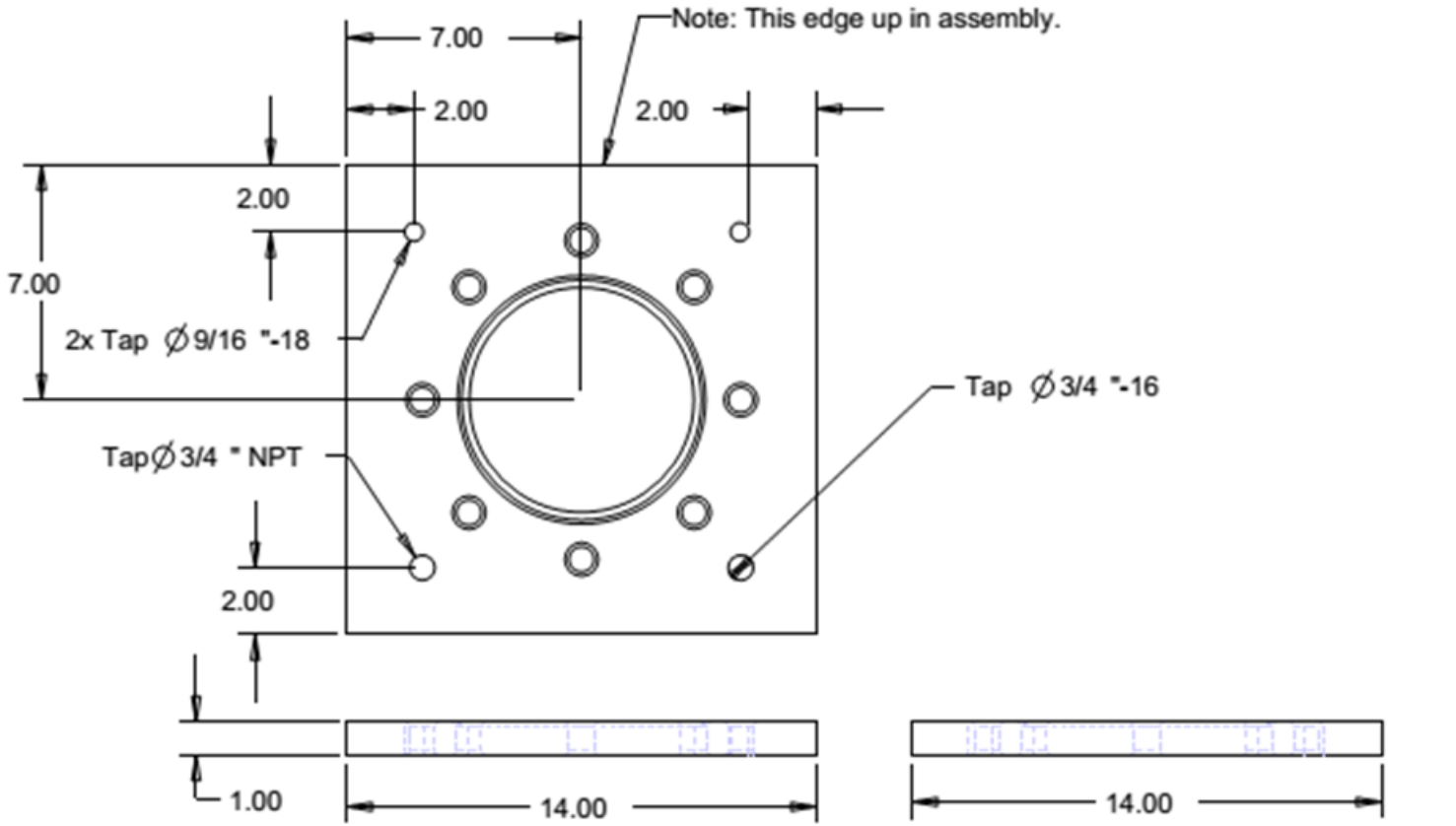

Blast Chamber Back Quantity: 1
Joe Kalman, UIUC MechSE
Version 1 1/16/2013
Material: Steel
Units: Inches
Scale: 0.25

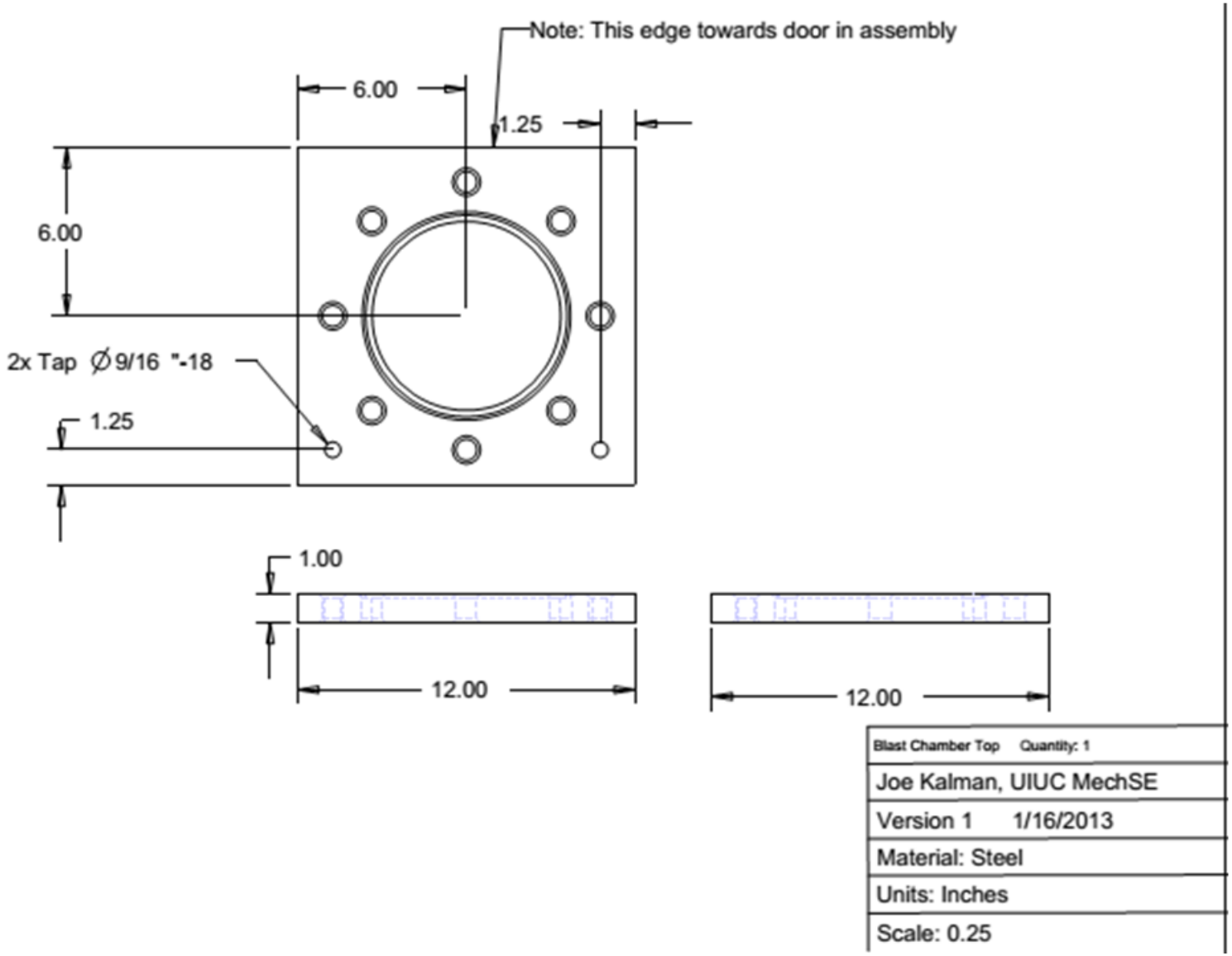
Note: This edge towards door in assembly
6.00
1.25
6.00
2x Tap ∅9/16 "-18
1.25
1.00
12.00
12.00
Blast Chamber Top Quantity: 1
Joe Kalman, UIUC MechSE
Version 1 1/16/2013
Material: Steel
Units: Inches
Scale: 0.25

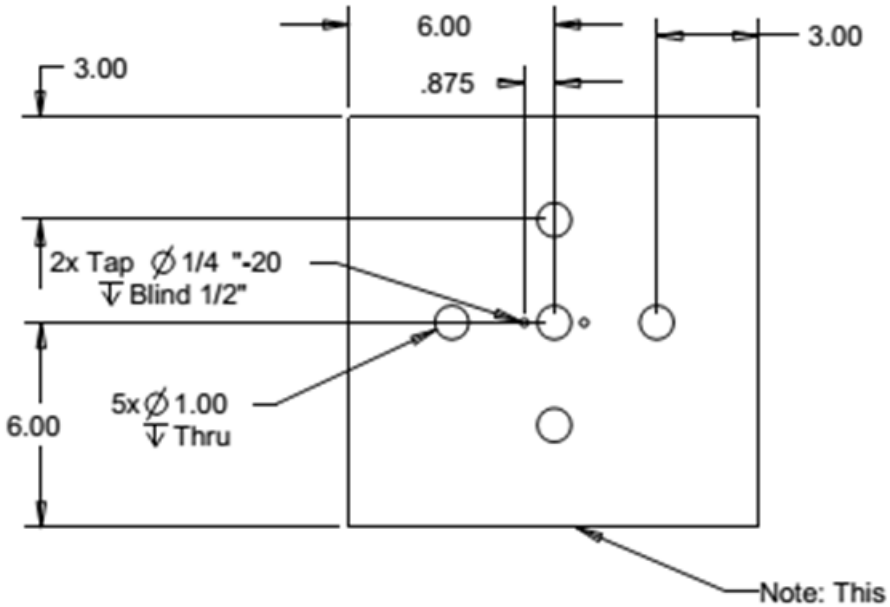

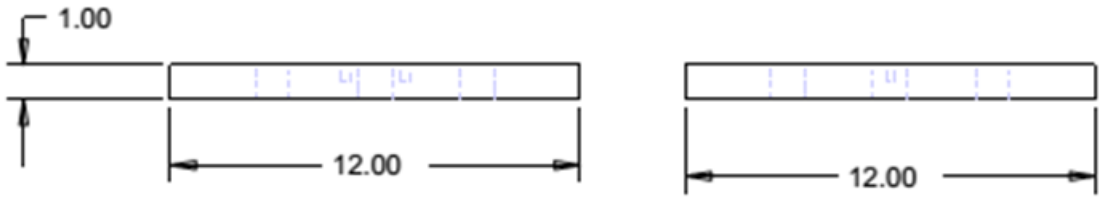

Blast Chamber Bottom Quantity: 1
Joe Kalman, UIUC MechSE
Version 1 1/16/2013
Material: Steel
Units: Inches
Scale: 0.25

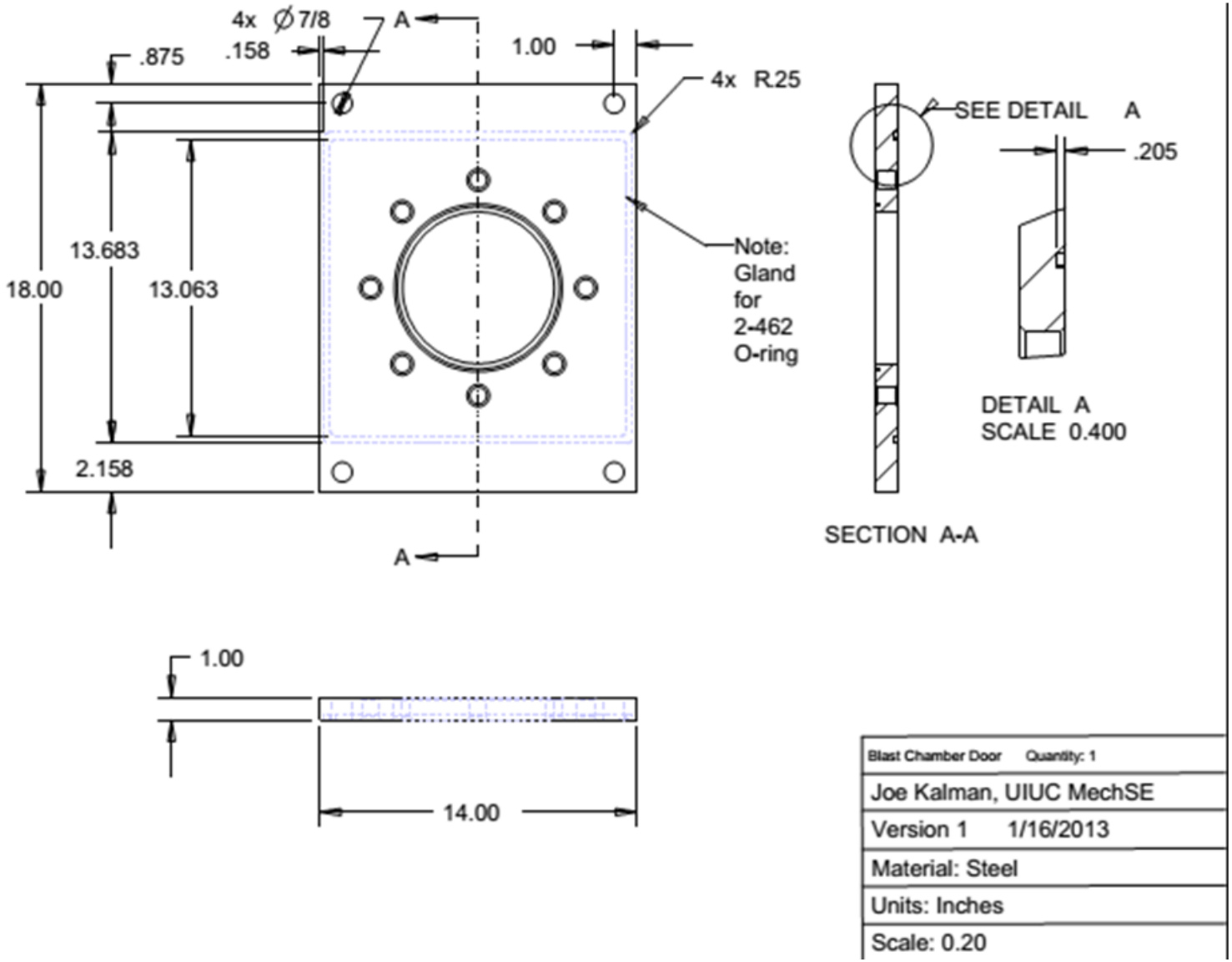
4x ∅7/8
.158
A
.875
1.00
4x R.25
13.683
18.00
13.063
Note:
Gland
for
2-462
O-ring
2.158
A
SEE DETAIL A
.205
DETAIL A
SCALE 0.400
SECTION A-A
1.00
14.00
Blast Chamber Door Quantity: 1
Joe Kalman, UIUC MechSE
Version 1 1/16/2013
Material: Steel
Units: Inches
Scale: 0.20

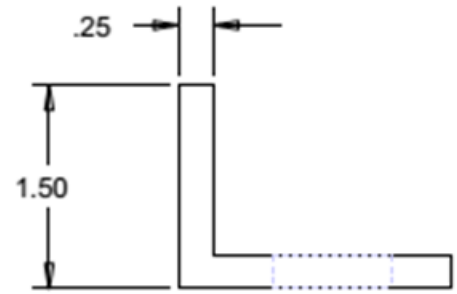

Note: Make from McMaster part 9017K77 or equivalent

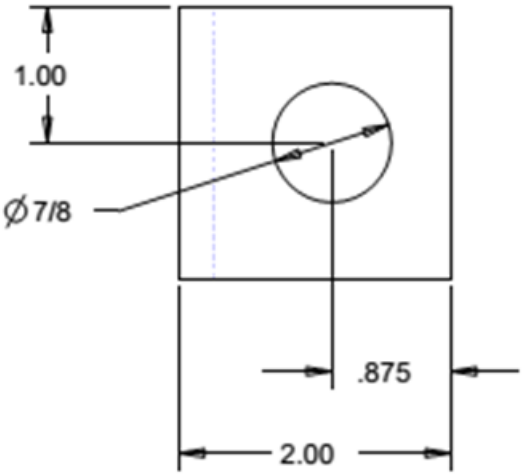

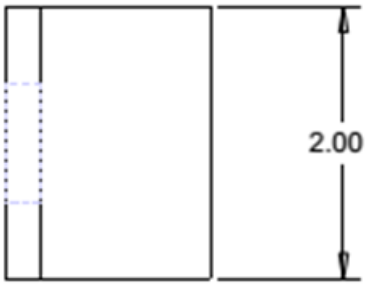

Door Clamp Bracket Quantity:4
Joe Kalman, UIUC MechSE
Version 1 1/16/2013
Material: Steel
Units: Inches
Scale: 1.0

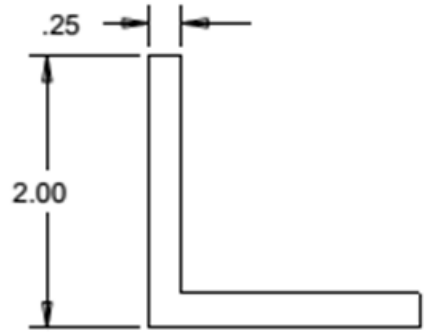

Note:Make from McMaster Part K9017K81 or equivalent

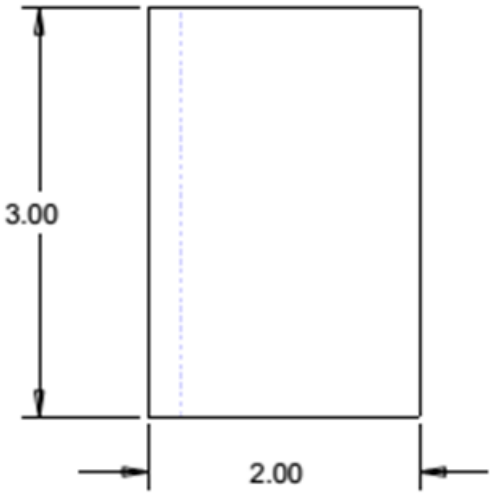

Hinge Mount Bracket Quantity: 2
Joe Kalman, UIUC MechSE
Version 1 1/16/2013
Material: Steel
Units: Inches
Scale: 1.0

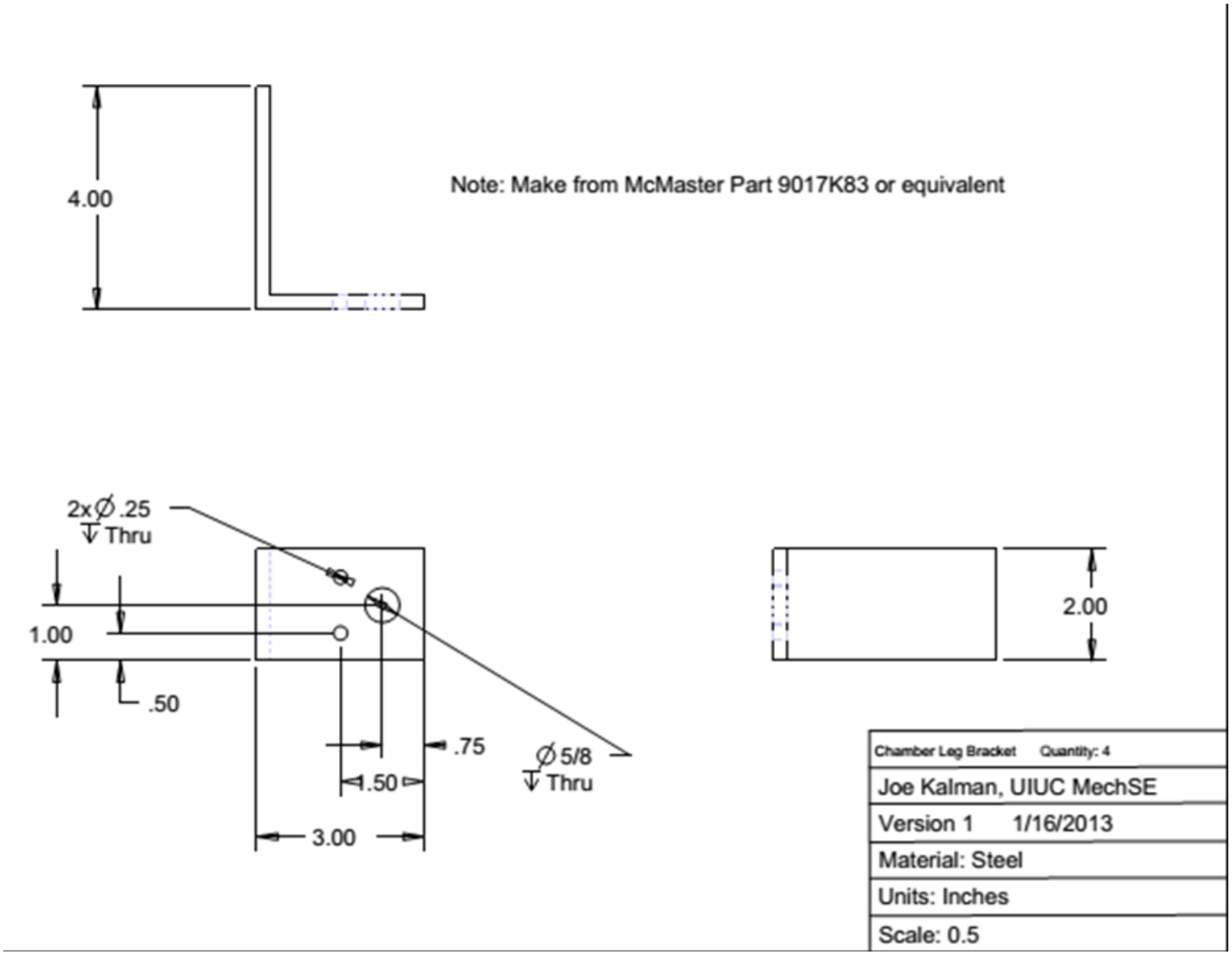
4.00
Note: Make from McMaster Part 9017K83 or equivalent
2x Ø .25
Thru
1.00
.50
.75
1.50
3.00
Ø 5/8
Thru
2.00
Chamber Leg Bracket Quantity: 4
Joe Kalman, UIUC MechSE
Version 1 1/16/2013
Material: Steel
Units: Inches
Scale: 0.5

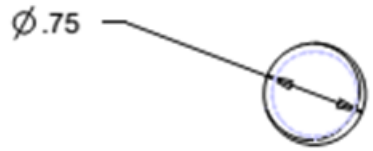

Note: Make from Grade 8, 3/4"-10 Threaded Rod

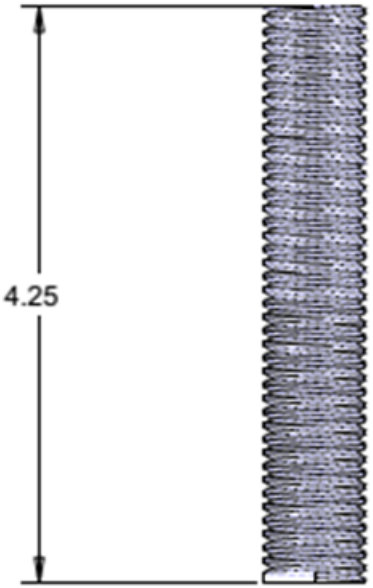

Note: Length includes the 1" portion inserted into chamber walls. Stud should protrude 3.25" out from chamber walls.

Threaded Studs Quantity: 40
Joe Kalman, UIUC MechSE
Version 1 1/16/2013
Material: Grade 8 Steel
Units: Inches
Scale: 1.0

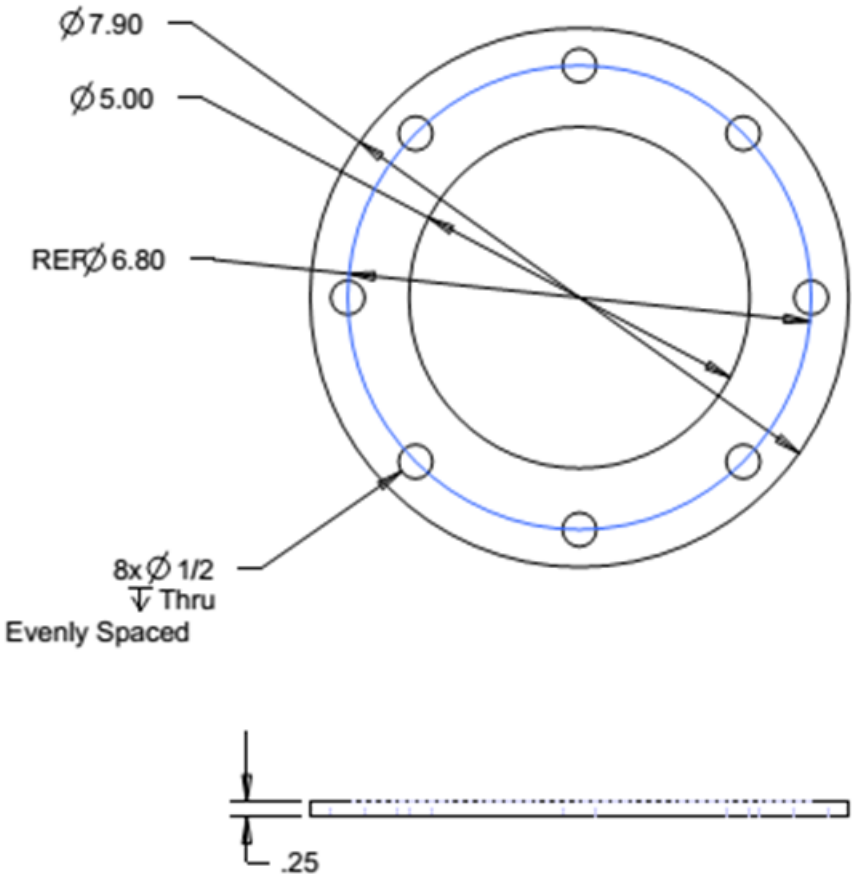

Window Adapter Clamp Quantity: 2
Joe Kalman, UIUC MechSE
Version 1 1/17/2013
Material: Steel
Units: Inches
Scale: 0.5

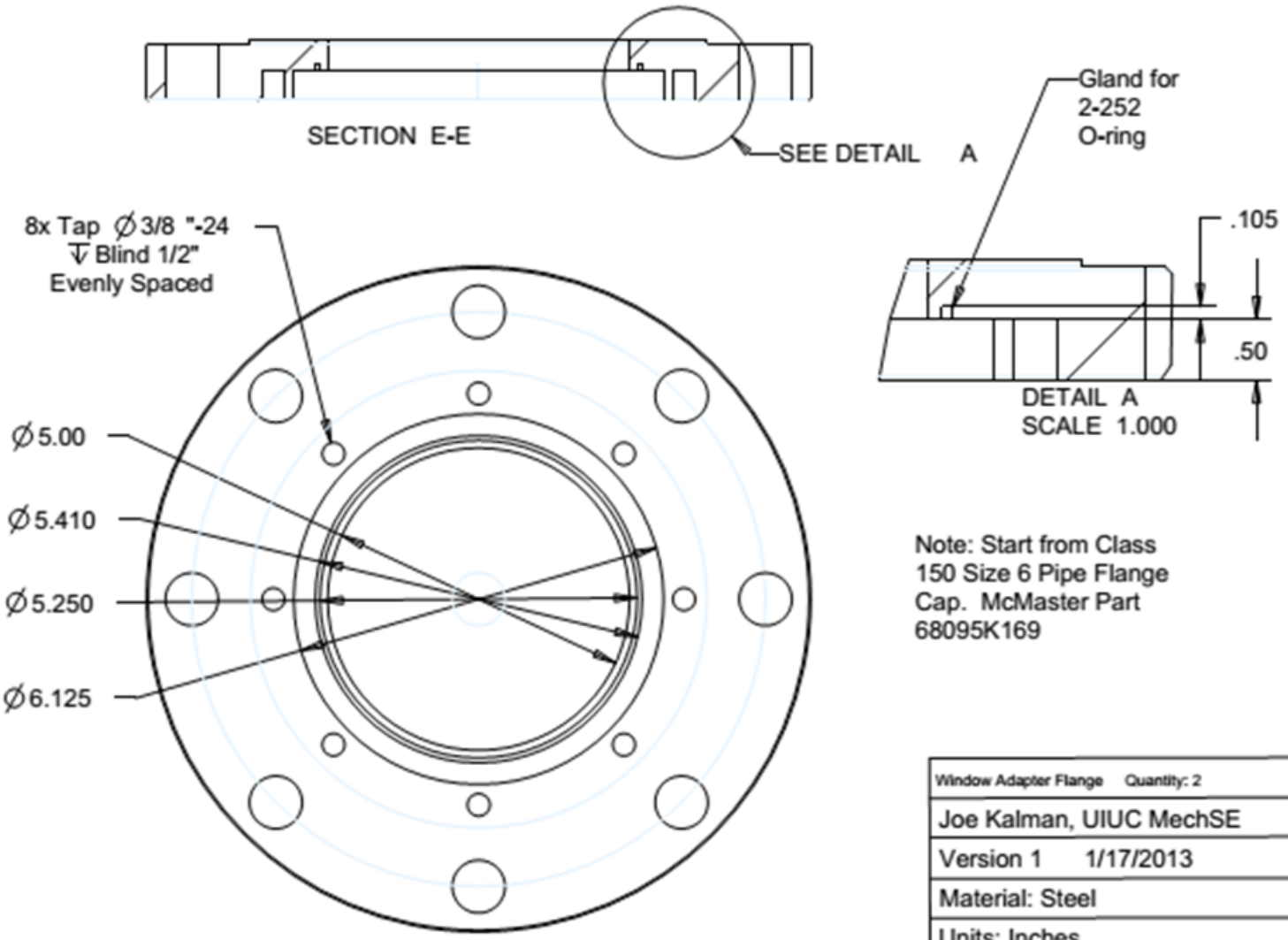

Note: Start from Class 150 Size 6 Pipe Flange Cap. McMaster Part 68095K169

Window Adapter Flange Quantity: 2
Joe Kalman, UIUC MechSE
Version 1 1/17/2013
Material: Steel
Units: Inches
Scale: 0.5

APPENDIX C

FRANCK-CONDON FACTOR CALCULATION

The probability of an electronic transition of a molecule is proportional to the strength (or probability) of the associated electronic, vibrational, and rotational transitions. The Franck-Condon factor describes the probability of a vibrational transition occuring. Recall that the Franck-Condon principle states that the electronic motion is much faster than the nuclear motion. Because of this principle, the molecule radius is essential constant during an electronic transition. The radius of molecule is dependent on the vibrational state. The probability of the vibrational transition can then be inferred to be related to the overlap of the vibrational wavefunction. This principle is illustrated by Figure C.1. The red arrow indicates the transition from the upper to lower state (i.e. emission) while the orange curves represent the wavefunctions. The Franck-Condon factor, $S_{v'v''}$, is given by the following relationship:

$$S_{v'v''} = \left| R_{vib}^{v'v''} \right|^2 = \left| \int \psi_v^{'} \psi_v^{''} dv_n \right|^2 \tag{C.1}$$

where $R_{vib}^{v'v''}$ is the so-called overlap intergral, ψ is the vibrational wavefunction with the single and double primes representing the initial and final vibrational state, dv_n is a differential volume element [41].

For the purpose of simulating the spectrum for a diatomic molecule, the vibrational wavefunction is assumed to be one dimensional so that the volume element, dv_n, becomes a differential radial segment, dr. The molecular vibration can be modelled as a harmonic oscillator. The solution to Schrodinger's equation for the $v = 0$ and $v = 1$ energy levels assuming a harmonic oscillator is given as follows:

$$\psi_0 = (\frac{\alpha}{\pi})^{0.25} e^{-0.5\alpha x^2} \tag{C.2}$$

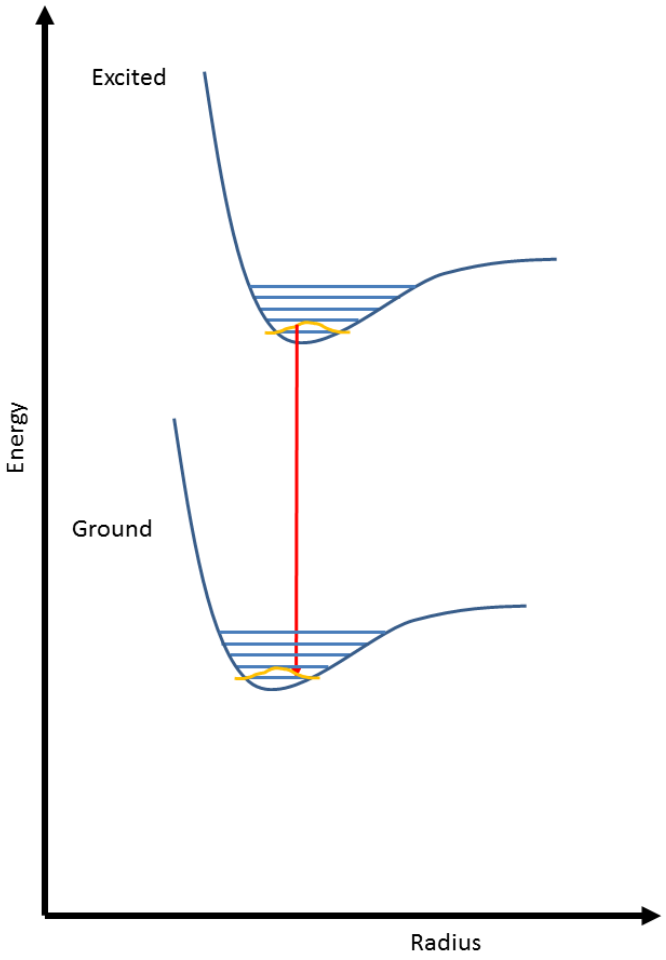

Figure C.1: Illustration of the energy diagram for an electronic transition of a molecule. The orange curves indicate the vibration wavefunctions. Energy levels are not drawn to scale.

$$\psi_1 = (\frac{\alpha}{\pi})^{0.25}(2\alpha^{0.5}x)e^{-0.5\alpha x^2} \tag{C.3}$$

where $\alpha = \frac{2\pi\mu\nu}{\hbar}$, $x = r - r_e$, and μ is the reduced mass. Equations C.2 and C.3 are used for both the upper and lower states (i.e. single and double prime). The Franck-Condon factor is calculated by substituting the expressions for $\psi_0^{'}$ and $\psi_0^{''}$ into Equation C.1. Note that the appropriate spectroscopic constants (e.g. r_e) are evaluated for either the upper or lower state. Equation C.1 is integrated from $r = 0$ to $r = \infty$ to determine the Franck-Condon factor for the (0,0) transition. This calculation is represented by the fraction of the area under the orange curve in excited state in Figure C.1 that is above the the orange curve in the ground state drawn in Figure C.1. A similar process is used for the other vibrational transitions with the appropriate wavefunction. As mentioned in Section 3.3.4, the square root of these factors (i.e. the evaluation of the overlap integral directly) is needed as an input into PGOPHER [43].

REFERENCES

[1] S. A. Grinshpun, A. Adhikari, M. Yermakov, T. Reponen, E. Dreizin, M. Schoenitz, V. Hoffmann, and S. Zhang, "Inactivation of aerosolized bacillus atrophaeus (bg) endospores and ms2 viruses by combustion of reactive materials," *Environmental Science & Technology*, vol. 46, no. 13, pp. 7334–7341, 2012.

[2] B. R. Clark and M. L. Pantoya, "The aluminium and iodine pentoxide reaction for the destruction of spore forming bacteria," *Physical Chemistry Chemical Physics*, vol. 12, no. 39, pp. 12653–12657, 2010.

[3] S. Zhang, M. Schoenitz, and E. L. Dreizin, "Iodine Release, Oxidation, and Ignition of Mechanically Alloyed AlComposites," *The Journal of Physical Chemistry C*, vol. 114, no. 46, pp. 19653–19659, 2010.

[4] D. Allen, "Optical combustion measurements of novel energetic materials in a heterogeneous shock tube," Master's thesis, University of Illinois at Urbana-Champaign, Mechanical Science and Engineering, 2012.

[5] M. Clemenson, "Explosive initiation of various forms of the ti/2b energetic system," Master's thesis, University of Illinois at Urbana-Champaign, Mechanical Science and Engineering, 2012.

[6] E. Shafirovich, S. K. Teoh, and A. Varma, "Combustion of levitated titanium particles in air," *Combustion and Flame*, vol. 152, no. 1, pp. 262–271, 2008.

[7] J. O. Nriagu, ed., *Sulfur in the Environment, Part I:The Atmospheric Cycle*. John Wiley and Sons, 1978.

[8] B. Setlow, C. Loshon, P. Genest, A. Cowan, C. Setlow, and P. Setlow, "Mechanisms of killing spores of bacillus subtilis by acid, alkali and ethanol," *Journal of Applied Microbiology*, vol. 92, no. 2, pp. 362–375, 2002.

[9] I. Glassman and R. Yetter, *Combustion*. Academic Press, Academic Press, 2008.

[10] C. Law, *Combustion Physics*. Cambridge University Press.

[11] Turns, *An Introduction to Combustion: Concepts and Applications*. McGraw-Hill series in mechanical engineering, McGraw-Hill Education, 2000.

[12] N. M. Laurendeau, *Statistical Thermodynamics: Fundamentals and Applications*. Cambridge University Press, 2010.

[13] T. Bazyn, H. Krier, and N. Glumac, "Evidence for the transition from the diffusion-limit in aluminum particle combustion," *Proceedings of the Combustion Institute*, vol. 31, no. 2, pp. 2021 – 2028, 2007.

[14] P. Lynch, H. Krier, and N. Glumac, "A correlation for burn time of aluminum particles in the transition regime," *Proceedings of the Combustion Institute*, vol. 32, no. 2, pp. 1887 – 1893, 2009.

[15] M. Beckstead, "Correlating aluminum burning times," *Combustion, Explosion and Shock Waves*, vol. 41, no. 5, pp. 533–546, 2005.

[16] S. Goroshin, F.-D. Tang, A. J. Higgins, and J. H. Lee, "Laminar dust flames in a reduced-gravity environment," *Acta Astronautica*, vol. 68, no. 78, pp. 656 – 666, 2011.

[17] S. Goroshin, J. Mamen, A. Higgins, T. Bazyn, N. Glumac, and H. Krier, "Emission spectroscopy of flame fronts in aluminum suspensions," *Proceedings of the Combustion Institute*, vol. 31, no. 2, pp. 2011 – 2019, 2007.

[18] L. Landau and E. Lifshitz, *Fluid Mechanics*. Permagon Press, 1959.

[19] R. K. Eckhoff, *Dust Explosions in the Process Industries*. Burlington: Gulf Professional Publishing, third edition ed., 2003.

[20] I. Hartmann, "The explosibility of titanium, zirconium, thorium, uranium, and their hydrides.(bureau of mines report no. 3202)," tech. rep., Bureau of Mines, 1951.

[21] M. T. P. R. Santhanam, V.K. Hoffman and E. Dreizin, "Characteristics of aluminum combustion," *Combustion Science and Technology*, vol. 182, pp. 904–921, 2010.

[22] S. Goroshin, M. Bidabadi, and J. Lee, "Quenching distance of laminar flame in aluminum dust clouds," *Combustion and Flame*, vol. 105, pp. 147–160, 1996.

[23] J. Jarosinski, J. Lee, R. Knystautas, and J. Crowley, "Quenching of dust-air flames," in *Symposium (International) on Combustion*, vol. 21, pp. 1917–1924, 1988.

[24] R. S. Conti, K. L. Cashdollar, and I. Liebman, "Improved optical probe for monitoring dust explosions," *Review of Scientific Instruments*, vol. 53, no. 3, pp. 311–313, 1982.

[25] I. Liebman, R. S. Conti, and K. L. Cashdollar, "Dust cloud concentration probe," *Review of Scientific Instruments*, vol. 48, no. 10, pp. 1314–1316, 1977.

[26] O. Kalejaiye, P. R. Amyotte, M. J. Pegg, and K. L. Cashdollar, "Effectiveness of dust dispersion in the 20-l siwek chamber," *Journal of Loss Prevention in the Process Industries*, vol. 23, no. 1, pp. 46 – 59, 2010.

[27] C. Kauffman, S. Srinath, F. Tezok, J. Nicholls, and M. Sichel, "Turbulent and accelerating dust flames," *Symposium (International) on Combustion*, vol. 20, no. 1, pp. 1701 – 1708, 1985. Twentieth Symposium (International) on Combustion.

[28] G. Zhen and W. Leuckel, "Effects of ignitors and turbulence on dust explosions," *Journal of Loss Prevention in the Process Industries*, vol. 10, pp. 317–324, 1997.

[29] A. Di Benedetto, A. Garcia-Agreda, P. Russo, and R. Sanchirico, "Combined effect of ignition energy and initial turbulence on the explosion behavior of lean gas/dust-air mixtures," *Industrial & Engineering Chemistry Research*, vol. 51, no. 22, pp. 7663–7670, 2012.

[30] N. Kuai, W. Huang, B. Du, J. Yuan, Z. Li, Y. Gan, and J. Tan, "Experiment-based investigations on the effect of ignition energy on dust explosion behaviors," *Journal of Loss Prevention in the Process Industries*, vol. 26, no. 4, pp. 869 – 877, 2013.

[31] C. Cloney, R. Ripley, P. Amyotte, and F. Khan, "Quantifying the effect of strong ignition sources on particle preconditioning and distribution in the 20-l chamber," in *Proc. of the 9th Int. Symp. Hazards, Prev., and Mitigation Ind. Explosions*, 2012.

[32] S. Gordon and B. J. McBride, "Computer program for calculation of complex chemical equilibrium compositions and applications," tech. rep., NASA Reference Publication 1311, 1996.

[33] W. N. Tuller, ed., *The Sulphur Data Book*. McGraw-Hill, 1954.

[34] C. Proust, "A few fundamental aspects about ignition and flame propagation in dust clouds," *Journal of Loss Prevention in the Process Industries*, vol. 19, pp. 104 – 120, 2006.

[35] T. Ziehn and A. Tomlin, "A Global Sensitivity Study of Sulfur Chemistry in a Premixed Methane Flame Model Using HDMR," *International Journal of Chemical Kinetics*, vol. 40, pp. 742–753.

[36] E. Randeberg and R. K. Eckhoff, "Measurement of minimum ignition energies of dust clouds in the less than 0.01mj region," *Journal of Hazardous Materials*, vol. 140, no. 12, pp. 237 – 244, 2007.

[37] J. Nagy, *Development and Control of Dust Explosions*. CRC, 1983.

[38] C. Proust, "Flame propagation and combustion in some dust-air mixtures," *Journal of Loss Prevention in the Process Industries*, vol. 19, no. 1, pp. 89 – 100, 2006.

[39] R. Fristrom, *Flame Structure and Processes*. Oxford University Press, 1995.

[40] T. A. Bazyn, *Spectroscopic Measurements of the Combustion of Aluminum and Aluminum-based Energetic Material Particles Using a Heterogeneous Shock Tube*. PhD thesis, University of Illinois at Urbana-Champaign, Mechanical Engineering, 2006.

[41] A. C. Eckbreth, *Laser Diagnostics for Combustion Temperature and Species*. Gordon and Breash Publishers, 1996.

[42] G. Herzberg, *Molecular Spectra and Molecular Structureructure: I. Spectra of Diatomic Molecules*. D. Van Nostrand Company, 1964.

[43] C. M. Western, "PGOPHER, a Program for Simulating Rotational Structure."

[44] S. Goroshin, D. Frost, J. Levine, A. Yoshinaka, and F. Zhang, "Optical pyrometry of fireballs of metalized explosives," *Propellants, Explosives, Pyrotechnics*, vol. 31, no. 3, pp. 169–181, 2006.

[45] T. Panagiotou, Y. Levendis, and M. Delichatsios, "Measurements of particle flame temperatures using three-color opticalpyrometry," *Combustion and Flame*, vol. 104, no. 3, pp. 272 – 287, 1996.

[46] P. Lynch, H. Krier, and N. Glumac, "Emissivity of aluminum-oxide particle clouds: Application to pyrometry of explosive fireballs," *Journal of Thermophysics and Heat Transfer*, vol. 24, no. 2, pp. 301–308, 2010.

[47] J. Kalman, D. Allen, N. Glumac, and H. Krier, "Optical depth effects on aluminum oxide emissivity," *AIAA Journal of Thermophysics and Heat Transfer*, Submitted August 2013. Submitted.

[48] J. Kalman, N. Glumac, and H. Krier, "High temperature metal oxide spectral emissivities for pyrometry applications," *AIAA Journal of Thermophysics and Heat Transfer*. Submitted.

[49] H. Cassel, I. Liebman, and W. Mock, "Radiative transfer in dust flames," in *Symposium (International) on Combustion*, pp. 602–605, 1957.

[50] H. Cassel, A. Das Gupta, and S. Guruswamy, "Factors affecting flame propagation through dust clouds," in *Third Symposium on Combustion and Flame, and Explosion Phenomena*, pp. 185–190, 1949.

[51] S. Goroshin, I. Fomenko, and J. Lee, "Burning velocities in fuel-rich aluminum dust clouds," in *Symposium (International) on Combustion*, vol. 26, pp. 1961–1967, 1996.

[52] J. Knapton, I. Stobie, and H. Krier, "Burning rate studies of fuel air mixtures at high pressures," *Combustion and Flame*, vol. 21, no. 2, pp. 211 – 220, 1973.

[53] A. Dahoe and L. de Goey, "On the determination of the laminar burning velocity from closed," *Journal of Loss Prevention in the Process Industries*, vol. 457-478, p. 16, 2003.

[54] C. Luijten, E.Doosje, and L. de Goey, "Accurate analytical models for fractional pressure rise in constant volume," *International Journal of Thermal Sciences*, vol. 48, pp. 1213–1222, 2009.

[55] M. Nair and M. Gupta, "Burning velocity measurement by bomb method," *Combustion and Flame*, vol. 22, pp. 219–221, 1974.

[56] J. Manton, G. V. Elbe, and B. Lewis, "Burning-Velocity Measurements in a Spherical Vessel With Central Ignition," *Symposium (International) on Combustion*.

[57] P. van der Wel, J. van Veen, S. Lemkowitz, B. Scarlett, and C. van Wingerden, "An interpretation of dust explosion phenomena on the basis of time scales," *Powder Technology*, vol. 71, no. 2, pp. 207 – 215, 1992.

[58] OSHA, "Sulfur dioxide."

[59] C. Bohren and D. Huffman, *Absorption and Scattering of Light by Small Particles*. Wiley Science Series, John Wiley and Sons, 2008.

[60] Y. A. Cengel, *Heat and Mass Transfer: A Practical Approach*. McGraw-Hill, 2006.

[61] D. R. Lide, ed., *Handbook of Chemistry and Physics*. CRC Press, 1992-1993.

[62] N. Glumac, H. Krier, T. Bazyn, and R. Eyer, "Temperature measurements of aluminum particles burning in carbon dioxide," *Combustion Science and Technology*, vol. 177, no. 3, pp. 485–511, 2005.

[63] A. Klippel, M. Scheid, and U. Krause, "Investigations into the influence of dustiness on dust explosions," *Journal of Loss Prevention in the Process Industries*, vol. 26, pp. 1616–1626, 2013.

[64] G. Gold, R. N. Duvall, B. T. Palermo, and J. G. Slater, "Powder flow studies iii. factors affecting the flow of lactose granules," *Journal of Pharmaceutical Sciences*, vol. 57, no. 4, pp. 667–671, 1968.

[65] P. Elder, T. Jerrick, and J. W. Birkeland, "Determination of the radial profile of absorption and emission coefficients and temperature in cylindrically symmetric sources with self-absorption," *Appl. Opt.*, vol. 4, pp. 589–592, May 1965.

[66] S. J. Young, "Iterative abel inversion of optically thick, cylindrically symmetric radiation sources," *Journal of Quantitative Spectroscopy and Radiative Transfer*, vol. 25, no. 5, pp. 479 – 481, 1981.

[67] M. Frenklach, H. Wang, C.-L. Yu, M. Goldenberg, C. Bowman, R. Hanson, D. Davidson, E. Chang, G. Smith, D. Golden, W. Gardiner, and V. Lissianski, "Gri-mech—an optimized detailed chemical reaction mechanism for methane combustion," tech. rep., 1995.

[68] G. Andrews and D.Bradley, "The burning velocity of methane-air flames," *Combustion and Flame*, vol. 19, pp. 275–288, 1972.

[69] D. Goodwin, "Cantera: An object-oriented software toolkit for chemical kinetics, thermodynamics, and transport processes," 2009.

[70] K. L. Cashdollar, "Flammability of metals and other elemental dust clouds," *Process Safety Progress*, vol. 13, no. 3, pp. 139–145, 1994.

[71] J. M. Ajello, D. L. Hansen, L. W. Beegle, C. A. Terrell, I. Kanik, G. K. James, and O. P. Makarov, "Middle ultraviolet and visible spectrum of so2 by electron impact," *Journal of Geophysical Research: Space Physics*, vol. 107, pp. SIA 2–1–SIA 2–7, 2002.

[72] W. R. Anderson, D. R. Crosley, and J. E. Allen Jr, "Franck–Condon Factors for the B–X System of S_2," *The Journal of Chemical Physics*, vol. 71, pp. 821–829, 2008.

[73] A. L. Smith and J. B. Hopkins, "Fluorescence of S_2 (B–X) Excited by Fixed Frequency Ultraviolet Lasers," *The Journal of Chemical Physics*, vol. 75, pp. 2080–2084, 1981.

[74] G. Lakshminarayana and C. Mahajan, "Spectroscopic studies of the sulphur afterglow," *Journal of Quantitative Spectroscopy and Radiative Transfer*, vol. 16, no. 7, pp. 549 – 552, 1976.

[75] R. Schlapp, "Intensities in singlet-triplet bands of diatomic molecules," *Phys. Rev.*, vol. 39, pp. 806–815, Mar 1932.

[76] G. Herzberg and T. J. Hugo, "Forbidden transitions in diatomic molecules: Iv. the absorption bands of carbon monoxide," *Canadian Journal of Physics*, vol. 33, no. 12, pp. 757–772, 1955.

[77] R. Colin, "The $b^1\Sigma^+ - X^3\Sigma^-$ Band System of SO," *Canadian Journal of Physics*, vol. 46, p. 1539, 1968.

[78] M. Greenberg, *Advanced Engineeing Mathematics*. Pearson.

[79] I. Barnes, K. Becker, and E. Fink, "Near-infrared Emissions From the $^1\Delta_g$ and $^1\Sigma_g^+$ States of S_2," *Chemical Physics Letters*, vol. 67, no. 23, pp. 314 – 317, 1979.

[80] P. H. Krupenie, "The spectrum of molecular oxygen," *Journal of Physical Chemistry*, vol. 1, 1972.

[81] L. Monchick and E. A. Mason, "Transport properties of polar gases," *The Journal of Chemical Physics*, vol. 35, no. 5, pp. 1676–1697, 1961.